POROUS BOUNDARY EFFECTS IN TURBULENT SHEAR FLOW

by
J. F. Ruff
and
L. W. Gelhar

(WATER RESOURCES AND)
M.I.T. HYDRODYNAMICS LABORATORY

Report No. 126

Prepared Under
National Science Foundation
Engineering Division
Grant No. GK-4180

July 1970

MIT

DEPARTMENT
OF
CIVIL
ENGINEERING

SCHOOL OF ENGINEERING
MASSACHUSETTS INSTITUTE OF TECHNOLOGY
Cambridge, Massachusetts 02139

R 70-40 DSR 71423

WATER RESOURCES AND HYDRODYNAMICS LABORATORY

Department of Civil Engineering

Massachusetts Institute of Technology

POROUS BOUNDARY EFFECTS IN TURBULENT SHEAR FLOW

by

James F. Ruff

Lynn W. Gelhar

July, 1970

Report No. 126

Prepared Under

National Science Foundation

Engineering Division

Grant No. GK-4180

ABSTRACT

POROUS BOUNDARY EFFECTS IN TURBULENT SHEAR FLOW

A technique of measuring seepage velocities is developed in order to investigate the velocity distribution in a porous boundary exposed to a turbulent shear flow. Measurements are performed in a 1.2 in. thick polyurethane foam lining of 12 in. inside diameter pipe using hot wire anemometer and a helium tracer technique involving the determination of the travel time of the peak concentration. In the shear zone, seepage velocities are determined directly from shielded hot wire anemometer data. In the pressure gradient flow zone, the helium tracer technique is used to measure the seepage velocities. Results of the velocity measurements indicate that the shear effect penetrates a relatively small distance into the porous boundary (approximately 0.25 to 0.30 in.). Measurements of the permeability and longitudinal dispersion coefficient are also made.

Three analytical models based upon the eddy viscosity concept are developed in an effort to gain some insight into the mechanism relating the turbulent shear flow and the porous boundary flow through the velocity distribution in the boundary. The models are extended to relate the core and boundary flow regions and an attempt is made to predict the friction factor for the pipe. The models provide a reasonable agreement with the observed velocity profile but indicate a decreasing friction factor with increasing Reynolds number whereas the observed friction factor increases.

Development of the helium tracer technique for velocity measurements requires additional information concerning the concentration distribution of a tracer in a shear flow. Perturbation methods are used to develop analytical solutions of the convective dispersion equation with an instantaneous point source in a shear flow for both constant and variable dispersion coefficients and the limitations of the solutions are defined. The analysis indicated shear effects caused no distortion on the longitudinal axis and the distortion due to dispersion was insignificant for the dimensions used in the experiments.

ACKNOWLEDGEMENT

The present investigation was carried out in the Hydrodynamics Laboratory of the Department of Civil Engineering at the Massachusetts Institute of Technology. The investigation was sponsored by the National Science Foundation under Grant No. GK-4180 administered at M.I.T. under DSR 71423. Part of the computational work was done at the Information Processing Center at M.I.T.

The assistance of Messrs. Y. H. Chu and P. Liu, Research Assistants in the Hydrodynamics Laboratory, in collecting and processing much of the data is appreciated. Mr. Edward McCaffrey provided technical advice for the electronic equipment.

The report is essentially a reproduction of the dissertation submitted by the senior author in September, 1970, in partial fulfillment of the requirements for the degree of Doctor of Philosophy. Dr. Lynn W. Gelhar, Associate Professor of Civil Engineering, served as thesis advisor. Mr. Ruff was supported in his doctoral studies through an N.D.E.A. Title IV Fellowship.

TABLE OF CONTENTS

I. INTRODUCTION

Flow in alluvial channels involves a complex interaction between the turbulent fluid motion of the stream, the particulate material being transported and possibly the flow in the porous bed. The fluid turbulence is the main feature of the interaction and it contributes to the entrainment and motion of the particles along the bed of the channel. The flow in the porous bed can cause uplift forces which may influence the sediment motion. Furthermore, the turbulence structure of the external flow can be modified by the flow in the porous boundary.

There are two specific mechanisms which can be involved in the porous boundary that are not possible with solid boundaries. A finite slip velocity can exist at the surface of the porous boundary. Also, it is possible to have lateral turbulent motion at the boundary which may increase the momentum transfer between the shear flow and the boundary. These mechanisms have opposite effects on the friction factor. The slip velocity tends to decrease the friction and the increased momentum transfer causes an increase.

Little information is available concerning these mechanisms for flow in a porous medium exposed to a turbulent shear flow, the primary reason being that direct measurements of velocities in a porous medium are difficult to achieve. Instruments and techniques necessary to provide satisfactory results have not been perfected. Without adequate measurements in the porous medium, the assumptions regarding the interaction of the mechanisms can be checked only through measurements of gross flow features such as the head loss.

In order to provide some basic information about the porous medium flow, the present investigation is oriented towards a determination of the velocity distribution in the porous medium. The study is concerned primarily with the flow in a porous boundary when the boundary is exposed to an external turbulent shear flow. Through the determination of the velocity distribution it is hoped that a better understanding of the interacting mechanisms can be achieved. The primary focus of the investigation is the development of a method of measuring seepage velocities in the porous boundary. It was felt that the measurements of porous boundary effects in mobile sand beds would be extremely complicated and that the actual effects of boundary permeability would be difficult to isolate. Therefore, a rigid porous medium was selected for this initial work. The problem is approached as one of fundamental fluid mechanics and although it may have relevance to sediment transport, no further attempt will be made to develop that aspect.

The contents of this report are outlined as follows. In Chapter 2 experimental technqiues for observing velocity distributions in the porous boundary are described. Supplemental to the velocity measurements are in situ determination of intrinsic permeability and longitudinal dispersion coefficients for the porous foam boundary.

In Chapter 3 mathematical models based on different eddy viscosity assumptions are developed in an effort to describe the mean velocity distribution in the porous boundary of the pipe. The predicted velocity distributions are compared with those observed. An analysis is developed linking the pipe core and the boundary flow fields together through

the surface velocity and the eddy viscosity at the boundary surfaces. The model provides a prediction of the porous pipe friction factor thus permitting a comparison of predicted and observed friction factors.

Development of the helium tracer technique of making velocity measurements required additional information concerning the concentration distribution of a tracer in shear flow. Therefore, a perturbation solution for dispersion of a tracer from an instantaneous point source in a shear flow is developed. The limitations of the solutions are identified and application to the experiments is considered. Before proceeding with the experimental investigation some information concerning similar flow situations and investigations is presented.

An unusual problem involving porous boundary effects is the determination of sediment deposition in gravel beds used by spawning salmon. Einstein (1968) has investigated this problem and presented experimental results of deposition of silt-sized particles in a gravel bed of a recirculating laboratory flume.

Meteorologists have long been concerned with the flow patterns within crop or forest canopies. These so-called canopy flows closely resemble the flow situation expected in the porous pipe boundary. Inoue (1963), applying a mixing length concept developed a description of the wind velocity profile within the canopy of exponential form. Plate and Quraishi (1965) presented velocity distributions measured in various field crops and in their model canopies. Takeda (1966), applied different eddy viscosity assumptions to find various distributions of velocity within the canopy. The distributions take the form of power law or exponential equations depending upon the eddy viscosity assumption

used. The flow in the canopy develops entirely from a shearing action of the overlying fluid.

Generally, the flow in a porous medium is considered to be the direct result only of a pressure gradient. The driving force in the porous pipe boundary is expected to result from both the shear and pressure gradient. Beavers and Joseph (1967) studied a condition involving both a pressure gradient flow and a shear flow in a channel with an impermeable upper wall and a permeable lower wall. The equation for the velocity distribution within the channel was developed for the laminar flow case using a slip velocity at the permeable wall as a boundary condition. The velocity in the permeable block of the lower wall was assumed to follow Darcy's law and no attempt was made to determine a velocity distribution in the transition zone between the core and Darcy-type flow. Their model predicted the increase in mass flow rate in the channel reasonably well using one experimentally determined parameter. They also found that the friction factor in the channel decreased with increasing Reynolds number.

Eckert, et.al., (1955), Yuan and Brogen (1961) and Olsen and Eckert (1966) have studied turbulent flows over porous boundaries with suction or injection through the boundaries. Eckert, et.al., reported that increasing injection through one wall of a rectangular channel caused the average friction factor to decrease. Olsen and Eckert also observed a decrease in the friction factor with an increased injection through the walls of a circular porous tube. They also noted that at a Reynolds

number of 80000 without suction or injection, the friction factor for the porous tube was about 30% greater than what it would have been had the tube been smooth walled. In both cases, the characteristics of only the core flow were measured or modeled.

Muñoz and Gelhar (1968) have shown that the velocity distribution in the core of the porous pipe corresponds closely to that observed in pipes with rough walls. In the range of Reynolds numbers which was studied, the friction factor always increased with increasing Reynolds number. A mathematical model for the flow in the porous medium was developed with the motion being generated by a turbulent pressure field at the boundary. Because of the linearization of the equations of motion the momentum transfer term relating to the Reynolds stress vanished everywhere in the porous medium.

It is with this meager information on porous medium boundaries exposed to shear flows that the research project began. Although a number of studies have investigated related phenomena, other than in canopy flows, no velocity measurements have been made in a porous boundary exposed to a shear flow. The development of the measurement technique is described in the following chapter.

II. EXPERIMENTAL EQUIPMENT, PROCEDURES AND TECHNIQUES

2.1 Experimental Objectives and Approach

The principal objectives of the experimental portion of the study were to investigate the mechanism of shear flow in the porous boundary of a pipe and to investigate the interaction between the core flow and boundary flow. The shear flow mechanism is related to the velocity distribution within the porous boundary. The interaction of the two flow fields will be shown in Chapter 3 to be related through the friction factor. Thus, the experimental program was directed toward determining the depth to which the shearing effect of the core flow penetrates the porous boundary and affects the porous boundary flow.

The penetration depth was determined by directly measuring the seepage velocity within the porous foam boundary. Measuring the seepage velocity directly presented a unique challenge in itself. Direct measurements in an unconfined porous boundary with a turbulent shear flow superposed on it have not been attempted previously. Generally, in porous media, the seepage velocity is determined indirectly from discharge measurements. In permeameters and under special conditions, it has been determined by tracer techniques, i.e., releasing a tracer in the flow and measuring the travel time of the tracer between two points downstream.

Several methods of measuring the seepage velocity were attempted. Measurements were performed using hot wire anemometers, later referred to as unshielded probes, located in holes punched in the porous foam boundary. Attempts were made to use pitot tubes. Then, a tracer technique using helium was devised. The tracer technique required the

development of miniature hot wire anemometer probes. The probes were protected with a shield and are referred to as the shielded probes. The probes were used both as helium detectors and as anemometers.

The measurement of the porous foam properties were also a part of the experimental program. The determination of in situ permeability and the dispersion coefficients of the porous foam boundary were necessary to support the development of the velocity measurement technique.

2.2 General Description of Equipment

The basic air flow system used in this study has been described by Muñoz (1968). The system is shown schematically in Fig. 2-1 and includes an inlet box, the test pipe, a blower-motor unit with a variable speed drive and a damper for discharge control.

The test pipe, referred to as the porous pipe, consisted of about 40 ft of polyvinyl chloride (PVC) pipe of 12.75 in. OD with 0.406 in. wall thickness. The PVC pipe was lined with a commercially available polyurethane material, Scott Industrial Foam, which has a very open skeletal structure with a porosity of 97%. A sample of the foam is shown in Fig. 2-2. The foam used for the lining had a texture of 30 pores per inch and the in situ thickness was 1.20 in. The test section was located approximately 34 ft (43 diameters) from the beginning of the porous lining.

The instrumentation used to measure seepage velocities included hot wire anemometers and pitot tubes. Various recorders were used to collect the data. The descriptions, characteristics and operations of these instruments are given in the section detailing their use.

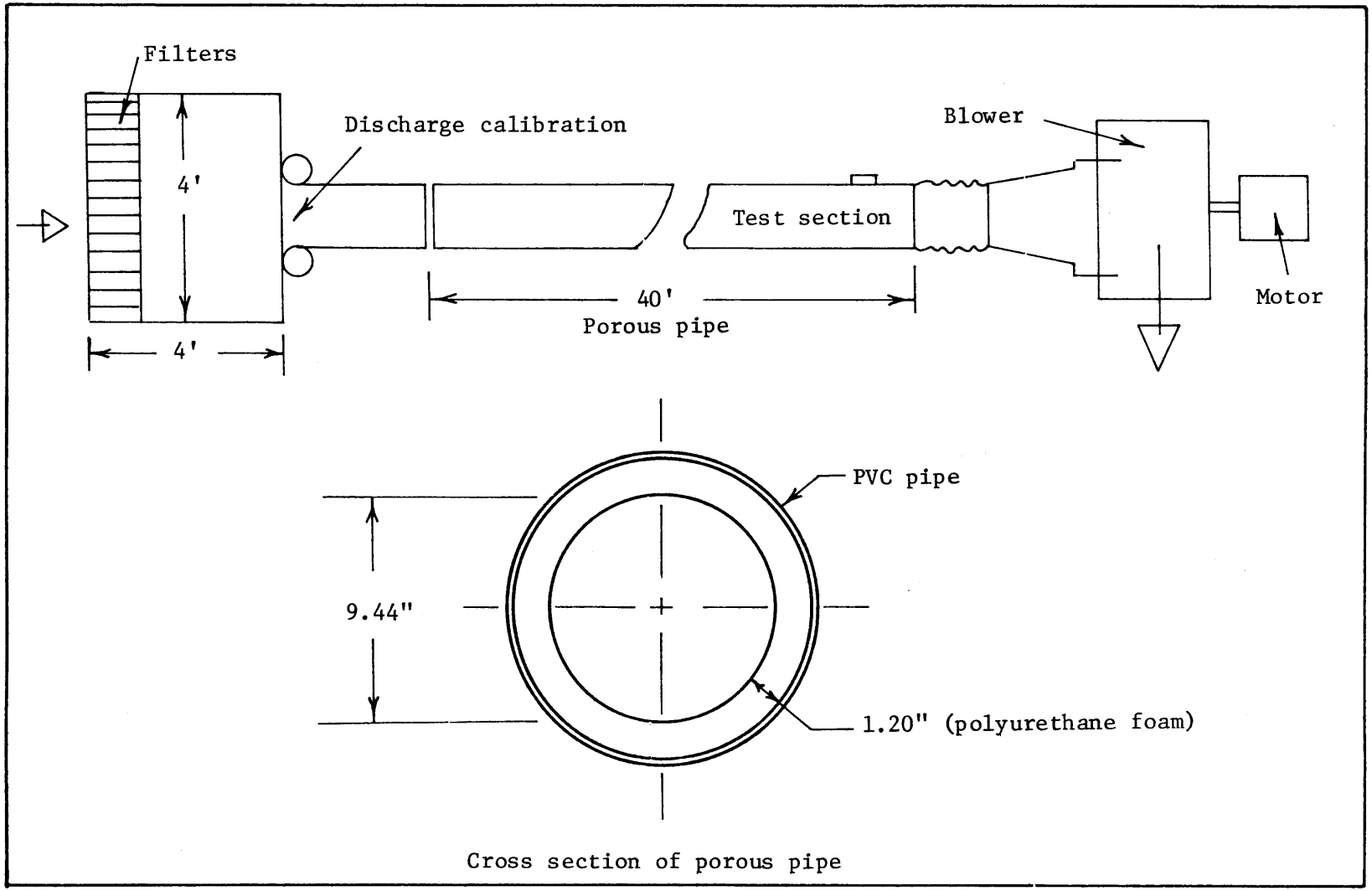

Fig. 2-1 Schematic diagram of the open circuit air flow system

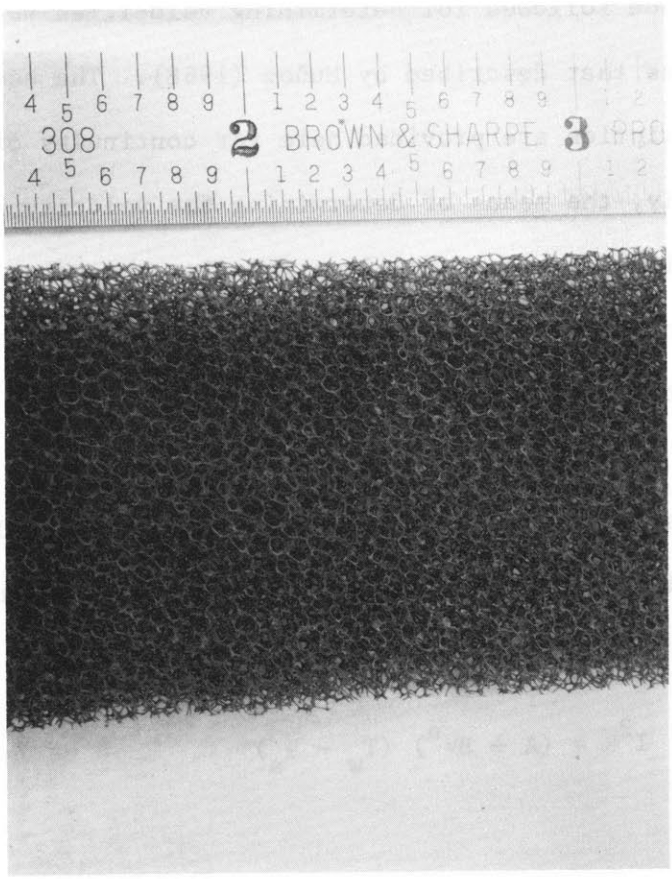

(Sample is 1/4 in. thick)

Fig. 2-2 Sample of porous foam

The anemometer was mounted on a United Sensor traversing unit Model 1108-18. Positions of the probe could be established with an accuracy of 0.01 in. using a vernier scale on the unit.

2.3 Hot Wire Anemometry

The method followed for determining velocities using the anemometer is the same as that described by Muñoz (1968). The essential features of that description are provided here for continuity of thought.

Basically, the means of determining the velocity of a fluid flowing past a hot wire anemometer involves relating the power required to keep the wire at a constant temperature to the heat transferred from the wire to the fluid. The theory of operation of hot wire anemometers is presented in books such as Hinze (1959) and in most anemometer manufacterers' literature, such as Flow Corporation Bulletin 94B (1964).

The empirical heat transfer relationship for a wire of infinite length is

$$I^2R = (A + BV^n)\ (T_w - T_a) \qquad (2\text{-}1)$$

where:

I = electric current in the wire

R = wire resistance

T_w = absolute wire temperature

V = fluid velocity normal to wire

T_a = fluid temperature

and A, B and n are constants depending upon the wire characteristics and are usually found by calibration. The expressions given by Collis and Williams (1959) are

$$A = C\pi \ell K_f \left(\frac{T_f}{T_a}\right)^{0.17} \tag{2-2}$$

$$B = D\pi \ell K_f \left(\frac{T_f}{T_a}\right)^{0.17} \left(\frac{d}{\nu_f}\right)^{n} \tag{2-3}$$

where:

K_f = thermal conductivity of the fluid

ν_f = kinematic viscosity

ℓ = wire length

d = wire diameter

C and D = constants

and the subscript, f, refers to the film temperature defined as the average temperature of the wire and fluid. Collis and Williams and Muñoz found a value of n = 0.45 gave the best correlation between the empirical relationship and calibration results. The value of n = 0.45 was also used in this study.

Using air properties represented by

$$\frac{\mu}{\mu_R} = \left(\frac{T}{T_R}\right)^{0.73} \tag{2-4}$$

$$\frac{K}{K_R} = \left(\frac{T}{T_R}\right)^{0.85} \tag{2-5}$$

$$\frac{\rho}{\rho_R} = \left(\frac{T_R}{T}\right)\frac{p}{p_R} \tag{2-6}$$

where μ = dynamic viscosity

ρ = density

p = pressure

and the subscript, R, refers to any reference value, the equation for the heat transfer relationship becomes

$$I^2 \frac{T_w - T_{ao}}{T_w - T_a} \left(\frac{T_{ao}}{T_a} \right)^{\frac{1.02}{2r} - 0.17} - I_o^2 = \frac{I_o^2}{a} \left(\frac{PV}{T_f^{1.73}} \right)^n \qquad (2\text{-}7)$$

where:

$$r = \frac{T_{fo}}{T_{ao}}$$

$$a = \frac{C}{D} \frac{\nu_R P_R^n}{dT_R^{1.73}}$$

and the additional subscript, o, indicates the conditions when there is no flow past the wire.

A computer program was written to assist in the data reduction. In the program, Eq. (2-7) was represented in the form

$$F(I) - I_o^2 = \frac{I_o^2}{a} F(V) \qquad (2\text{-}8)$$

with

$$F(I) = I^2 \frac{T_w - T_{ao}}{T_w - T_a} \left(\frac{T_{ao}}{T_a} \right)^{\frac{1.02}{2r} - 0.17}$$

$$F(V) = \left(\frac{PV}{T_f^{1.73}} \right)^n$$

The constant temperature anemometer system used in this experiment consisted of two channels of the model 900 series anemometers manufactured by Flow Corporation (Fig. 2-3). Mean voltages were measured with either two DC voltmeters, Digiter model 201 or the model 900-2D DC voltmeter which was one module of the model 900 series anemometer. RMS voltage were measured with another module of the 900 series, the model 900-5 RMS voltmeter which is a modified version of the Hewlett-Packard model 3400A true RMS meter. The modification extends the low frequency range to 2 Hz and provides an averaging time of 20 sec.

Two different types of probe configurations were used in the experiments. One configuration shown in Fig. 2-4 was a straight, single wire probe, 1/4 in. diameter, with the last 1 1/4 in. reduced to a diameter of 1/8 in. A polyurethane foam cylinder was glued to the reduced diameter portion of the probe to make the diameter 1/4 in. This was done to fill the 1/4 in. diameter hole punched out of the test section boundary in order to accept the probe. This probe will be referred to hereinafter as the unshielded probe.

The second probe configuration was a specially designed shielded probe. It will be described in detail in section 2.5.

The calibration apparatus is shown in Fig. 2-5. It consists of a bell-mouthed intake, approximately 4 ft of 2 in. ID plexiglass tubing, nozzles, and a blower controlled with a Variac transformer. The hot wire probes were calibrated in the core region near the bell-mouthed intake. The velocity in the 2 in. plexiglass tubing was determined from the pre-sure drop measured across different diameter nozzles depending upon the

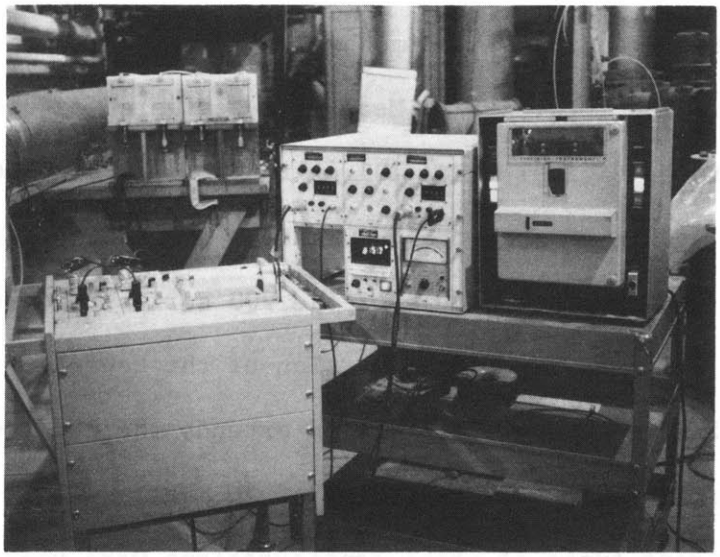

Fig. 2-3 Hot wire anemometry system and recording instruments

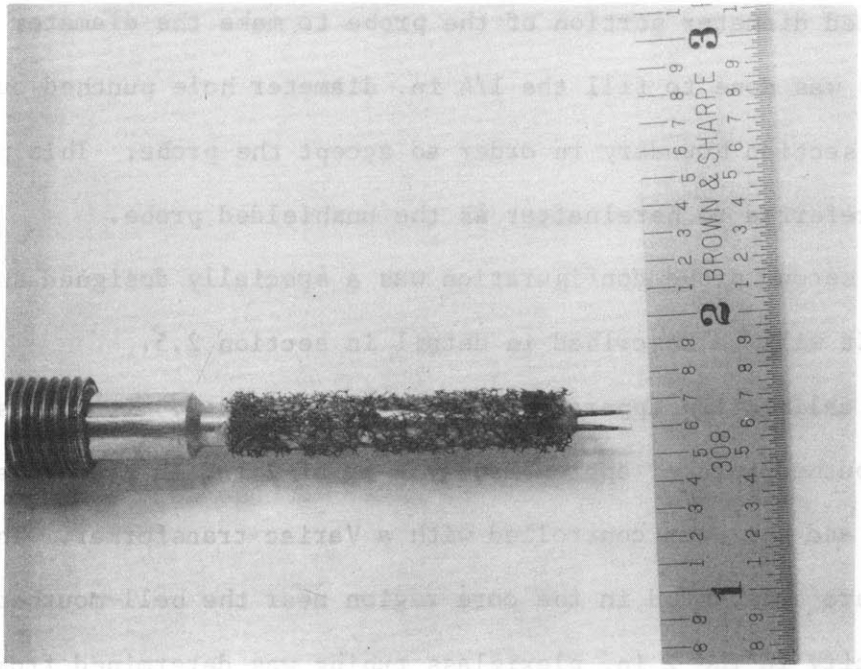

Fig. 2-4 Unshielded hot wire anemometer probe

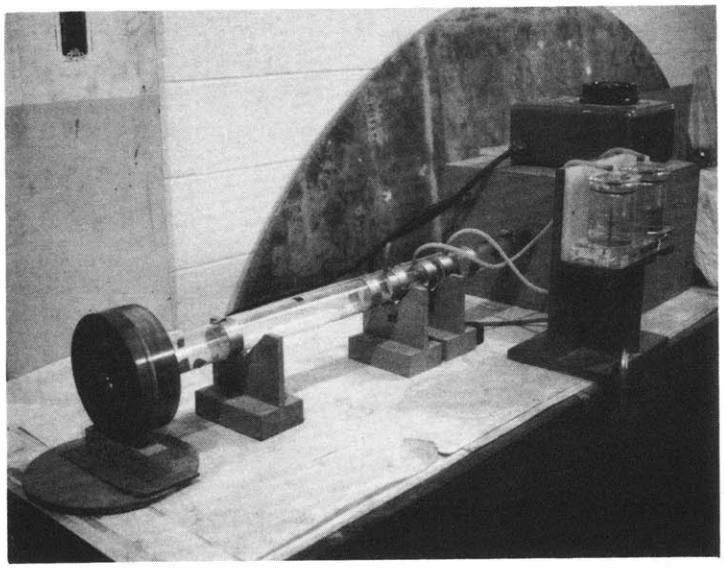

Fig. 2-5 Calibration unit

range of velocities required calibrated. The velocity at the nozzle throat, V_n, was computed using

$$V_n = C_n \sqrt{\frac{2g\ (\rho_w/\rho_a)\ (\Delta h_w/12)}{1 - (D_n/D_p)^4}} \qquad (2\text{-}9)$$

where

g = gravitational acceleration

ρ_w = density of water

ρ_a = density of air

D_n = nozzle diameter

D_p = pipe diameter

Δh_w = differential pressure across the nozzle measured in inches of water

C_n = nozzle coefficient

The coefficient, C_n, varied only slightly from nozzle to nozzle. An average value of $C_n = 1.01$ was used for all nozzles.

A typical calibration curve for the unshielded probe is shown in Fig. 2-6. The velocities for this calibration curve range from about 0.25 ft/sec to 12.5 ft/sec.

Velocity measurements in the porous foam were first carried out in the calibration unit. A polyurethane foam plug (30 pores per inch) approximately 10 in. long was placed inside the plexiglass tubing. The anemometer was inserted through a hole drilled in the wall of the tubing and into a 1/4 in. hole punched in the foam transverse to the flow. Velocities measured at the centerline of the tube are shown in Fig. 2-7. For seepage velocities below about 2 ft/sec, the anemometer

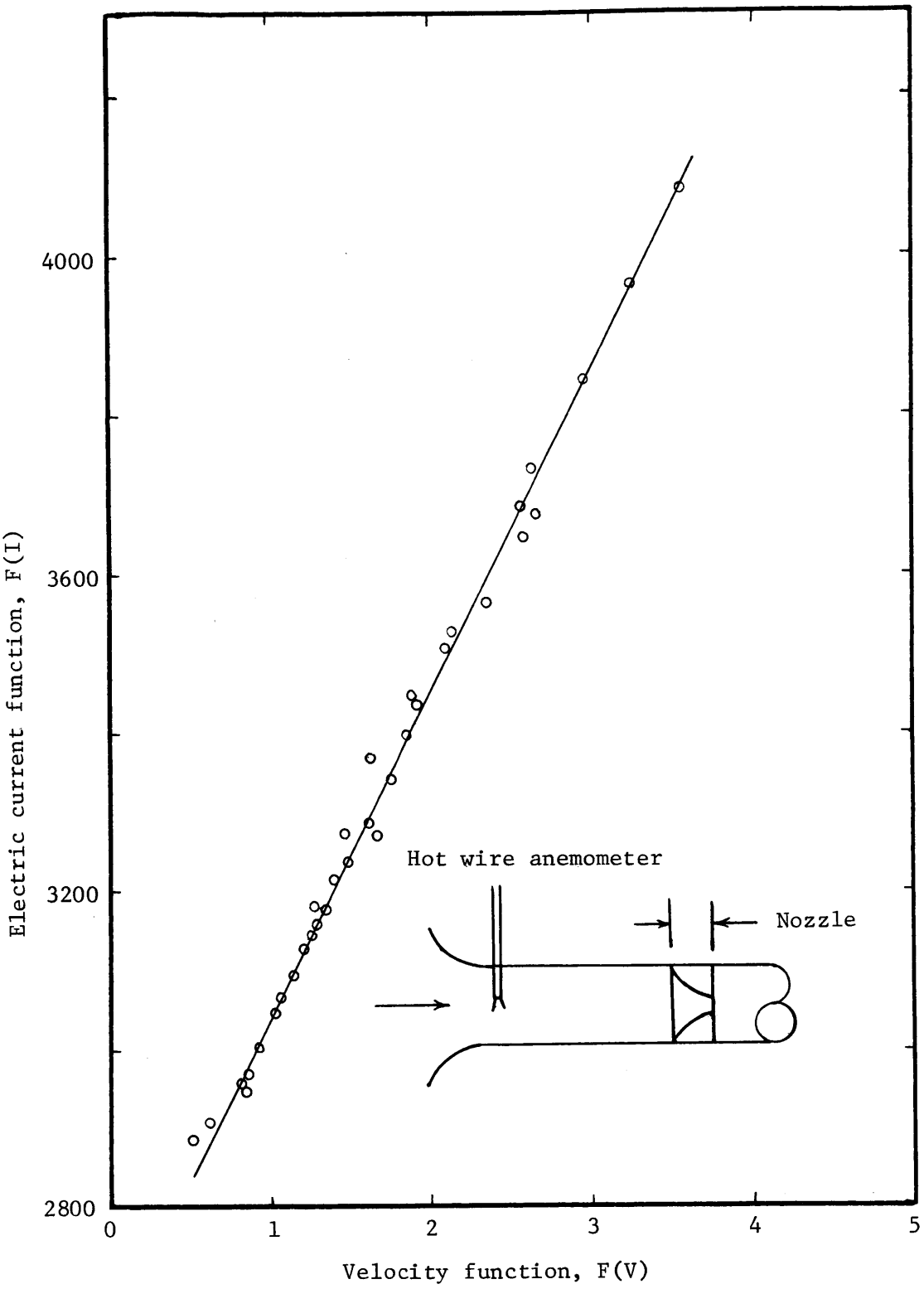

Fig. 2-6 Calibration curve for unshielded hot wire anemometer probe in air

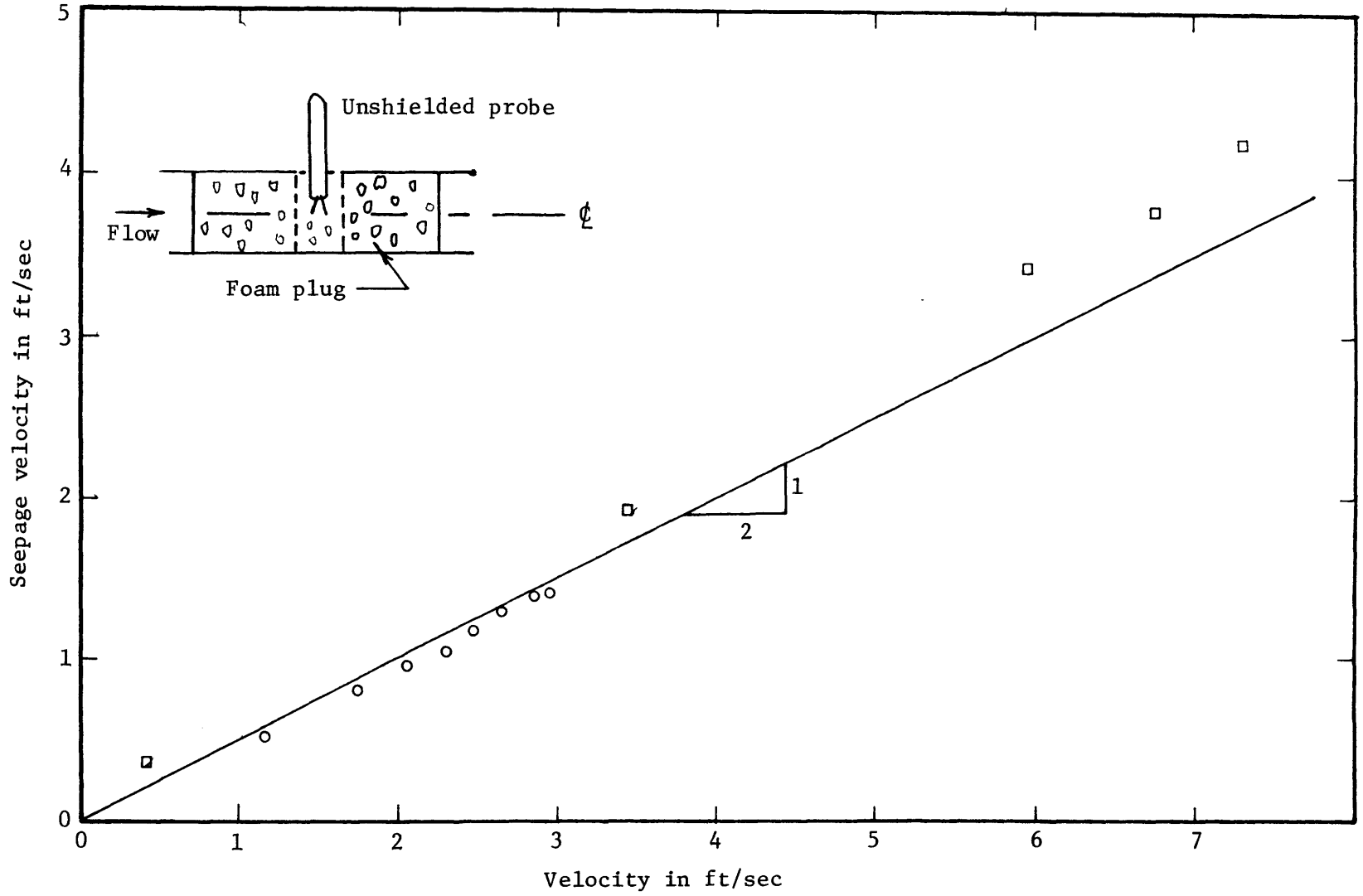

Fig. 2-7 Calibration of unshielded probe in a porous foam

indicated velocities within the hole approximately double the seepage velocity. This corresponds to the relationship that is predicted from potential flow analysis. Above 2 ft/sec, the correlation is not as good with the deviation from a 2:1 prediction increasing with increasing velocity.

By traversing the porous plug, considerable scatter in the velocity distribution was found. This scatter is evident in the two velocity profiles of Fig. 2-8. For both traverses the centerline velocity indicated by the unshielded probe is about 12 ft/sec even though the two profiles are for different seepage velocities of 5.85 ft/sec and 7.56 ft/sec.

A 1/4 in. diameter hole was punched in the polyurethane foam and aligned with a 1/4 in. hole in the wall of the PVC pipe to accept the hot wire probe. The probe was then traversed through the porous boundary. The probe position was referenced to the boundary of the porous medium near the clear core of the pipe. Positioning of the probe relative to this boundary was accomplished only by eye. The probe first was pushed through the hole until the probe needles extended beyond the surface of the porous material. Then, a straight edge was positioned parallel to the pipe centerline and as close to the probe as possible so that the straight edge indicated the nominal boundary of the porous medium. The probe then was drawn back into the porous medium until the hot wire was aligned with the straight edge.

Traversing the porous boundary was accomplished with the hole completely open between the probe and the core flow and with plugs of

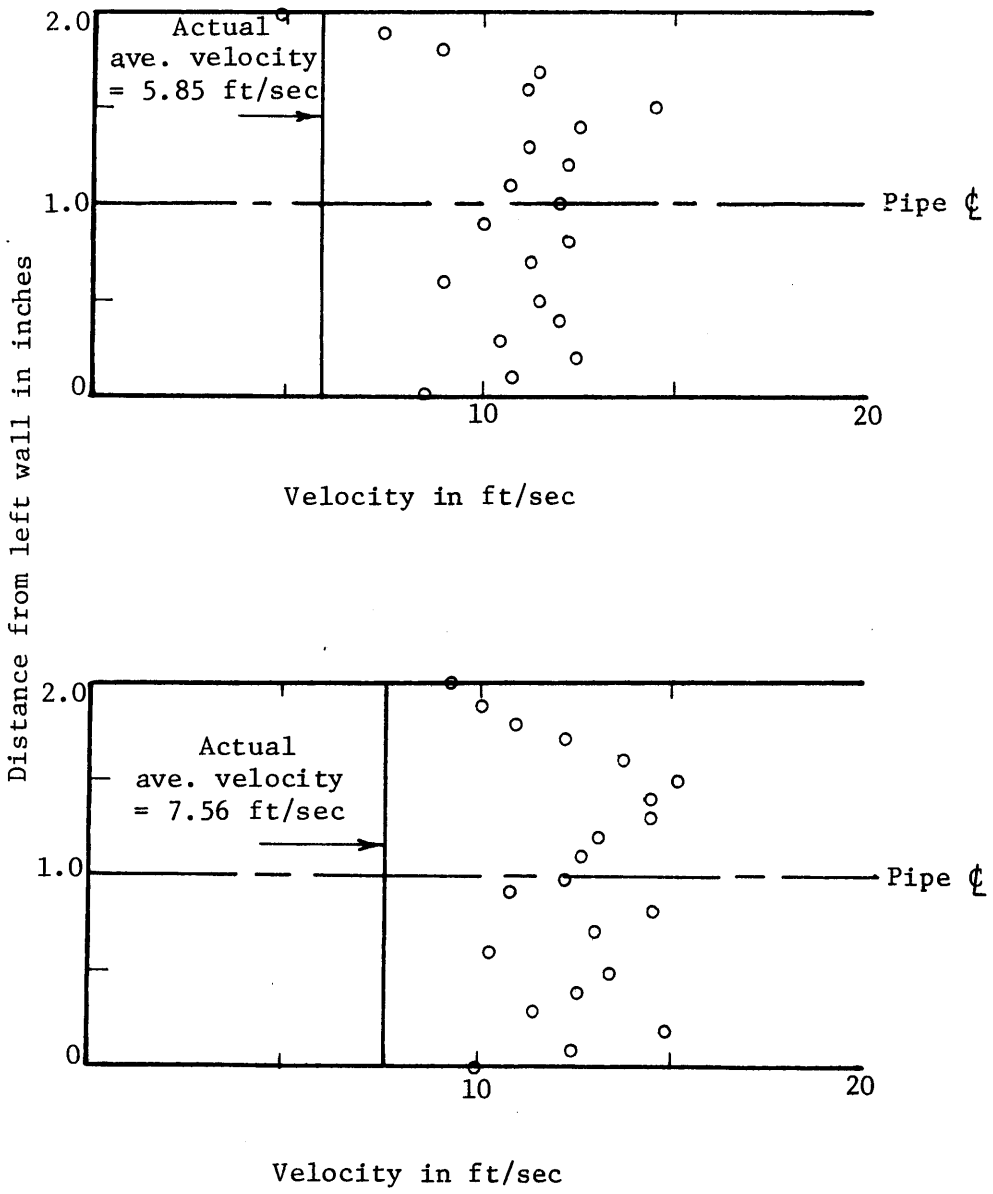

Fig. 2-8 Velocities indicated by the unshielded anemometer probe in a porous foam plug in the calibration unit

different lengths inserted into the holes as shown in Fig. 2-9. The plugs were installed by inserting a solid 1/4 in. diameter rod into the hole to a specified distance from the nominal porous boundary. The rod was referenced to the boundary in the same manner as the hot wire probe. The plug then was pushed into the hole and compressed against the rod. A tweezers was used to grasp the plug fibers and pull them slowly out of the hole until they were flush with the boundary. Porous plugs of lengths 0.15 in., 0.25 in., 0.55 in., and 0.75 in. were used in the tests. After the plug was installed, traversing of the probe began at a point 0.05 in. from the base of the plug and went to the impermeable boundary.

The velocities relative to the shear velocity, U_*, measured with the unshielded anemometer are shown in Fig. 2-10 for two Reynolds numbers. For these tests, there was no plug in the hole and the anemometer was traversed into the core flow. These tests indicated that the velocity decreased very rapidly in the first 10% of the porous foam (0.12 in.) and then had a gradual decrease throughout the rest of the depth.

Tests then were performed with a cylindrical porous plug inserted in the hole between the core flow and the unshielded probe. Results of these tests are shown in Fig. 2-11. These tests indicate the same trend of decreasing velocity with depth as was observed in the previous tests. Generally, the tests with the porous plug inserted gave velocities in the boundary which were slightly lower than those observed at the same location for runs with the plug removed. This reduction is most likely the result of the plug; however, the difference is well within the range of scatter observed in the 2 in. plexiglass tubing. Therefore, a

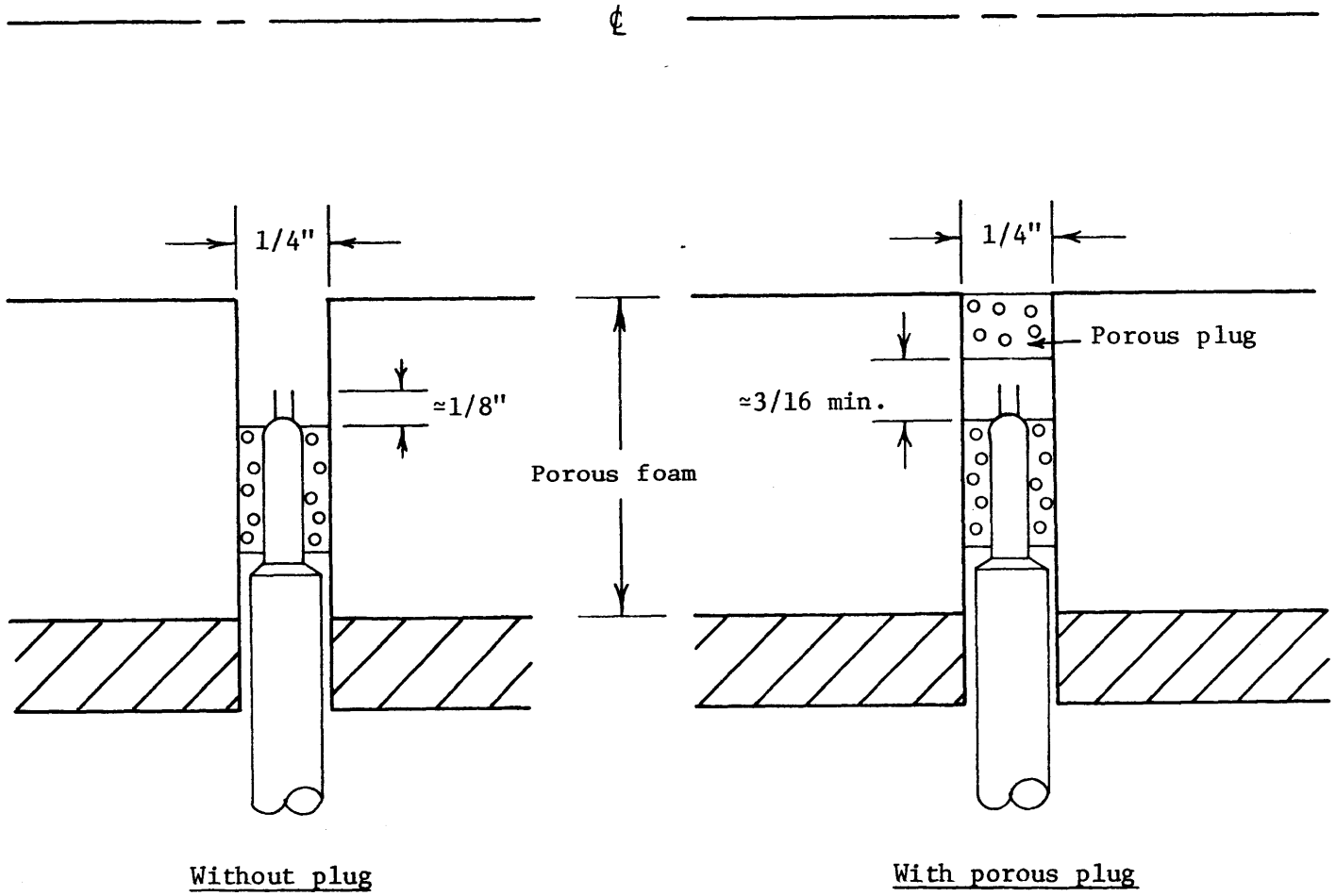

Fig. 2-9 Schematic representation of traversing the porous boundary with the unshielded probe

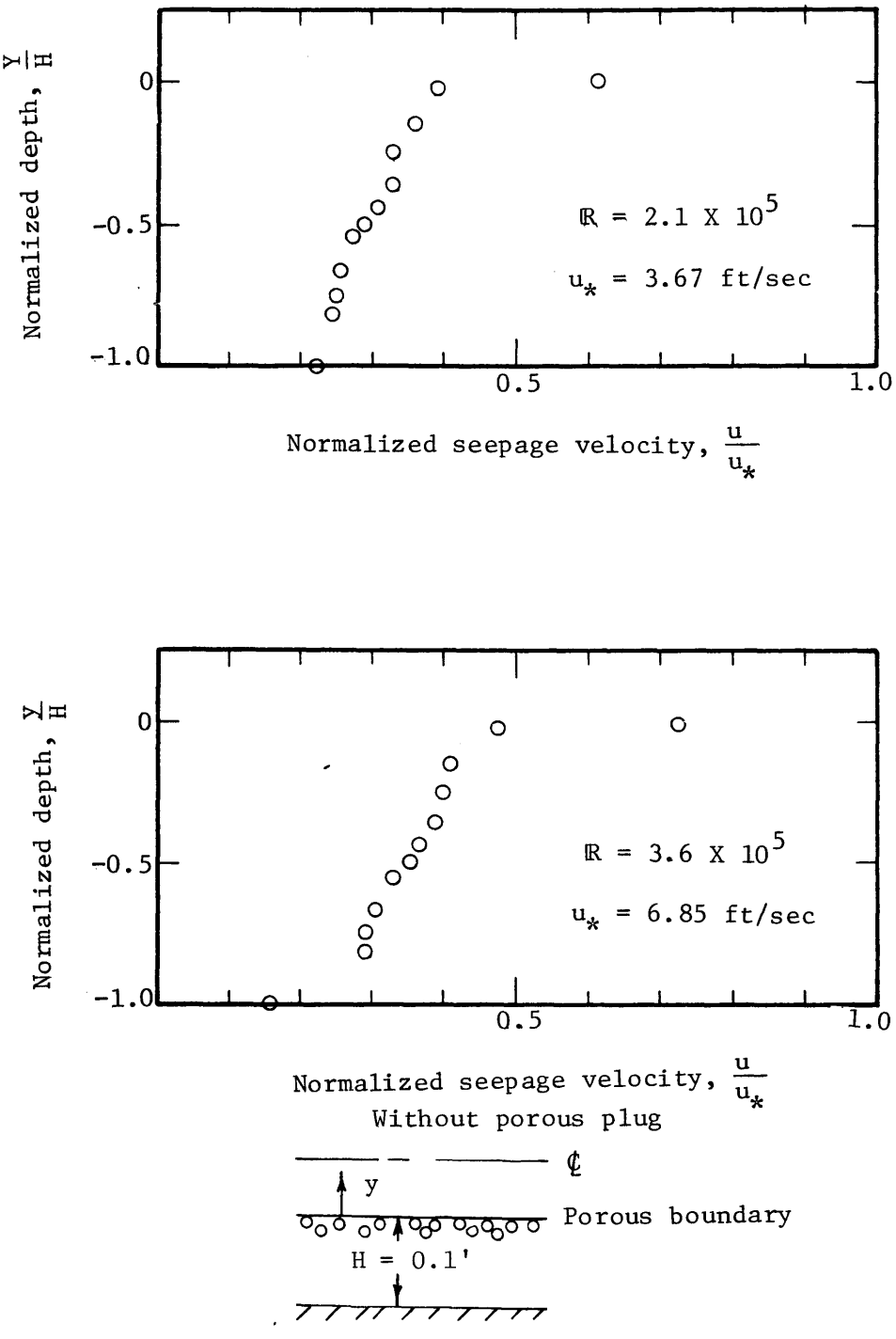

Fig. 2-10 Velocity distributions in porous foam boundary using the unshielded probe

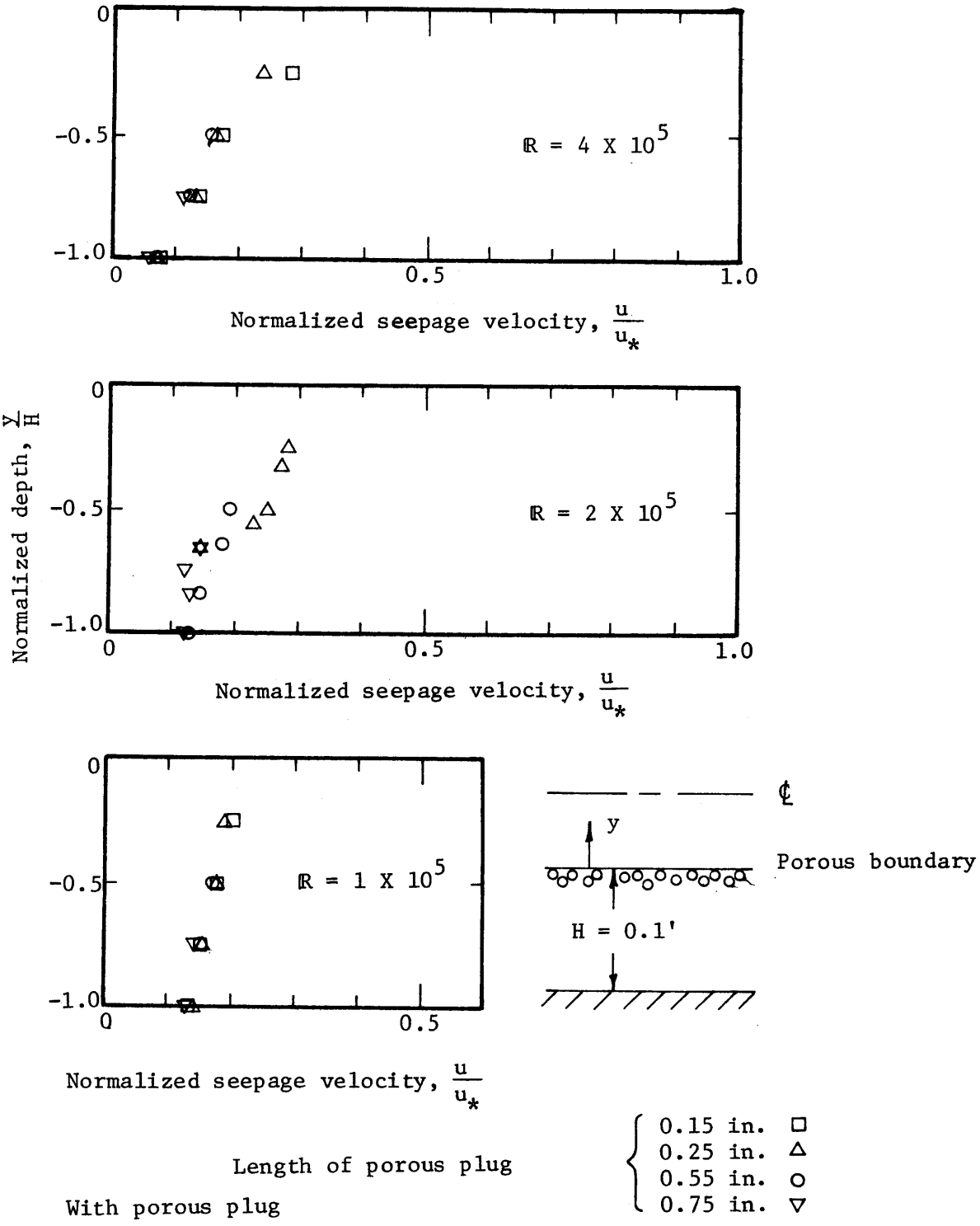

Fig. 2-11 Velocity distribution in porous foam using the unshielded probe

quantitative judgment of the porous plug effect could not be made.

Similar measurements of velocities and turbulence intensities in a porous medium with a superposed shear flow are not available. Therefore, any disturbing effect caused by the hole cannot be satisfactorily evaluated. Thus, an alternative method of making the measurements was sought. The following sections describe the methods attempted.

2.4 Pitot Tube Measurements

Measurements within a porous foam plug installed in the 2 in. diameter plexiglass calibration unit were performed using a pitot tube. The pitot tube used was 0.065 in. OD with a 0.030 in. diameter impact opening and four static openings of approximately 0.010 in. diameter. No attempt was made to install the pitot tube in the porous pipe because of the limitations and difficulties encountered while testing it in the calibration unit.

The pitot tube was inserted into a slit in the foam. Even with the slit, the pitot tube would become entangled in the foam and the foam would be pulled out of position whenever the pitot tube was moved. The resolution of the system was inadequate for the low velocities. For these reasons, the pitot tube was discarded as a means of making measurements in the porous foam.

2.5 Tracer Techniques

It is not known when tracers were first used to make velocity measurements. It may have been when man first watched a leaf floating down a small stream and noted how long it took for the leaf to travel from one rock to the next. Basically, this example illustrates the

tracer concept of making velocity measurements. The leaf acts as a tracer and the rocks as observation points. Generally, the tracer technique involves injecting a substance (tracer) with different properties than the fluid in which the measurements are desired. The travel time of the tracer between two points at a known distance apart is recorded. The velocity is determined by dividing the distance between the points by the travel time. Since tracer measurements have been made successfully in porous media, this measurement technique seemed to offer a reasonable chance of success and was pursued.

Most experiments using tracers in porous media have involved salt solution tracers in water such as the experiments performed by Hoopes and Harleman (1965). In water, the tracer is sensed by measuring the changes of the electrical conductivity of the salt solution as it passes a probe.

Different gases such as carbon dioxide and helium have been used as tracers in air. The procedure has been to draw a sample from the test section into a gas analyser to determine the tracer concentration. Various principles are used in gas analyzers, one of which is related to the change in thermal conductivity of gases. Rush and Forstall (1947) and Forstall and Shapiro (1950) used this type of gas analyser in experiments involving mixing of gases within a pipe and a jet, respectively. Although, a gas sample was not used in this experiment, the principle and apparatus involved are of primary importance in the measurement technique developed hereinafter.

Briefly, the thermal conductivity method of determining gas concentrations involves measuring the transfer of heat from a long thin electrically heated wire. Two conductivity cells form two sides of a Wheatsone bridge circuit. One cell contains a reference gas and the other the gas-tracer sample. The heat released from the wire is conducted through the gases to a heat sink. Unbalance of the bridge occurs because the greater rate of heat conduction in the gas-tracer sample cools the wire and changes its resistance, thus producing a bridge unbalance. The point of interest is that the hot wire anemometer reacts in a manner similar to the wire used in the conductivity cell. Therefore, by placing two hot wire anemometers in the flow, one downstream of the other, the probes would act as small thermal conductivity cells to sense the passage of a tracer gas injected in the flow upstream.

Consider the heat transfer relationship for a wire of infinite length, Eq. (2-1), with Eq. (2-2) and Eq. (2-3) substituted for A and B.

$$I^2R = C\pi\ell K_f \left(\frac{T_f}{T_a}\right)^{0.17} \left\{1 + \frac{D}{C}\left(\frac{d}{\nu_f}\right)^n V^n\right\} \left(T_w - T_a\right) \qquad (2\text{-}10)$$

This equation relates the output voltage of the hot wire to the air velocity and the properties of the air and wire. As the tracer gas passes, the anemometer output changes due to the change of fluid properties. Using the subscript, h, to indicate the quantities affected by the tracer, Eq. (2-10) becomes

$$I_h^2 R = C\pi \ell K_{fh} \left(\frac{T_f}{T_a}\right)^{0.17} \left\{1 + \frac{D}{C}\left(\frac{d}{\nu_{fh}}\right)^n V^n\right\} \left\{(T_w - T_a)\right\} \quad (2\text{-}11)$$

The assumptions implied in Eq. (2-11) are that the flow is steady and that injection of the tracer does not change the temperature or velocity. Dividing Eq. (2-11) by Eq. (2-10) and rearranging gives:

$$\frac{I_h^2 R}{I^2 R} = \left(\frac{K_{fh}}{K_f}\right) \frac{\frac{C}{D} + \left(\frac{Vd}{\nu_{fh}}\right)^n}{\frac{C}{D} + \left(\frac{Vd}{\nu_f}\right)^n} \quad (2\text{-}12)$$

Using previous hot wire calibrations, C/D was found to range from about 3000 to 10000 with an average of about 5000. The Reynolds number range for these experiments is $0.0025 < \frac{Vd}{\nu_f} < 2.5$. Therefore, it can be seen that even with a two or three-fold change of viscosity the influence on the voltage output of the anemometer will be negligible.

Since the hot wire output is generally read in terms of volts, $E = IR$, instead of power units, $P = I^2R$, Eq. (2-12) can be converted to voltage output by multiplying it by R and taking the square root. Subtracting one from both sides of the resulting equation and rearranging gives

$$\frac{E_h - E}{E} = \frac{\Delta E}{E} = \sqrt{\frac{K_{fh}}{K_f}} - 1 \quad (2\text{-}13)$$

This expression relates the relative difference in the output voltage of the hot wire to the thermal conductivity of the fluid and tracer.

Bird, Stewart and Lightfoot (1960) give the relationship between the thermal conductivity of a mixture of gases and their mole fractions as:

$$K_{mixture} = \sum_{i=1}^{n} \frac{x_i K_i}{\sum_{j=1}^{n} x_j \phi_{ij}} \tag{2-14}$$

where K_i = thermal conductivities of the pure components

x_i = the mole fractions

and

$$\phi_{ij} = \frac{1}{\sqrt{8}} \left(1 + \frac{M_i}{M_j}\right)^{-1/2} \left\{1 + \left(\frac{\mu_i}{\mu_j}\right)^{1/2} \left(\frac{M_j}{M_i}\right)^{1/4}\right\}^2 \tag{2-15}$$

where M_i = molecular weights of the gases

μ_i = viscosities

In a binary system, the mole fractions of two species, A and B, are related to their concentrations, C_A and C_B, by

$$x_A = \frac{C_A/M_A}{\frac{C_A}{M_A} + \frac{C_B}{M_B}}, \quad x_B = \frac{C_B/M_B}{\frac{C_A}{M_A} + \frac{C_B}{M_B}} \tag{2-16}$$

Considering equations (2-14) through (2-16) it can be deduced that the concentration of a tracer in the flow can be determined from the output of the hot wire anemometer. Since equation (2-14) is independent of the velocity of the air, the hot wire anemometer does not have to be calibrated but only properly balanced if just the concentration of

tracer is desired. This can be highly desirable, since changes in the velocity calibrations can be quite large over long operating times.

Helium was selected as the tracer gas for these experiments. Its thermal conductivity is an order of magnitude higher than that of air and its principal constitutes, nitrogen and oxygen.

The relative voltage difference related to specific values of helium concentration in air was evaluated using Eqs. (2-14) through (2-16). The properties of helium and air used in the program are given in Table 2-1 and were obtained from Weast (1968).

Table 2-1

Properties of Helium and Air

Species	n	M dimensionless	$\mu \times 10^7$ ($g\ cm^{-1}\ sec^{-1}$)	$K \times 10^7$ ($cal\ sec^{-1} cm^{-1}\ K^{-1}$)
Air	1	28.966	1789	60.5
Helium	2	4.003	1941	355.0

The relationship between the anemometer output voltage difference and the concentration of helium in air is given graphically in Fig. 2-12. The relationship is practically linear over the range shown. Therefore, when using the hot wire as a helium sensor where absolute concentrations are not essential, the change in output voltage gives a direct measure of the relative concentration.

To test the tracer technique, an injection system was devised and constructed and special miniature probes were developed. The injection

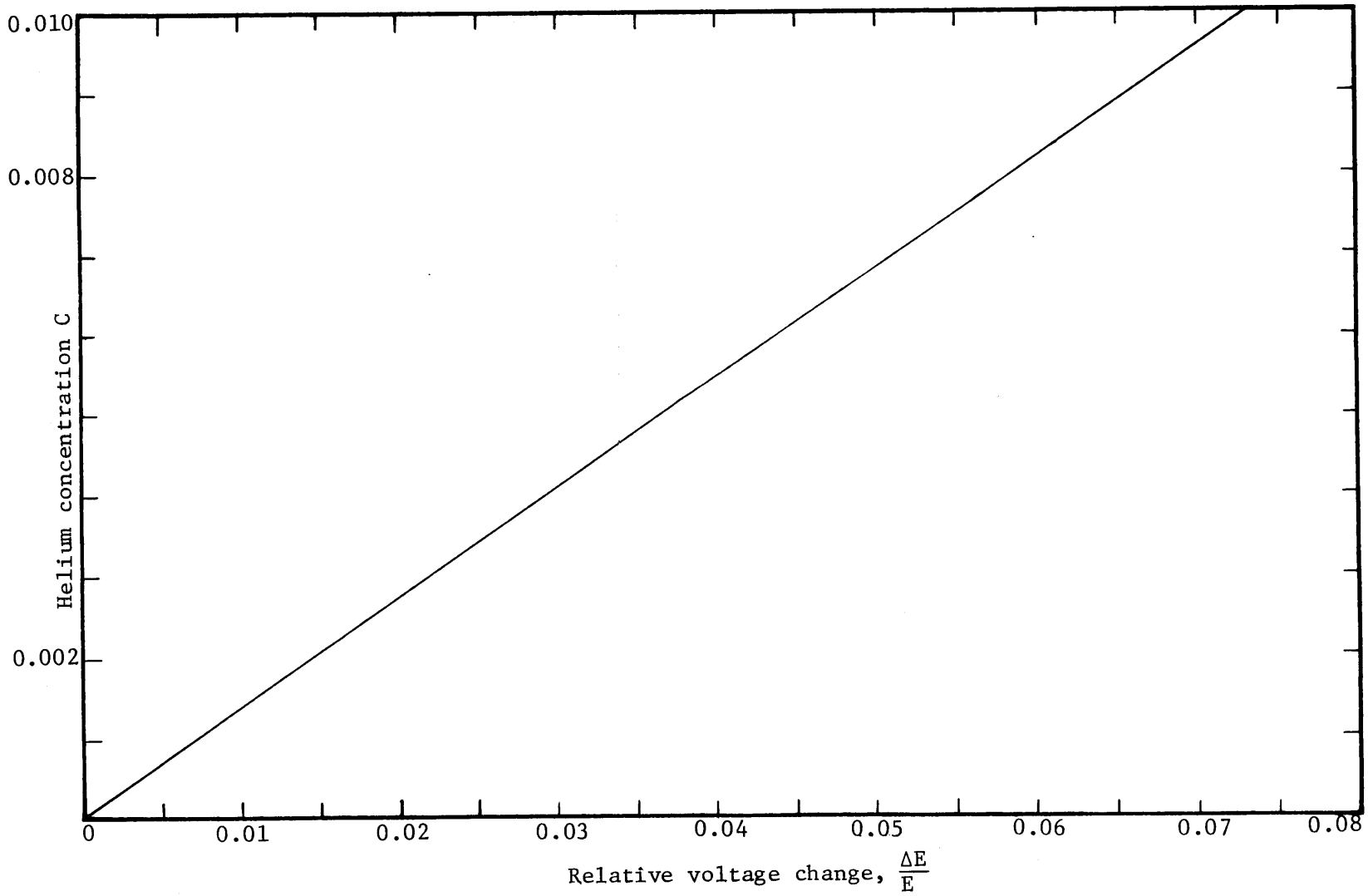

Fig. 2-12 Dependence of hot wire anemometer output on helium concentration

system is shown in Fig. 2-13 installed in the porous pipe. It consisted of a tank of compressed helium, a pressure regulator, polyvinyl tubing, a solenoid operated valve, and a modified hypodermic needle. The pressure regulator reduced the pressure in the tank to working pressures in the range of about 3 psi to 50 psi.

The solenoid operated valve, Automatic Switch Co. (ASCO) catalog no. 8262B1 with 3/64 in. orifice, was controlled by an electric switching unit which could provide a 10 millisecond pulse for "instantaneous" injections. Continuous injections could be achieved by bypassing the switching unit. The circuit diagram for the switching unit is shown in Fig. 2-14. Initially, the switching unit was used only for manually controlled instantaneous injections. In later stages of the test program, a periodic instantaneous injection was required. This was accomplished by using a rotary switch driven by a motor with a variable speed control which replaced switch, S2.

A no. 20 hypodermic needle was modified for use as the injector and is shown in Fig. 2-15. The injector was made by bending the needle to form a right angle near the tip. Epoxy cement then was daubed around the needle in the vicinity of the tip. The epoxy cement and right angleprotusion of the needle then were filed down to approximately 0.05 in. The needle then could be inserted through the pores of the polyurethane foam. The foam did cling to the injector slightly during changes in position. But, by moving slightly past the desired position and then back to it, no distortion of the foam was evident.

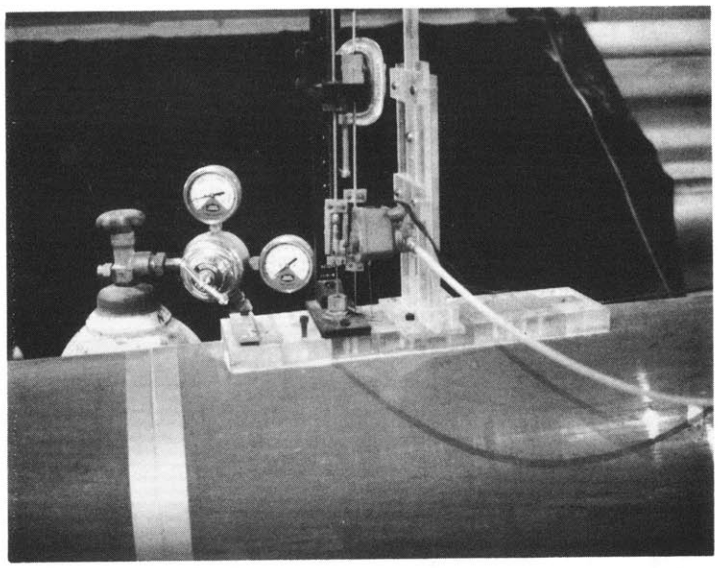

Fig. 2-13 Helium injection unit installed on porous pipe

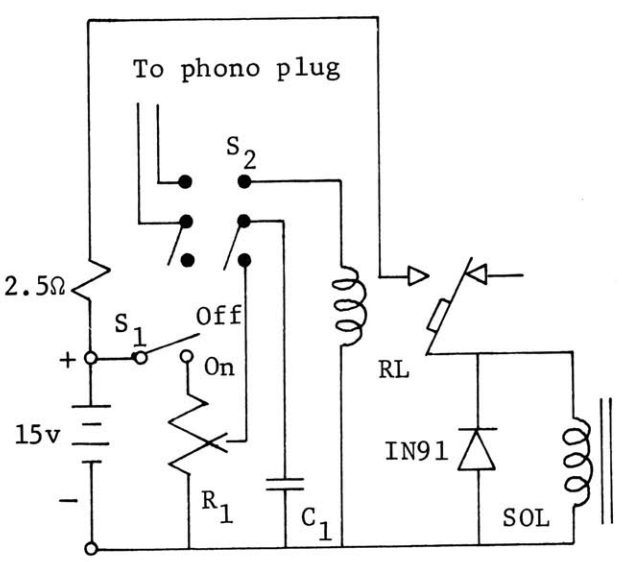

RL = Magnecraft relay

S_1 = SPST switch

S_2 = DPDT switch

R_1 = 10 KΩ potentiometer

C_1 = 100 μf capacitor

SOL = ASCO 8262B1 solenoid valve, 12 VDC

Fig. 2-14 Circuit diagram for controlling solenoid valve

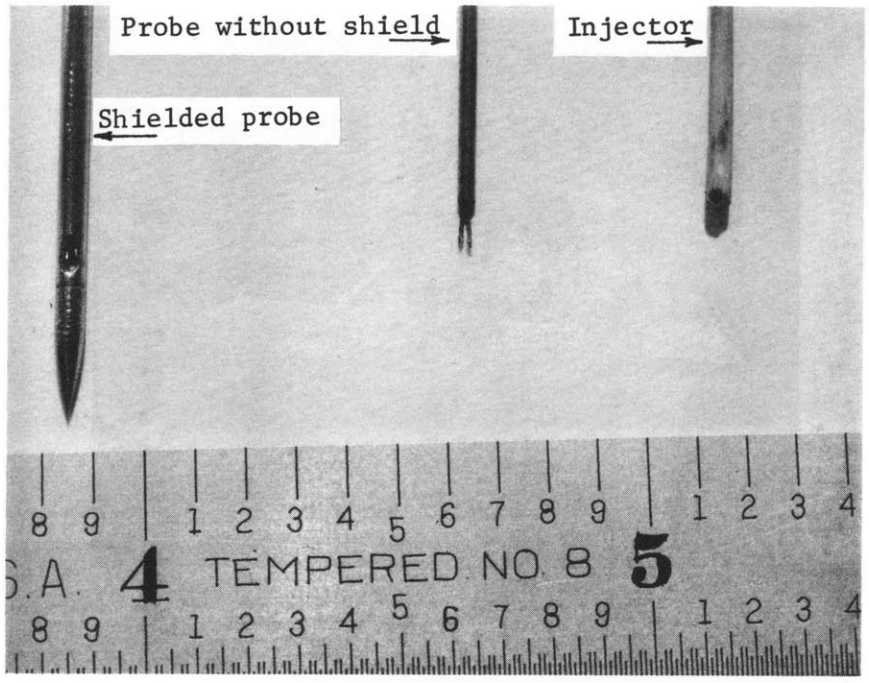

Fig. 2-15 Helium injector and shielded hot wire anemometer probes

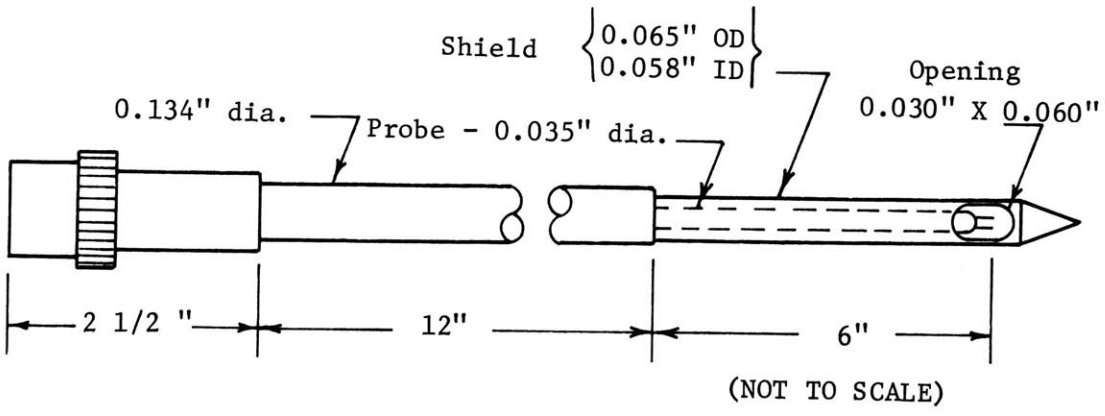

Fig. 2-16 Shielded hot wire anemometer probe

One of the main objectives of the tracer measurements was to evaluate the measurements made with the 1/4 in. diameter unshielded probe. Therefore, it was decided that a small tracer-sensing probe which could be inserted through the pores of the foam was required. Commercial probes were not available which could be used directly for measurements in the porous foam. Therefore, miniature shielded probes were developed especially for these experiments. The probes themselves are modified versions of Flow Corporation F-1-E02 probes as shown in Fig. 2-15 and 2-16. The overall length of the probes is about 18 in., 12 in. of which is 0.134 in. diameter and 6 in. of 0.035 in. diameter. A pointed shield of 0.058 in. OD tubing fitted with two openings, 0.060 in. in the axial direction by 0.030 in., covered the 0.035 in. diameter portion of the probe. When the shield was touching the shoulder of the larger diameter portion of the probe the hot wire of the probe was aligned with the center of the openings. With this configuration the probe could be inserted directly into the polyurethane foam. The foam adhered slightly more to the probes than to the injector needle. This partly was due to the larger diameter stem and the slight indentation caused by the openings. Any observable deformation of the foam was eliminated by following the same positioning procedure as used for the injector. If the probe was pushed through the porous pipe boundary and the positioning procedure was not used, the foam formed a mound around the probe. This mound was approximately 0.03 in. to 0.05 in. with an estimated diameter of about 3/8 in. If the probe was pulled

back into the foam, an indentation of about the same magnitude as the mound was observed.

The tracer technique involves measuring the travel time between two points in space. The velocity can be determined by dividing the distance between the two points by the time of travel between the peak concentrations observed at the two points. Therefore, the two probes were mounted on the traversing unit so that they were moved in unison to any location. The solenoid valve and injector needle were mounted in a sliding bracket which could be attached to the porous pipe upstream of the shielded probes. The shielded probes and injector needle were referenced to the nominal boundary of the porous foam in the same manner as the unshielded probe.

The equipment used to record the concentrations sensed by the two hot wire probes is shown in Fig. 2-17. A schematic diagram of the system is shown in Fig. 2-18. The equipment includes the hot wire anemometer units, Flow Corporation series 900, a strip chart recorder, Sanborn model 296 recorder, and a magnetic tape recorder, Precision Instrument model PS-207A portable FM tape recorder. The frequency response of the system was limited to 125 cps by the Sanborn recorder. This was more than sufficient for recording the passing of a helium pulse. In fact, when the probes were inserted into the porous pipe, a R-C filter circuit was installed between the hot wire anemometer output and the Sanborn recorder to eliminate the higher frequency voltage fluctuations caused by turbulence in the flow. The RC circuit reduced

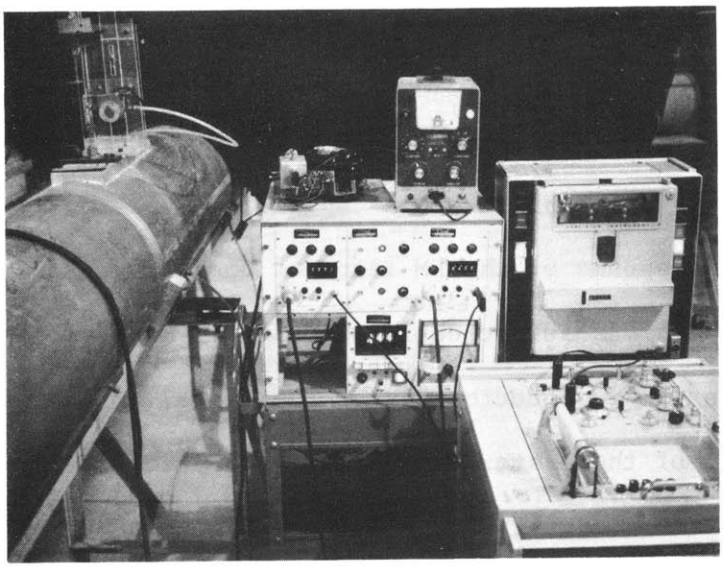

Fig. 2-17 Equipment for sensing and recording helium concentrations in a porous medium

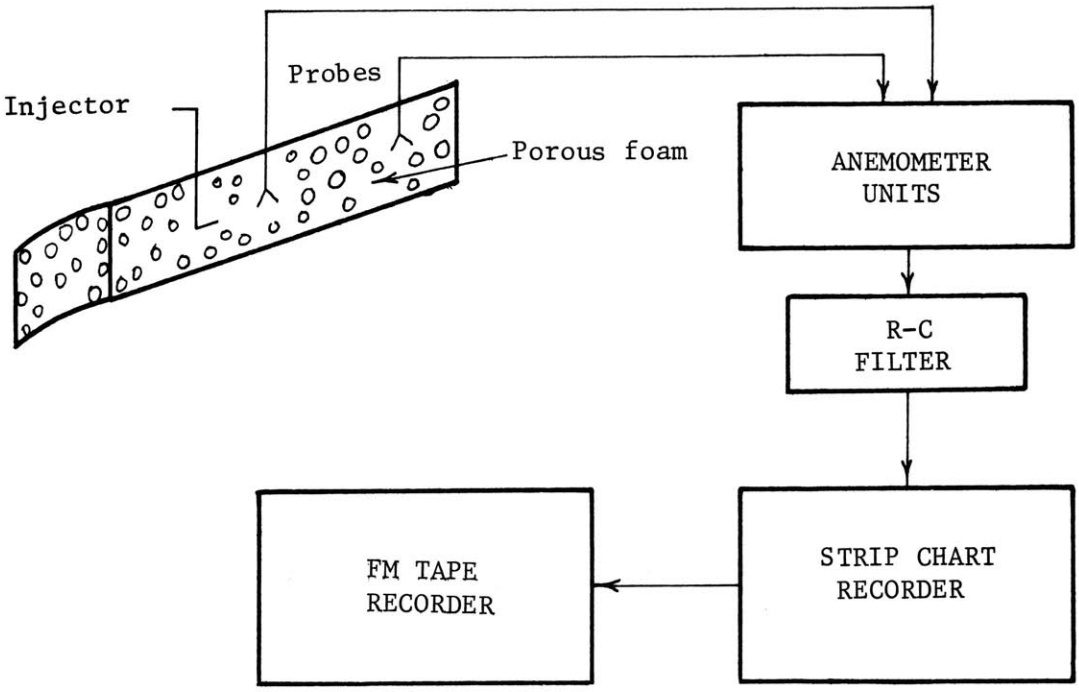

Fig. 2-18 Schematic diagram of tracer sensing and recording equipment

the signal at 50 Hz by 3 db.

The output of the Sanborn recorder was played into the FM tape recorder operating at 7 1/2 in./sec. This was done to utilize the suppression voltage and amplification capabilities of the Sanborn recorder. The frequency response of the FM recorder operating at 7 1/2 in./sec was 2500 Hz which was sufficiently above the limits of the Sanborn recorder to insure reproducibility of the signal.

Operation of the system began after the anemometers were adjusted. This amounted to balancing of the bridge circuit and checking the frequency response of the wires according to the manufacturer's instructions, Flow Corporation Bulletin No. 900A (1967). The frequency response of the shielded probes was about 12 kHz which was determined using a square wave calibration signal built into the unit. Having performed this operation the shielded probes could be operated directly as anemometers if desired or used as the helium detectors.

The peak concentration of the helium tracer travels with the mean velocity along a line parallel to the flow. Therefore, the shielded probes and injector were positioned in the porous pipe along a line parallel to the centerline of the pipe for all runs in which the velocity was required.

The tracer technique was first checked on the calibration unit. A typical recording of the helium passing the shielded probes is shown in Fig. 2-19. In Fig. 2-20 the seepage velocity in the porous foam plug determined by dividing discharge by the area and porosity

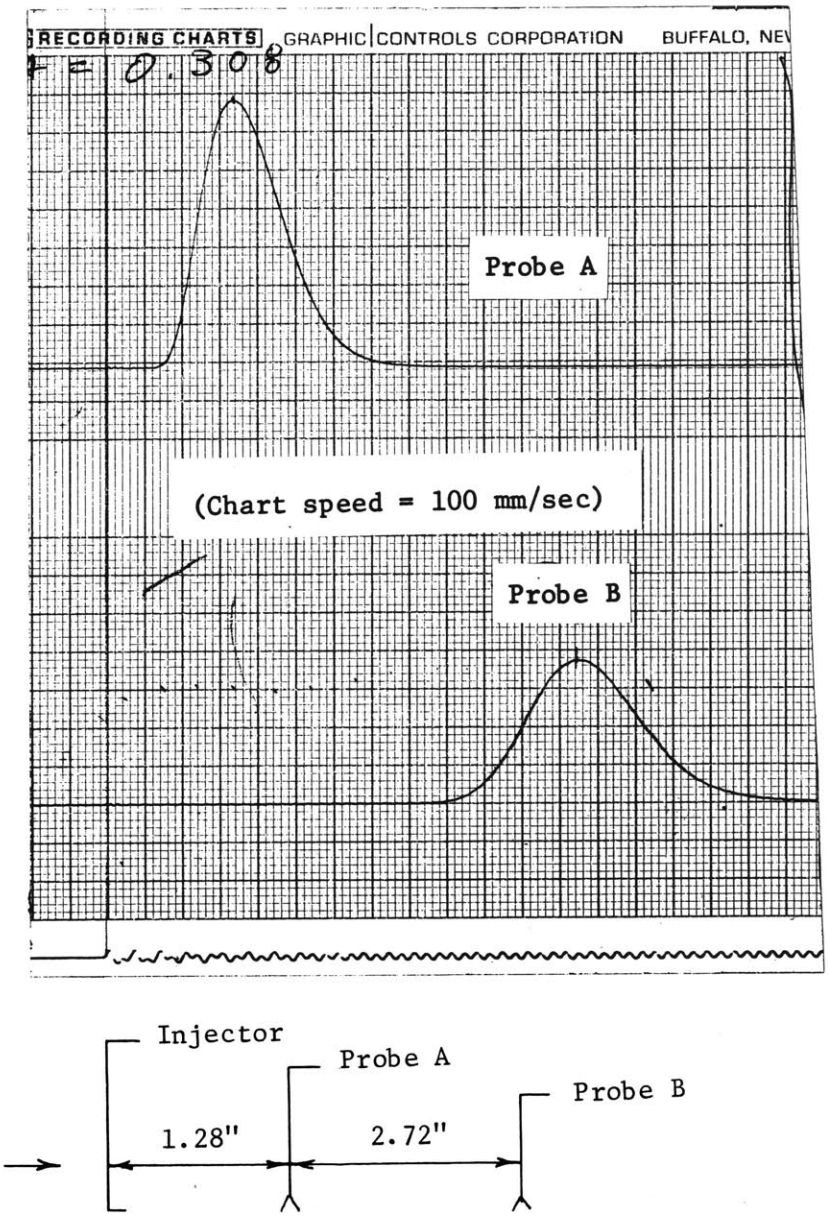

Fig. 2-19 Recording of helium tracer passing shielded probes in calibration unit

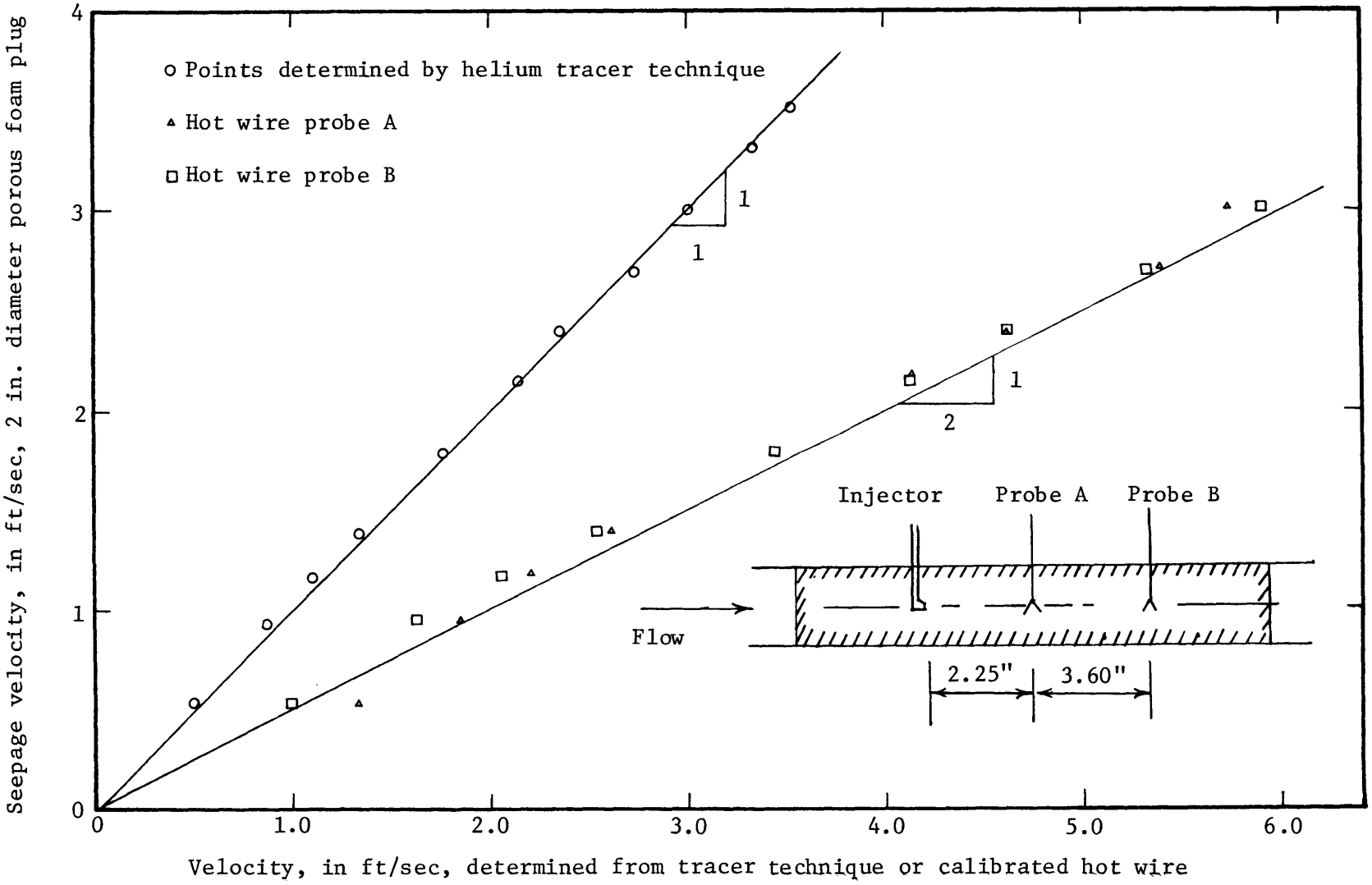

Fig. 2-20 Calibration of the shielded hot wire anemometer probes

(0.97) is compared to the seepage velocity determined by the tracer technique and the velocities indicated using the shielded probes directly as anemometers. It is interesting to note that the measurements by the tracer technique show close agreement with the actual specific discharge and that the velocities sensed through the openings of the shield show a close agreement with the average velocity (twice the seepage velocity) predicted from potential flow analysis for a clear circular opening in a homogeneous porous medium. To determine what effect the jet issuing from the injector needle had on the velocity measurements, tests were performed in the calibration unit using several injection pressures. The pressure indicated at the pressure regulator was used as a reference. Pressures of 4, 10, 14, and 18 psi were tried. The seepage velocities determined at two of the pressures, 4 and 18, are shown in Fig. 2-21. The velocities in these tests were determined from an average of these separate pulse travel times.

The effects of helium buoyancy in the flow field were evaluated by measuring the vertical concentration distribution in the porous pipe. Helium was continuously injected at several positions in the porous boundary. The shielded probes were then traversed vertically through the boundary at two positions downstream. Results of these traverses are shown in Fig. 2-22. The continuous injection gives a better indication of the buoyancy effects. Since more mass is injected into the system than with a pulse, buoyancy effects should be more obvious if they exist. These results indicated that buoyancy effects are negligible in the distance covered in these tests.

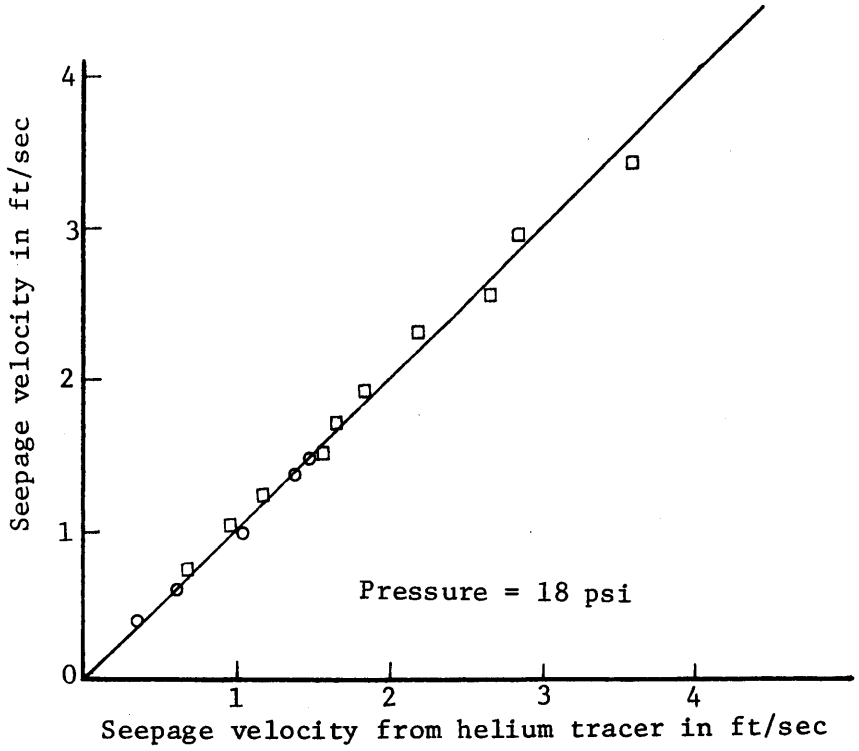

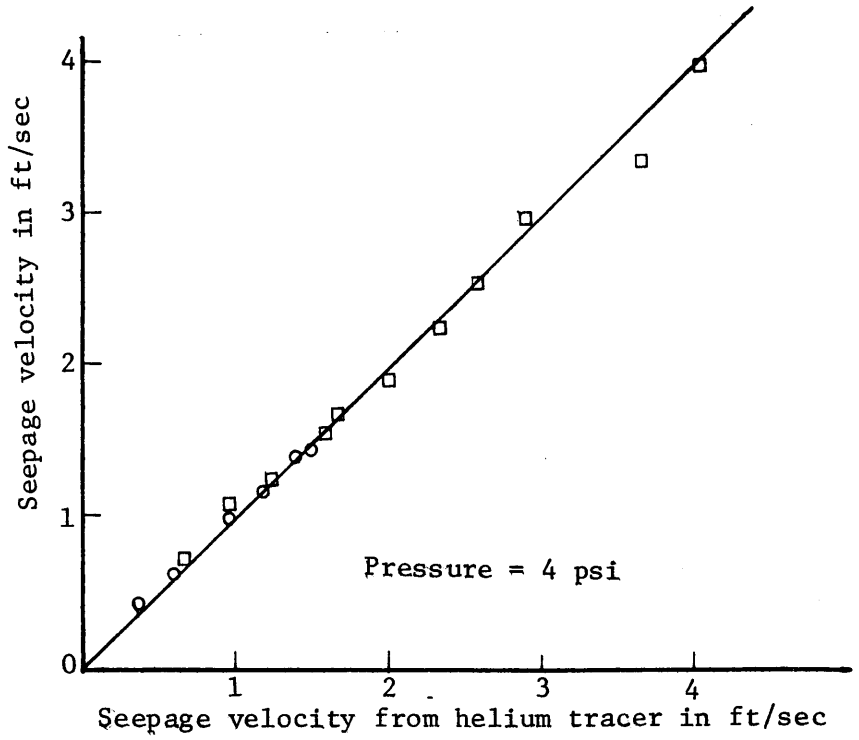

Fig. 2-21 Seepage velocity determined using different injection pressures

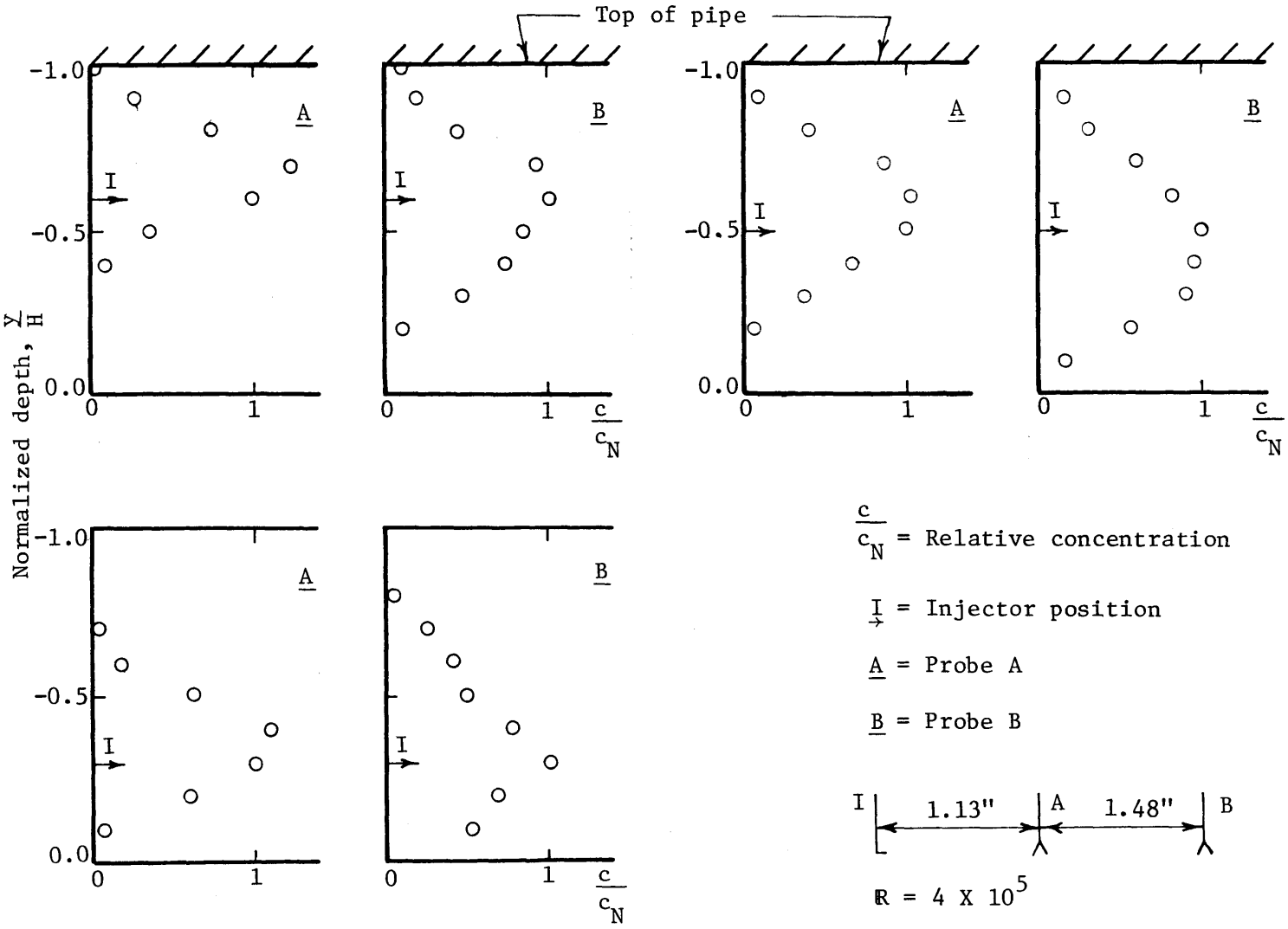

Fig. 2-22 Helium concentrations downstream from a continuous source

A significant difference in the anemometer output wave form was evident when the equipment was moved from the calibration unit to the porous pipe. A sample of the output wave form recorded in the calibration unit was shown in Fig. 2-19.

Samples of the recorded signal for different positions in the porous boundary are shown in Figs. 2-23 and 2-24. The difference is due primarily to the turbulent fluctuations of velocity present in the porous pipe. The signals at positions Y/H = -0.1, -0.2 and -0.3 are typical of the signals recorded at these positions and show the difficulties of determining accurate travel times from them. The signals recorded in the rest of the boundary, $-0.4 > Y/H > -1.0$, are similar to those shown for Y/H = -0.6 and the time between peaks is easily measured. Tests were performed by traversing the injector and the shielded probes through the boundary. Manually controlled pulses were used in the tests. Where the peaks in the concentration curves were identifiable, the velocities were calculated using average travel times established from two to five pulses. Results of these tests are shown in Fig. 2-25 where the velocity is normalized with the shear velocity, u_*, and the depth is normalized with the total thickness of the porous foam, H. These velocity profiles indicate that a relatively uniform velocity exists over most of the porous foam boundary. Apparently, the shearing effect of the core flow does not penetrate beyond about Y/H = -0.3 or -0.4. Comparison of the profiles of Fig. 2-25 with those of Figs. 2-10 and 2-11 indicates that the hole punched in the foam affects the velocities measured by the anemometer

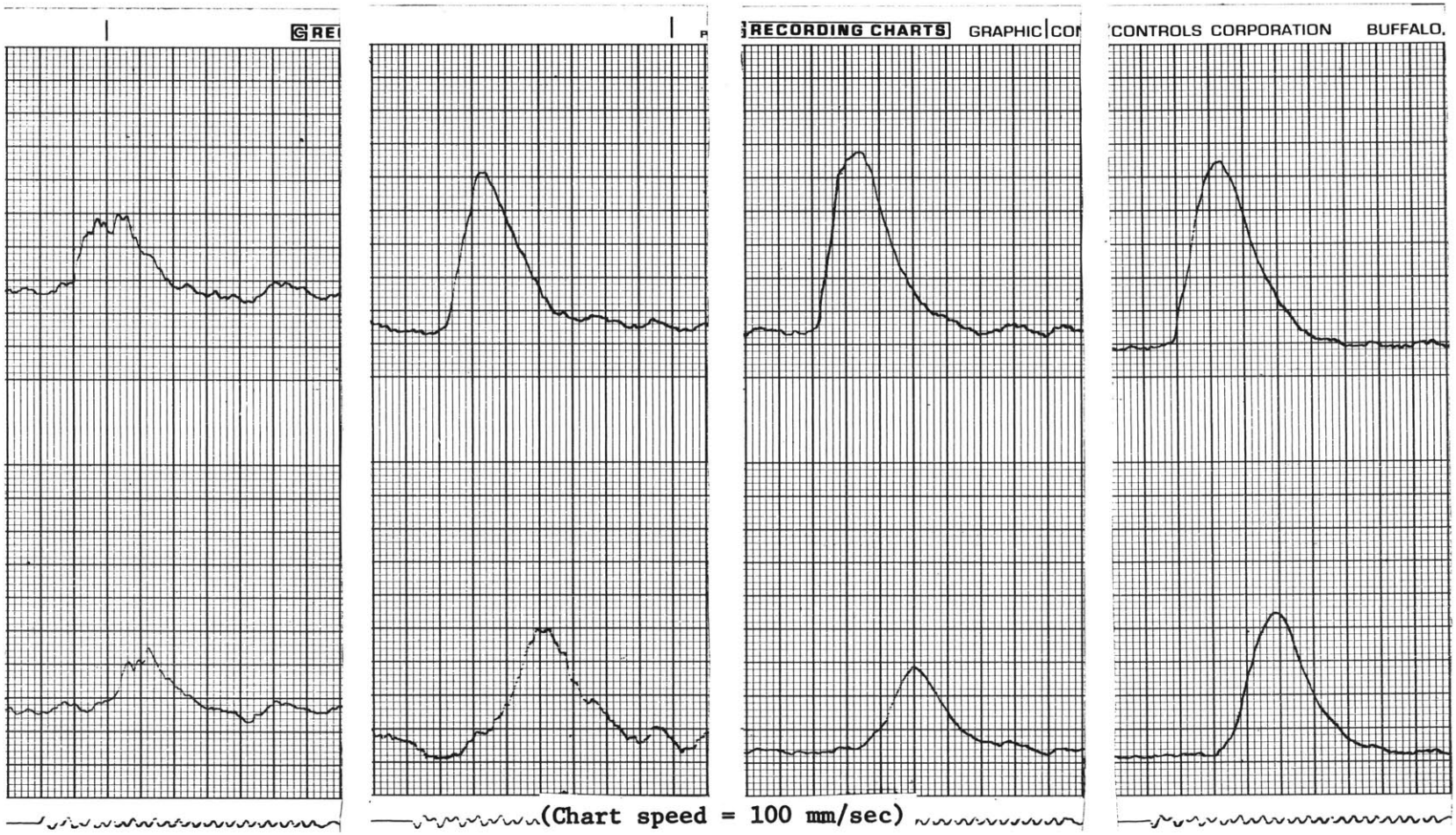

(a) $\frac{Y}{H} = -0.1$

(b) $\frac{Y}{H} = -0.2$

(c) $\frac{Y}{H} = -0.3$

(d) $\frac{Y}{H} = -0.6$

H = thickness of porous foam boundary = 0.1 ft.

Fig. 2-23 Samples of recorded signals at different positions in the boundary $\mathbb{R} = 4 \times 10^5$

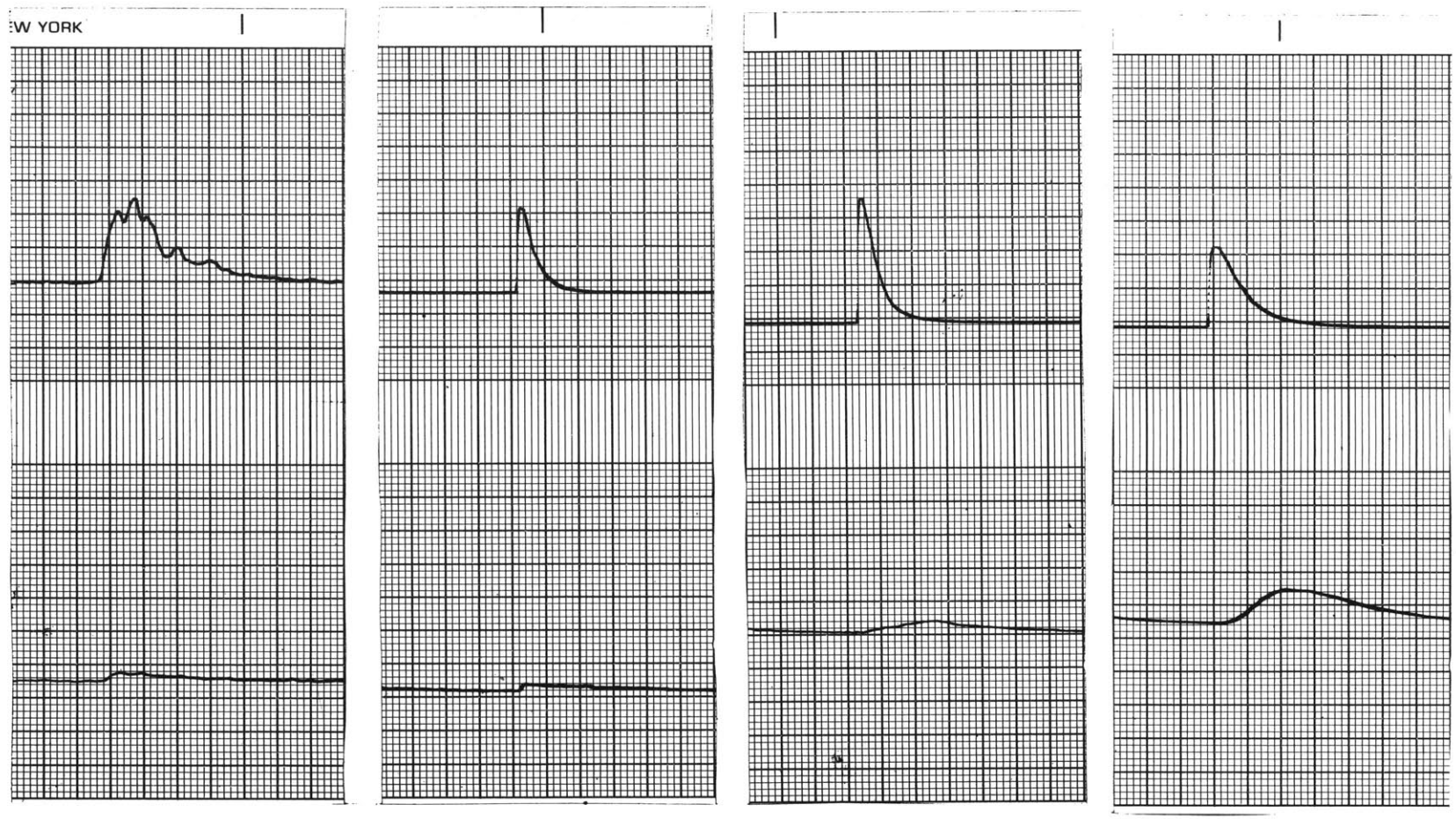

H = thickness of porous foam boundary = 0.1 ft.

Fig. 2-24 Samples of recorded signals at different positions in the porous boundary $\mathbb{R} = 1 \times 10^5$

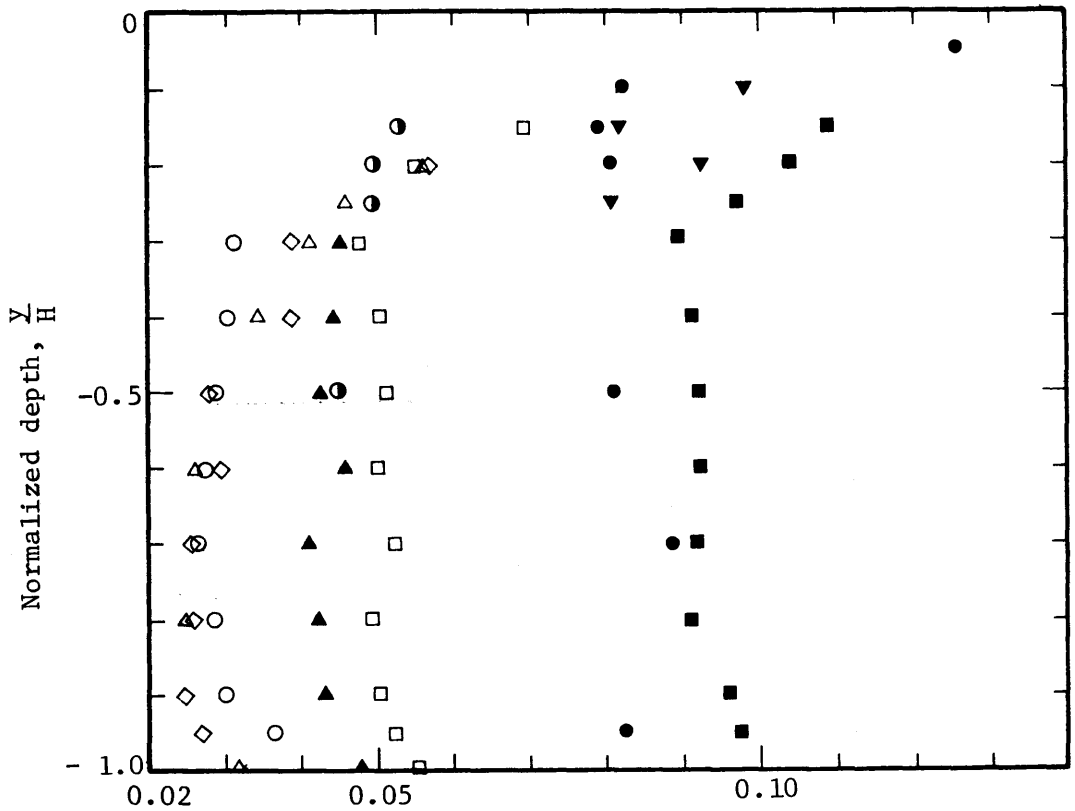

● ▼ ■	4 D 29-1 4 D 29-2 4 D 7-1	$\mathbb{R} = 4 \times 10^5$	$u_* = 7.824$ ft/sec
◑ □ ▲	2 D 29-1 2 D 6-1 2 N 24-1	$\mathbb{R} = 2 \times 10^5$	$u_* = 3.588$ ft/sec
△ ◇ ○	1 D 29-1 1 D 29-2 1 D 18-1	$\mathbb{R} = 1 \times 10^5$	$u_* = 1.596$ ft/sec

H = Porous foam thickness = 0.1'

Fig. 2-25 Seepage velocities in the boundary of a porous pipe determined from helium tracer

since it indicated that the shearing action took place over the entire depth of the boundary. To verify this, different approaches for the data analysis were tried for the measurements in the vicinity of the interface boundary. These approaches are presented in the following sections.

2.6 Tracer Detection in a Turbulent Flow Field

The difficulty of interpreting the data obtained in the vicinity of the interface boundary has already been pointed out. The difficulty arises from the turbulent fluctuations of velocity present in the porous pipe. The fluctuations, considered as noise in this case, make the location of the peak concentration and the travel time between the probes difficult to evaluate. In some cases, the change in voltage due to the helium is on the same order of magnitude as that due to the noise.

Communications engineers have been faced with the same type of detection problem. Through correlation theory and techniques they have developed analytical tools for detecting periodic signals in noise. Lee (1960) presents a thorough development of the theory and technique and only a rudimentary discussion of the method will be given here as it pertains to the determination of the travel time of the peak concentration between the probes.

The crosscorrelation function of two periodic signals $f_1(t)$ and $f_2(t)$ having the same fundamental period, T, is defined as

$$R_{12}(\tau) = \frac{1}{T} \int_{-T/2}^{T/2} f_1(t)\, f_2(t - \tau)\, d\tau \qquad (2\text{-}17)$$

To describe the crosscorrelation function in terms of Fourier coefficients the periodic signals are expanded as:

$$f_1(t) = \frac{a_{10}}{2} + \sum_{n=1}^{\infty} (a_{1n} \cos n\omega_1 t + b_{1n} \sin n\omega_1 t) \qquad (2\text{-}18)$$

$$f_2(t) = \frac{a_{20}}{2} + \sum_{n=1}^{\infty} (a_{2n} \cos n\omega_1 t + b_{2n} \sin n\omega_1 t) \qquad (2\text{-}19)$$

$$a_n = \frac{2}{T} \int_{-T/2}^{T/2} f(t) \cos \frac{n\pi t}{T}\, dt \qquad (2\text{-}20)$$

$$b_n = \frac{2}{T} \int_{-T/2}^{T/2} f(t) \sin \frac{n\pi t}{T}\, dt \qquad (2\text{-}21)$$

The crosscorrelation upon appropriate substitutions and reductions is given by Lee in the form

$$R_{12}(\tau) = \frac{a_{10}a_{20}}{4} + \frac{1}{2} \sum_{n=1}^{\infty} c_{1n}\, c_{2n} \cos (n\omega_1\tau + \theta_{2n} - \theta_{1n}) \qquad (2\text{-}22)$$

where $c_n = \sqrt{a_n^2 + b_n^2}$ (2-23)

$$\theta_n = \tan^{-1}\left(-\frac{b_n}{a_n}\right) \qquad (2\text{-}24)$$

$$\omega_1 = \frac{2\pi}{T} \qquad (2\text{-}25)$$

The discrete form is shown here only because it is easier to see that the crosscorrelation retains the phase differences of the harmonics which are present in both signals. This phase difference is a constant for a given fundamental period, T. The crosscorrelation function has a maximum or minimum whenever

$$\tau = \frac{\theta_{1n} - \theta_{2n}}{n\omega_1} \qquad n = 1, 2, 3 \ldots. \tag{2-26}$$

Relating the crosscorrelation concept to the periodic signals caused by the helium tracer passing the hot wire probes, it will become apparent that one value of the time displacement, τ, given in equation (2-26) is the time of travel of the peak concentration. This is visualized more easily by considering the following simple example.

Assume that two periodic signals shown in Fig. 2-26(a) represent the signals from the hot wire as the helium tracer passes and that the time of travel of the peak concentration between the probes is three units of time. Basically, taking the crosscorrelation of two signals involves three operations, a time shift of one signal relative to the other, multiplication of the ordinates of the two signals, and integration or averaging of the cross products. Fig. 2-26(b) shows one signal being shifted in time with respect to the other. Performing these operations continuously gives the crosscorrelation function, $R_{12}(\tau)$, for the two signals which is shown in Fig. 2-26(c). A maximum in the correlation function occurs at a value of time delay, τ, equal to three time units, which corresponds

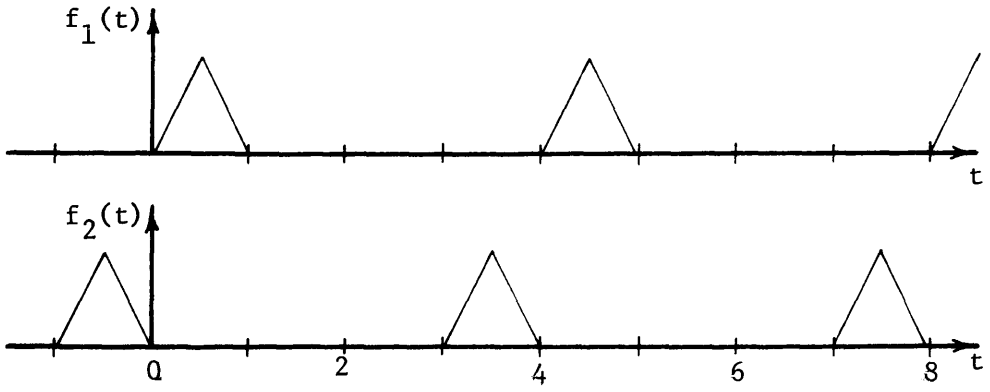

(a) Two periodic signals, $f_1(t)$ and $f_2(t)$, before crosscorrelation

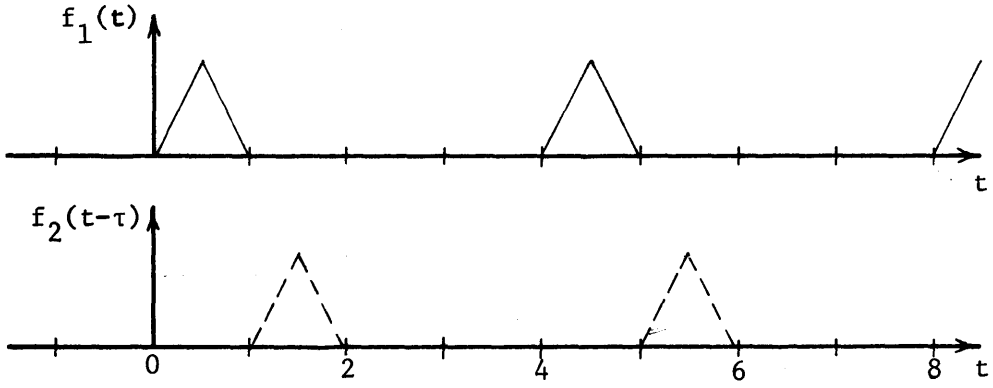

(b) Displacing one signal with respect to the other in time

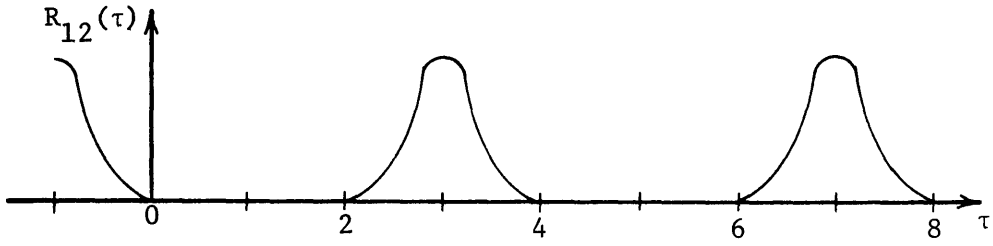

(c) Crosscorrelation function of signals in (a)

Fig. 2-26 Crosscorrelation of two periodic signals

to the travel time of the peak concentration.

Tests were performed using a train of periodic helium pulses. The period of the pulses was varied, and generally two different periods were used at each traverse location. The output signals of the shielded probes were recorded on the FM tape recorder. Cross-correlations of the signals were performed using a correlation function computer, Princeton Applied Research Corporation PAR model 101. The instruction manual provided by Princeton Applied Research Corp. (1967) gives the characteristics of the computer of which the following is a cursory explanation.

The computer utilizes both analog and digital techniques to solve the integrals required for the crosscorrelation function. This is accomplished at 100 incremental subdivisions of the time delay, τ. Time delays from 100 microseconds to 10 seconds in a 1,2,5 sequence can be selected. The useful frequency range specified by the manufacturer is DC to approximately 250 kHz.

To provide an "infinite" length of signal for the correlator to sample, the recorded signals to be analysed were re-recorded on another Precision Instruments FM tape recorder model 6208 which had provisions for a tape loop. The signal was then input from the loop to the correlation function computer. Crosscorrelation and autocorrelation of the two anemometer signals were performed. Plotting of the correlations functions was accomplished with an X - Y recorder, Mosely model 2D2. Typical correlations for two different positions in the porous medium boundary are shown in Figs. 2-27 and 2-28.

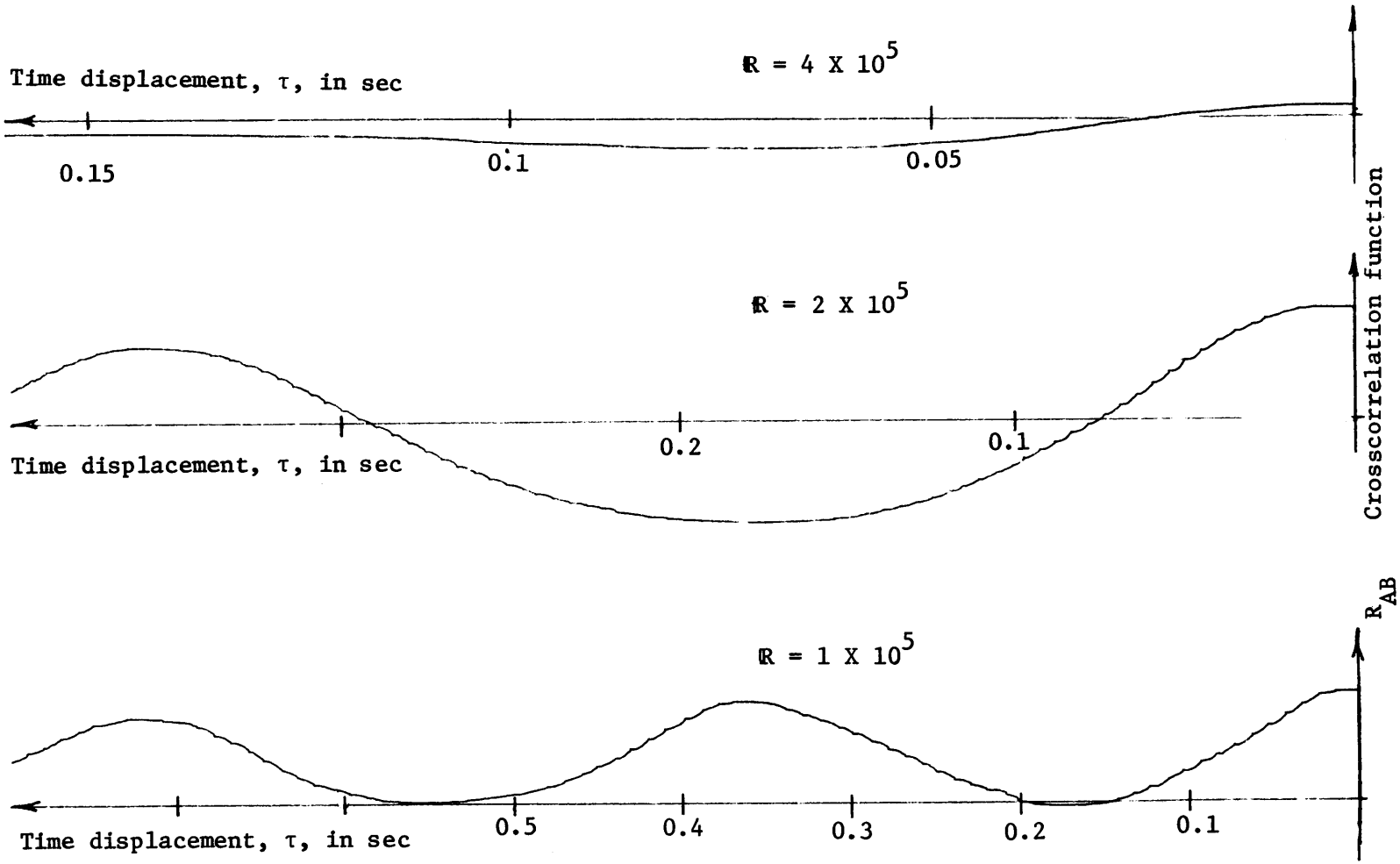

$\frac{y}{H} = -0.1$

(Note: positive time is to the left)

Fig. 2-27 Crosscorrelation functions for anemometers located near surface of porous boundary

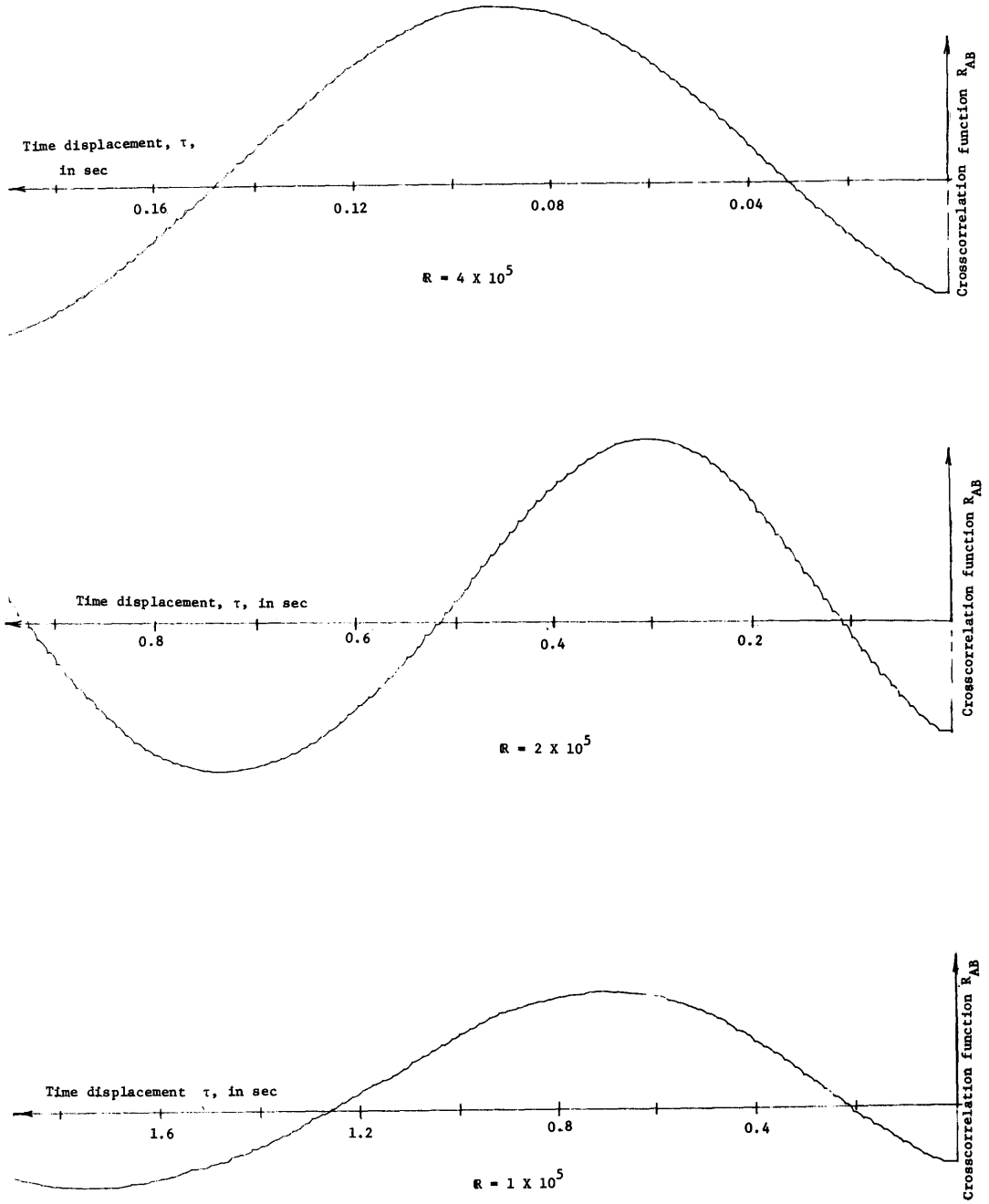

Distance between probes = 0.0583 ft

(Note: positive time is to the left)

$$\frac{Y}{H} = -0.5$$

Fig. 2-28 Crosscorrelation functions for anemometers located at mid-depth of porous boundary

Even though crosscorrelation of the signals eliminates the noise, interpretation of the travel time is still difficult. This is because the travel time is still a random variable. It varies slightly from pulse to pulse due to the turbulent fluctuations in the velocity, the path which the helium follows through the porous matrix, and slight irregularities in the response time of the valve. These effects plus the fact that correlation is an averaging process tend to make the peak in the crosscorrelation curve relatively flat and difficult to interpret as is shown in Fig. 2-27. If the time of travel is relatively long in comparison to the time over which the peak occurs as is the case for Fig. 2-28, good results can be achieved with crosscorrelation. Seepage velocities calculated from the cross-correlation functions are shown in Fig. 2-29.

In the vicinity of the interface boundary, the velocities are the highest, turbulence intensities are nearly maximum, and these effects all combine to make determination of the travel time difficult even with crosscorrelation. It was in this region good results were desired. Unfortunately, crosscorrelation of the signals met with only limited success because of the "flat" peaks in the crosscorrelation function which allowed a wide interpretation of the travel time.

Over the rest of the foam boundary, from about Y/H = -0.3 to the impermeable wall, crosscorrelation worked well. The travel times are a better representation of the mean travel time since they are determined from a minimum of 40 pulses. The results found by correlation verify those already found using the visual determination of the peak

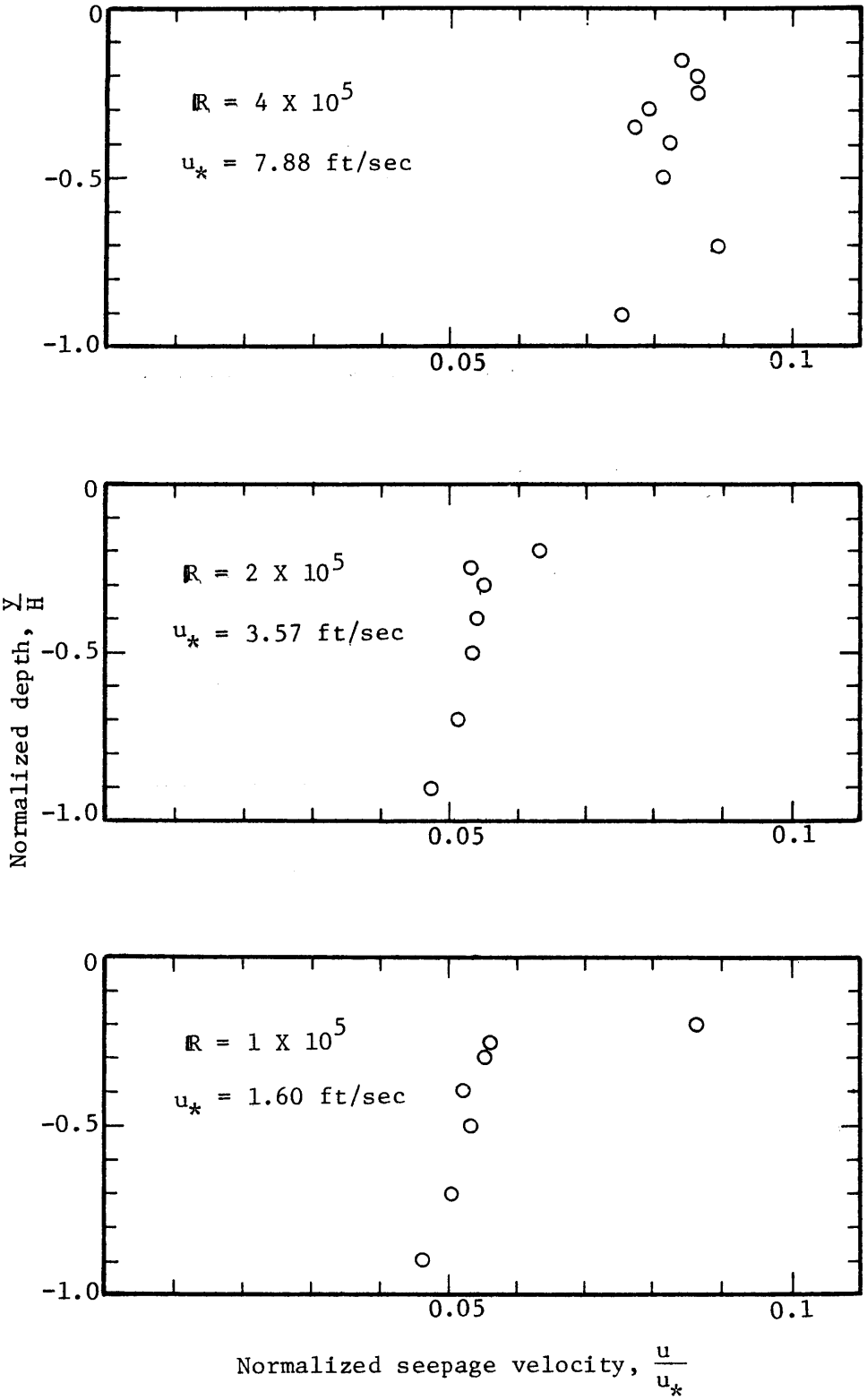

Fig. 2-29 Seepage velocities determined from crosscorrelation functions

concentrations for the two higher Reynolds number flows, thus, reinforcing the evidence that the shear effects from the core flow penetrate to a relatively shallow depth. At the lower Reynolds number, the velocities determined from crosscorrelation functions are higher than those determined from the visual determination of travel times. This apparent discrepancy may have been the result of the jet issuing from the injector and the injector probe locations. For the visual runs the probes were generally spaced at distances greater than 1 in. and the distance from the first probe to the injector was initially 1.44 in. and later 0.70 in. For the correlation runs, the distance between the shielded probes was reduced to 0.70 in. and the distance between the injector and the first probe was 0.66 in. At the low Reynolds number, actual seepage velocities for the visual determinations were on the order of 0.05 ft/sec and for the correlation determinations on the order of 0.08 ft/sec. The velocity of the jet entering the porous foam is not known, but it apparently produces some effect for close spacing of the injector and shielded probes.

2.7 Shielded Probes Used as Anemometers

The shielded probes when used directly as anemometer indicated velocities that correlated well with double the seepage velocity. The correlation shown in Fig. 2-20 is limited to velocities greater than about 1.5 to 2.0 ft/sec because of the characteristics of the shielded probes.

A typical calibration for one of the shielded hot wire probes is given in Fig. 2-30. The data points deviate from a straight line, at a value of F(V) of approximately 1.4 which corresponds roughly to an

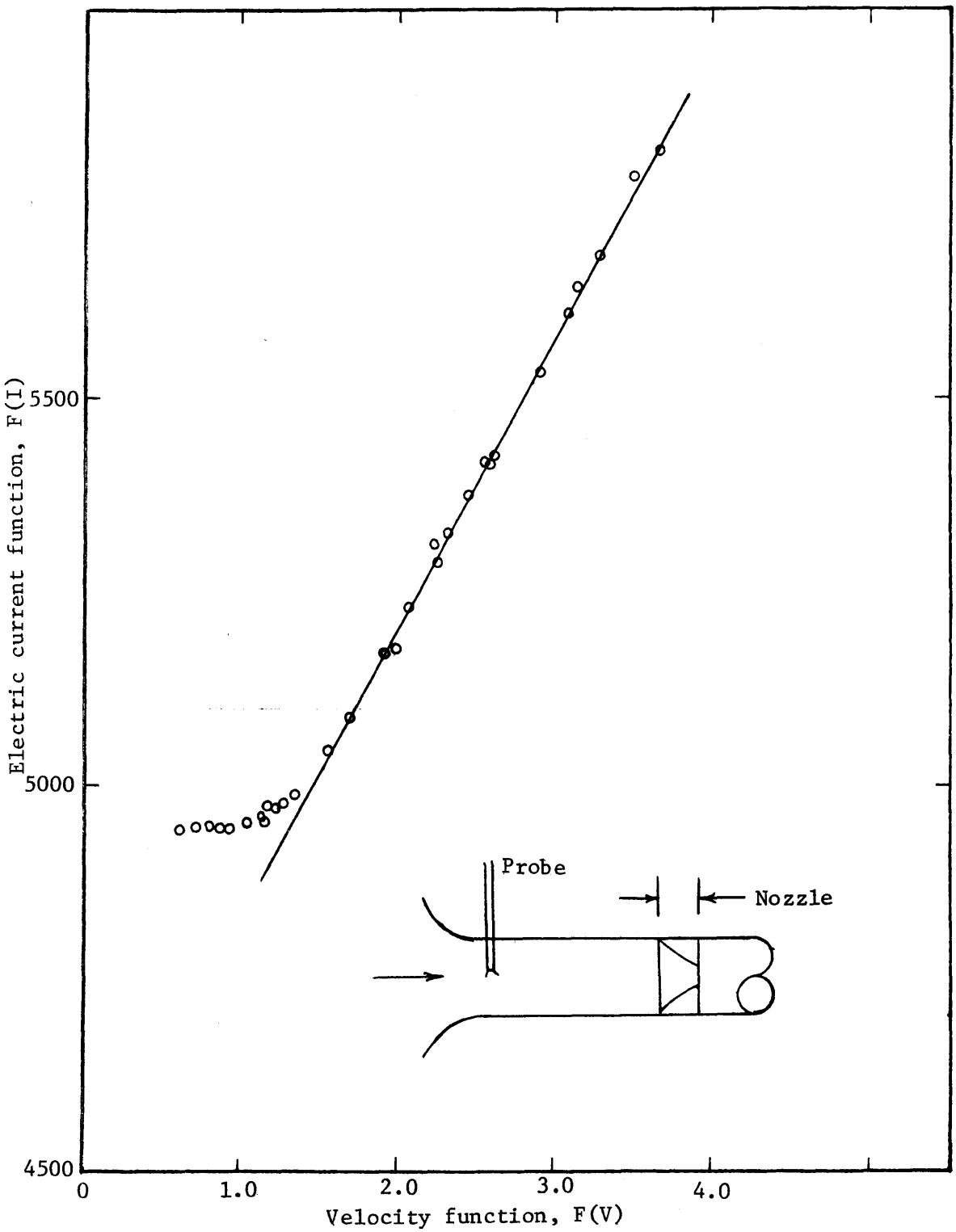

Fig. 2-30 Shielded hot wire anemometer probe calibration curve

air speed of about 1.5 ft/sec. Collis and Williams (1959) observed a similar phenomenon due to the interaction of free and forced convection. They gave a rough criterion for the effects of buoyancy (free convection) for wires with large aspect ratios (length of wire, ℓ, divided by its diameter, d) in terms of the wire Reynolds number and the Grashof number. They cautioned that for sufficiently small aspect ratios three-dimensional heat transfer could modify the heat flux at higher Reynolds numbers than that given by their criterion. The wires they used has aspect ratios greater than 2000 and the deviations due to free convection occurred at Reynolds numbers of about 0.03. The shielded probes used in this study have aspect ratios on the order of 125 and the deviation observed in Fig. 2-30 occurs at a Reynolds number of about 0.16, where the Reynolds number was determined in the same manner as Collis and Williams. The effect of the shield on the heat transfer is not known, but probably also adds to the effects causing the deviations.

Mean velocities measured with the shielded probe anemometer in and near the porous foam boundary are shown in Fig. 2-31. All seepage velocities in the boundary were interpreted as being one half the velocity indicated by the anemometer. The point at the surface, Y/H = 0.0, was included in this interpretation even though one half of the shield opening was exposed to the core flow and, therefore, the interpretation may be incorrect. Velocities in the core are actual velocities determined with the anemometers. Velocities less than 1.5 ft/sec are included to aid in visualizing the shear zone even though they are somewhat ambiguous as to their actual magnitude. Also plotted

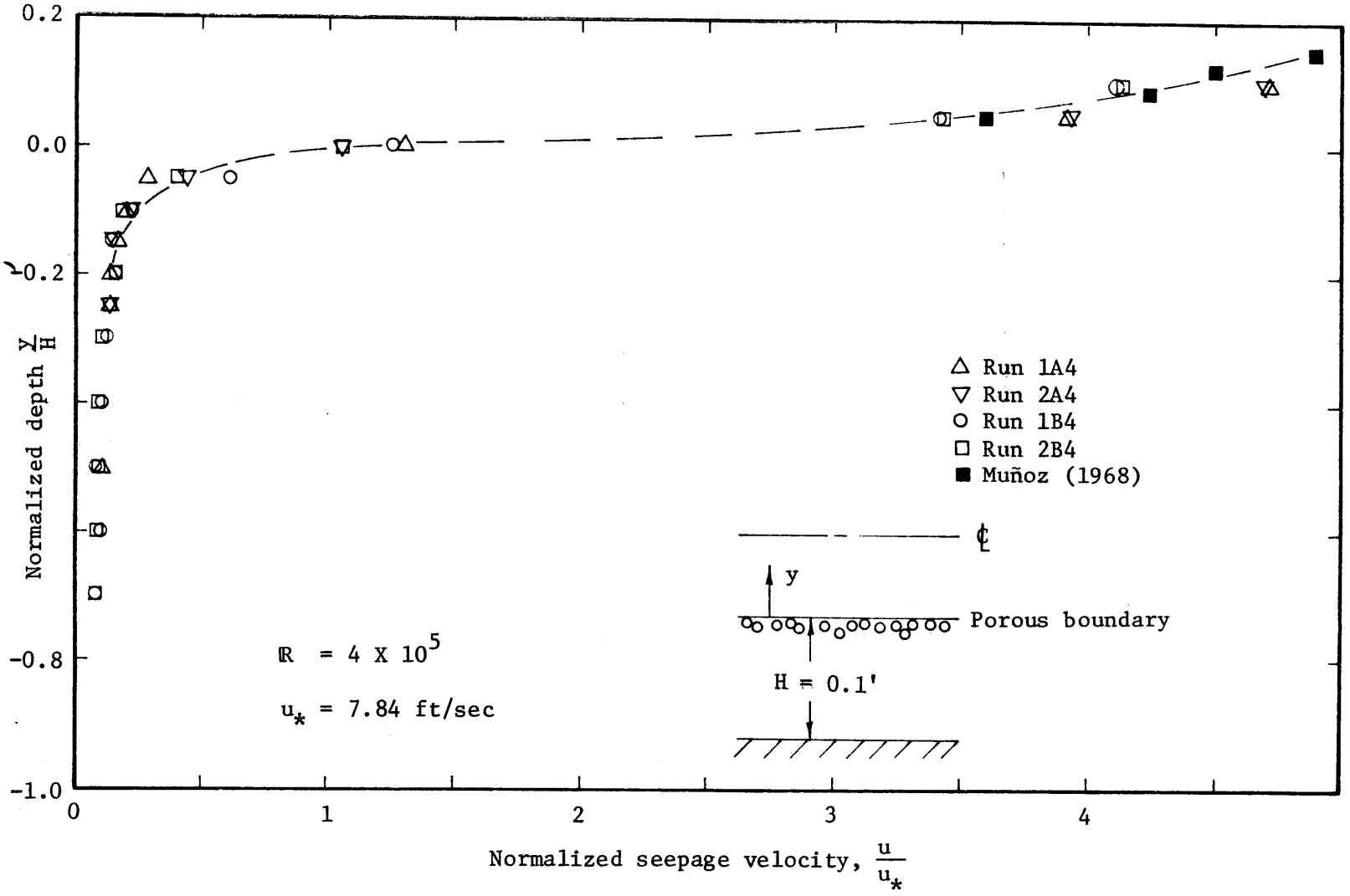

Fig. 2-31a Velocities near surface of porous boundary measured with shielded hot wire anemometer probe, $R = 4 \times 10^5$

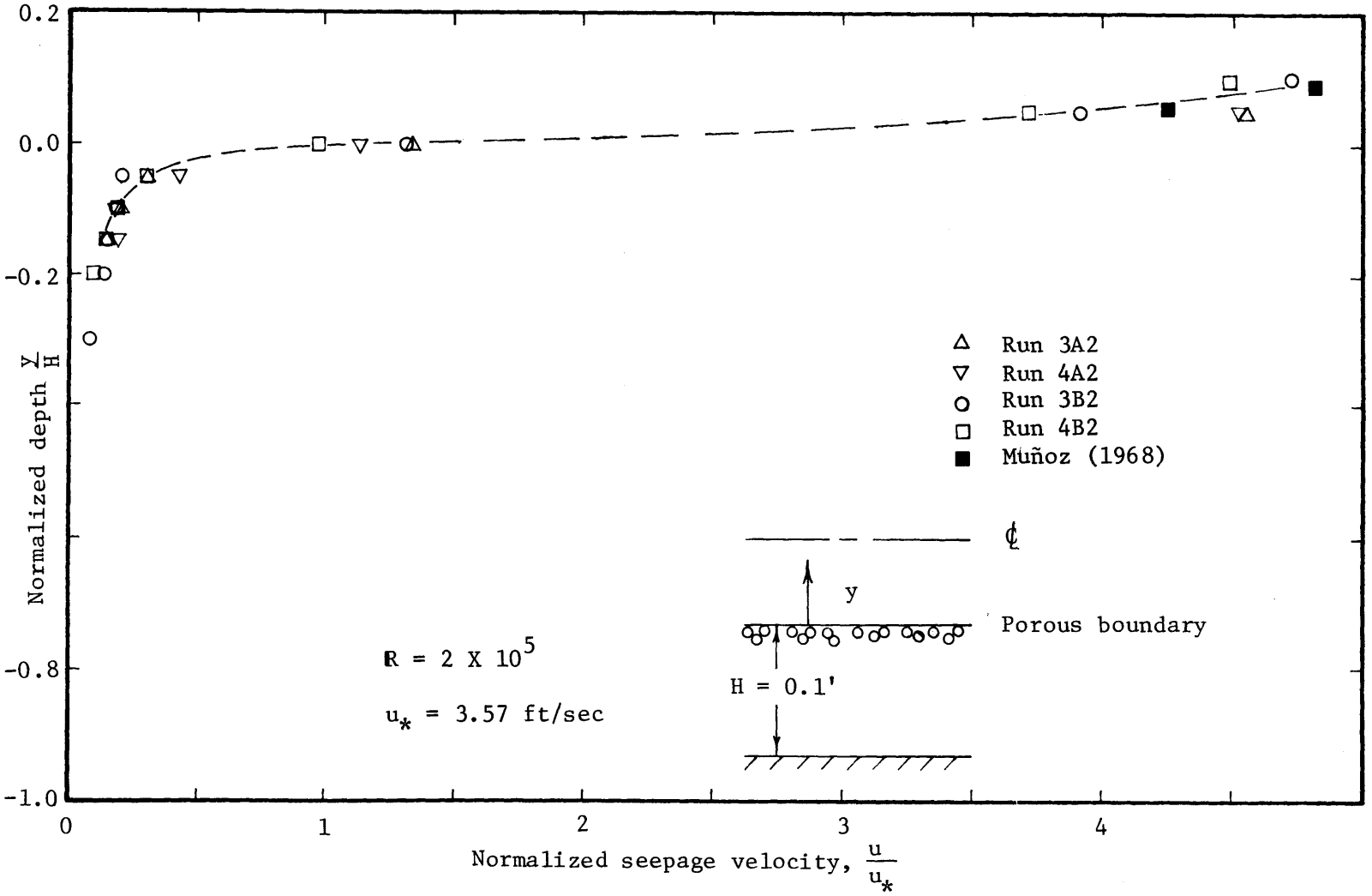

Fig. 2-31b Velocities near surface of porous boundary measured with shielded hot wire anemometer probe, $R = 2 \times 10^5$

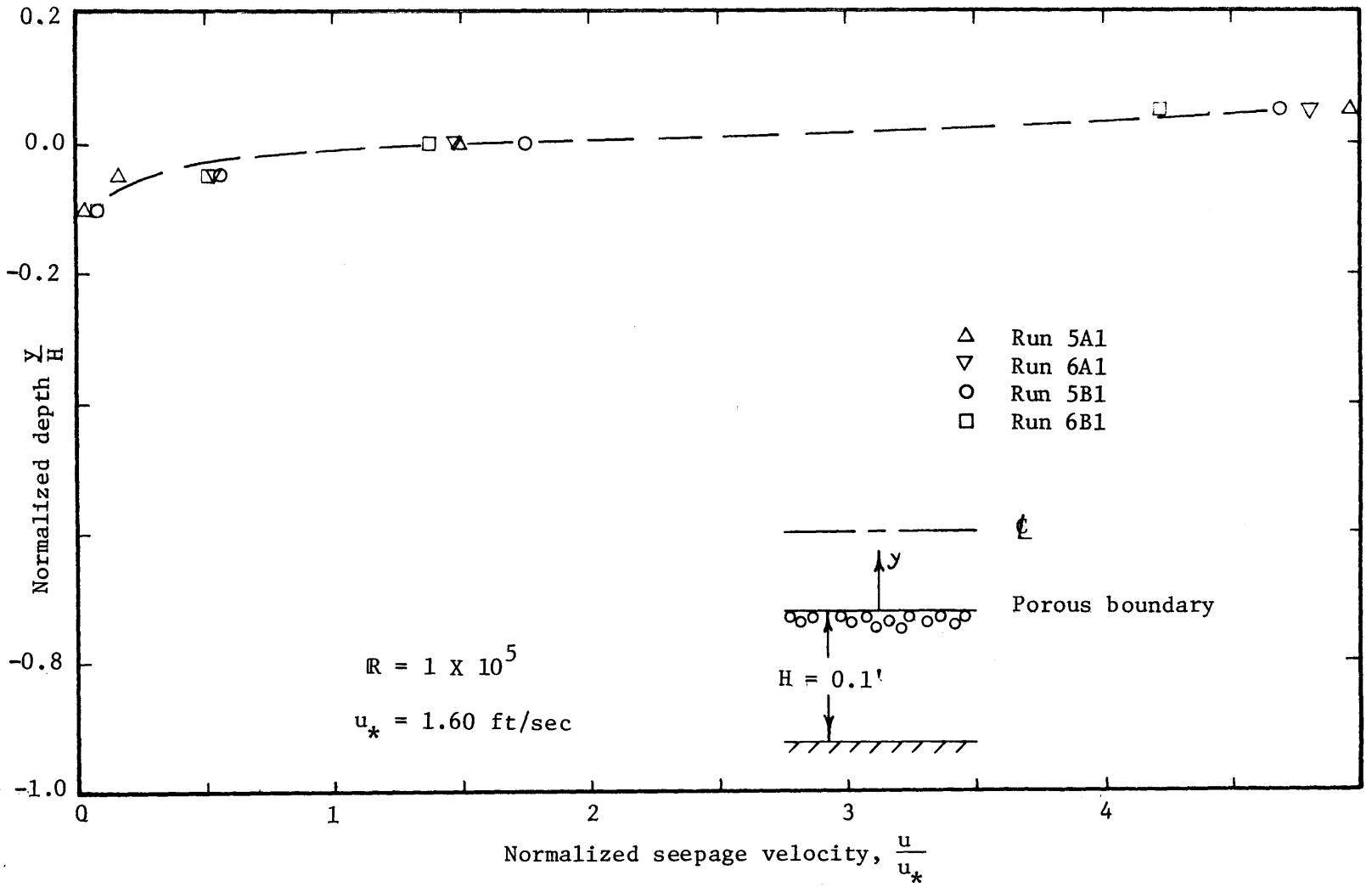

Fig. 2-31c Velocities near surface of porous boundary measured with shielded hot wire anemometer probe, $\mathbb{R} = 1 \times 10^5$

on Fig. 2-31 are velocities measured by Muñoz in the core near the interface. The dashed curves in Fig. 2-31 were fitted by eye and are drawn only in the range of validity of the shielded probe anemometers.

Longitudinal intensities of turbulence measured with the shielded probes are shown in Fig. 2-32 along with those measured by Muñoz (1968) in the core flow near the porous boundary.

Both the mean velocity profiles and the turbulent intensity profiles indicate the shearing effect penetrates only to a depth of $Y/H \simeq -0.25$ or -0.30. Beyond this depth, the shearing effect is negligible and the flow is governed by the pressure gradient in the pipe. These results are in agreement with the penetration depth and uniform velocity distribution indicated by the tracer technique.

2.8 In Situ Intrinsic Permeability

The specific discharge, q, within the porous medium boundary is related directly to the intrinsic permeability of the medium. When there is no shear, Eq. (3-17) describing the velocity distribution in the boundary is nearly that presented by Ward (1964).

$$-\frac{1}{\rho}\frac{dp}{dx} = \frac{\nu q}{k} + \frac{1}{C\sqrt{k}}\,q^2 \qquad (2\text{-}27)$$

The difference is that Eq. (2-27) uses the specific discharge and Eq. (3-17) uses the seepage velocity.

Tests were performed in the porous pipe to determine the values of C and k using the above equation. The pressure drop along the pipe was measured using a U-tube manometer. The specific discharge, q, within the porous medium boundary was determined using the tracer

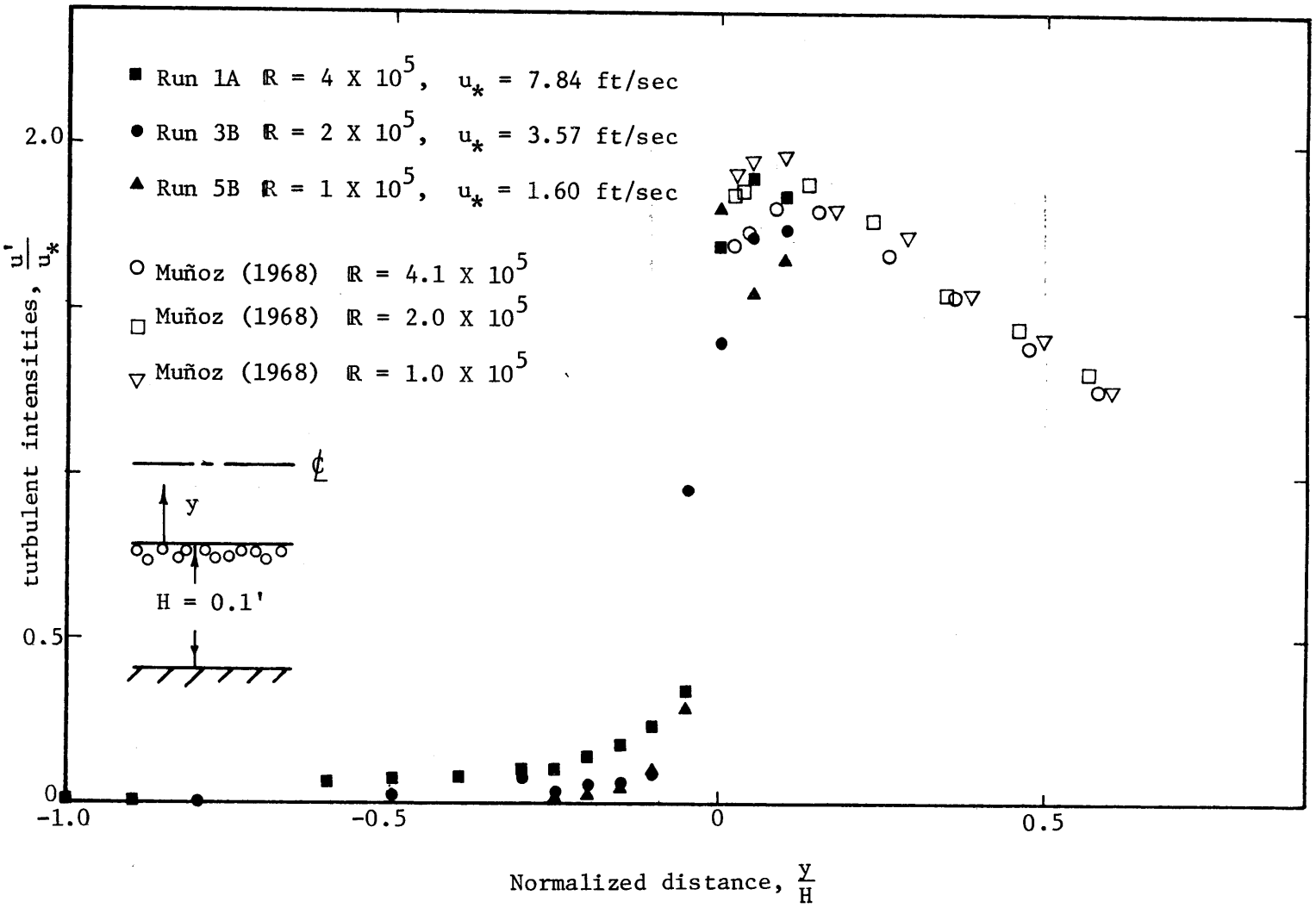

Fig. 2-32 Longitudinal intensities of turbulence relative to the shear velocity near surface of the porous boundary

technique with manually controlled pulses. The probes were located in a plane 0.72 in. from the interface boundary at a distance of 0.70 in. apart.

Equation (2-27) was rearranged to provide a relation of the form

$$Y = mX + b \tag{2-28}$$

where

$$Y = \frac{1}{\rho q^2} \frac{dp}{dx} \tag{2-29}$$

$$X = \frac{1}{q} \tag{2-30}$$

$$m = \frac{\nu}{k} \tag{2-31}$$

$$b = \frac{1}{c\sqrt{k}} \tag{2-32}$$

In this form, the permeability and the constant, c, can be determined directly from the slope and intercept of the linear equation.

Fig. 2-33 shows data points plotted for a range of pipe Reynolds numbers from about $\mathbb{R} = 1.7 \times 10^5$ to $\mathbb{R} = 4 \times 10^5$. The line, labeled $Y = 52.1 + 390.9X$, is the best fitting straight line found by the method of least squares. The permeability, k, and the constant, c, determined from this linear equation are:

$k = 0.409 \times 10^{-6}$ sq ft

$c = 30.0$

These values of k and c were used to develop the theoretical curves of velocity distribution in the porous boundary presented in Chapter 3.

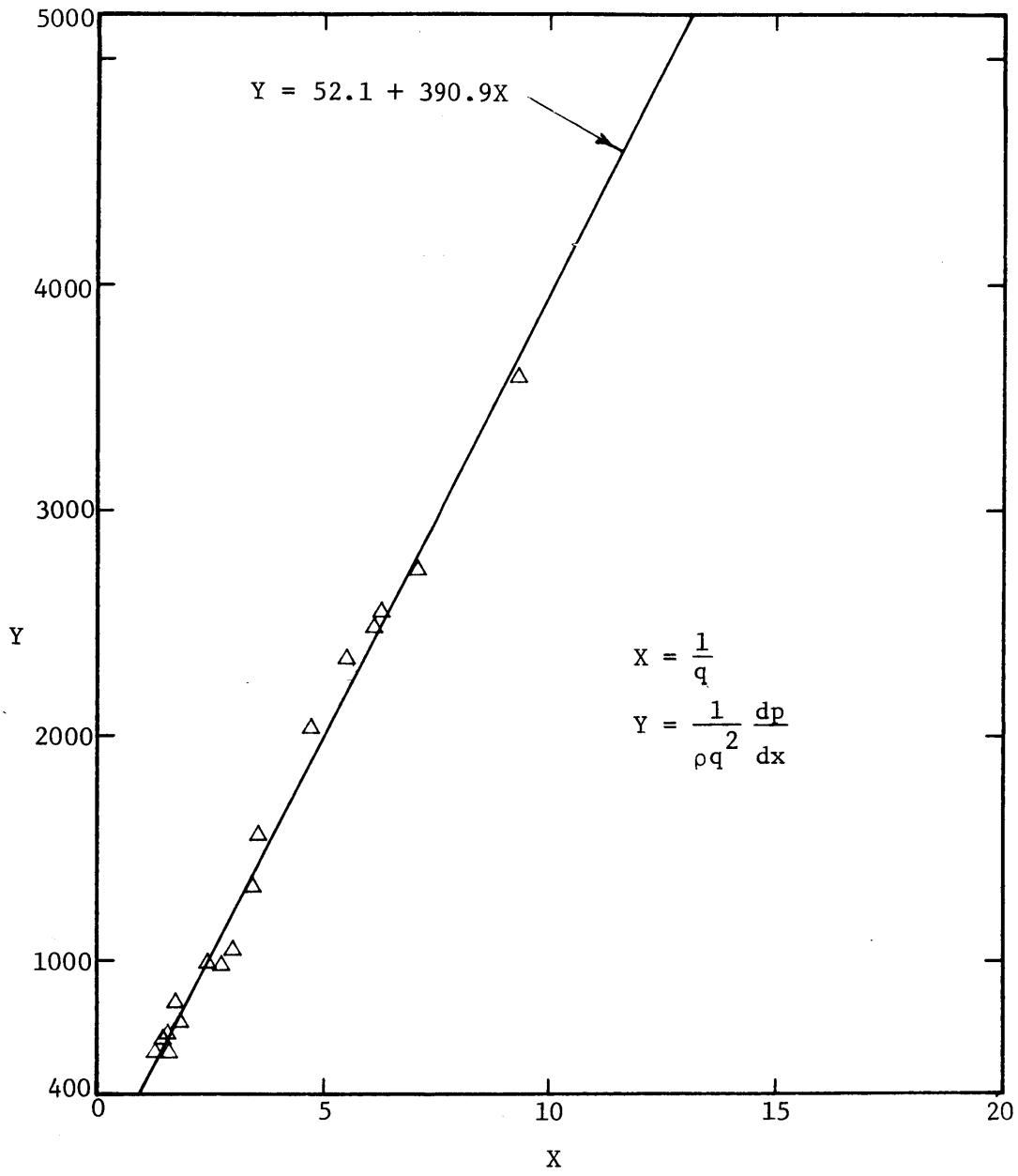

Fig. 2-33 Intrinsic permeability determination

2.9 Longitudinal Dispersion Coefficient

The concentration distribution of the helium tracer injected instantaneously into an infinite flow field will be developed in Chapter 4 and the dimensional form of Eq. (4-56) can be written as

$$c(x,y,z,t) = \left(\frac{M/\rho}{8\pi^{3/2}\sqrt{E_{10}}\,E_{20}\,t^{3/2}}\right) \exp\left(-\frac{1}{4t}\left[\frac{(x-ut)^2}{E_{10}} + \frac{y^2+z^2}{E_{20}}\right]\right)$$

$$\left(1 - \frac{3}{4}\frac{5y}{L}\frac{[x-ut]\,ysU_o}{4LE_{10}} + \frac{ys}{8Lt}\left\{\frac{(x-ut)^2}{E_{10}} + \frac{y^2+z^2}{E_{20}}\right\}\right) \quad (2\text{-}33)$$

where E_{10} and E_{20} are the longitudinal and lateral dispersion coefficients on the x-axis.

Letting

$$c_o = \frac{M/\rho}{8\pi^{3/2}\sqrt{E_{10}}\,E_{20}} \quad (2\text{-}34)$$

and considering the case along the x-axis, the concentration distribution, which is now only a function of x and t, can be written as

$$c(x,t) = \frac{c_o}{t^{3/2}} \exp\left\{-\frac{1}{4t}\left(\frac{(x-ut)^2}{E_{10}}\right)\right\} \quad (2\text{-}35)$$

From this relationship, the dispersion coefficient, E_{10}, can be determined if either the concentration distribution is known for all values of x at a given time or for all values of time at a given distance, x, from the source of the injection.

The velocity distribution in the porous foam boundary has been shown to be relatively uniform at distances from the interface boundary of Y/H = - 0.3 to the pipe wall. Therefore, over this region, the variation in the velocity in the angular direction should be negligible and the flow field can be represented in a Cartesian coordinate system, thus making Eq. (2-35) applicable.

The helium tracer system was set up initially to determine the travel time between the two hot wire probes. The timing marker on the strip chart recorder was energized every time the switch was tripped to open the solenoid valve. The time indicated between this mark and the hot wire responses recorded on the strip chart is not the exact time from the instant the helium is released. This is due to the time required for the helium to travel from the valve through approximately 3 in. of 1/8 in. pipe and about 4 in. of the hypodermic needle shaft to the point of injection. The purging of the air from the needle and the subsequent mixing of air and helium in this piping section was thought to cause the elongated tail observed on the strip chart records of the concentration curves.

Since there are two probes, the time of travel from the injection point to the probes can be estimated in the following manner. If the dispersion coefficient is assumed to be small, the travel time of the peak concentration is the same as the mean velocity. When the maximum concentration occurs, $x = ut$ and the value of the exponential term is 1. Call t_{p1} and t_{p2} the times at which the maximum concentrations, c_{p1}, and c_{p2}, are observed at probe 1 and 2, respectively. Then

$$t_{p2} = t_{p1} + \Delta t \tag{2-36}$$

where Δt is the travel time of the peak between the two probes.

Using equation (2-35)

$$\frac{c_{p1}}{c_o} = \frac{1}{t_{p1}^{3/2}} \tag{2-37}$$

$$\frac{c_{p2}}{c_o} = \frac{1}{t_{p1}^{3/2}} \tag{2-38}$$

Dividing (2-37) by (2-38) and substituting equation (2-36) for t_{p2} gives

$$\frac{c_{p1}}{c_{p2}} = \frac{(t_{p1} + \Delta t)^{3/2}}{t_{p1}^{3/2}} \tag{2-39}$$

The voltage difference of the anemometer output between that observed at the maximum concentration and that when no tracer was present was used to calculate c_{p1} and c_{p2}. The travel time, Δt, can be measured directly from the strip chart and thus the time, t_{p1}, can be calculated.

Dividing equation (2-35) by either (2-37) or (2-38) the concentration observed at the probe, c, related to the peak concentration c_p, and time to the peak, t_p, is

$$\frac{c}{c_p} = \frac{t_p^{3/2}}{t^{3/2}} \exp\left\{-\frac{(x - ut)^2}{4E_{10}t}\right\} \tag{2-40}$$

Knowing the distance between the probes, the value of x can be determined from

$$x = u \cdot t_p \tag{2-41}$$

Thus, the longitudinal dispersion coefficient, E_1, can be determined if curves of concentration versus time are known at two points along the x-axis. This is the type of information presented on the strip chart records.

Several methods are available for evaluating E_{10}. The method used here was to find the best fit curve from the time the anemometer first sensed the helium to the time when the peak concentration was observed. The points beyond the peak were disregarded because the injection was not instantaneous and its exact form was not known.

If the form of the injection pulse were known exactly, it could be described by superposition of a number of the instantaneous pulses and the concentration observed at the probes would be the superposition of the solutions of this pulse train. However, since the objective of finding the dispersion coefficient was only to determine its order of magnitude and to see if the assumption used for the dispersion coefficients in Chapter 3 seemed justified, further refinement of its determination did not seem justified. The assumption made was that E_1 was directly proportional to the velocity.

Values of E_1 were determined from the data at the two probes. A curve was fitted through the rising limb of the c vs t curve using different values of E. The value of E_1 was found from a least squares fitting of the data to the rising limb of Eq. (2-35). The values of

E_{10} determined in this manner are given in Fig. 2-34 in terms of the relationship between E_1 and the seepage velocity, u. This relationship can be characterized roughly by the equation.

$$E_{10} = \alpha_1 u_o \tag{2-42}$$

where $\alpha_1 = 0.00167$ ft.

2.10 Discussion of Experimental Techniques and Results

The objective of the experimental work described was to develop a method of making direct measurements of the seepage velocity within a porous foam. Several techniques were used in the course of the experimental phase of the study.

The unshielded anemometer probe when used in a hole punched in the foam gave results that now appear to be biased due to the physical configuration of the hole and probe combination. It is not known exactly what the flow patterns in a shear flow is in the vicinity of the cylindrical hole. However, when the hole was completely open above the probe, there could be considerable interaction between the core flow and the flow within the hole. Adding the plug above the probe should produce this interaction somewhat but still a three dimensional pattern occurs and some complex averaging takes place within the cylindrical disc surrounding the probe. The size of the hole causing the disturbance is probably the most significant factor of all. Its minimum size was that of a disc approximately 1/8 in. high by 1/4 in. diameter. This size was necessary to provide clearance for the hot wire. This method could not be counted on to give an accurate indication of the seepage velocities.

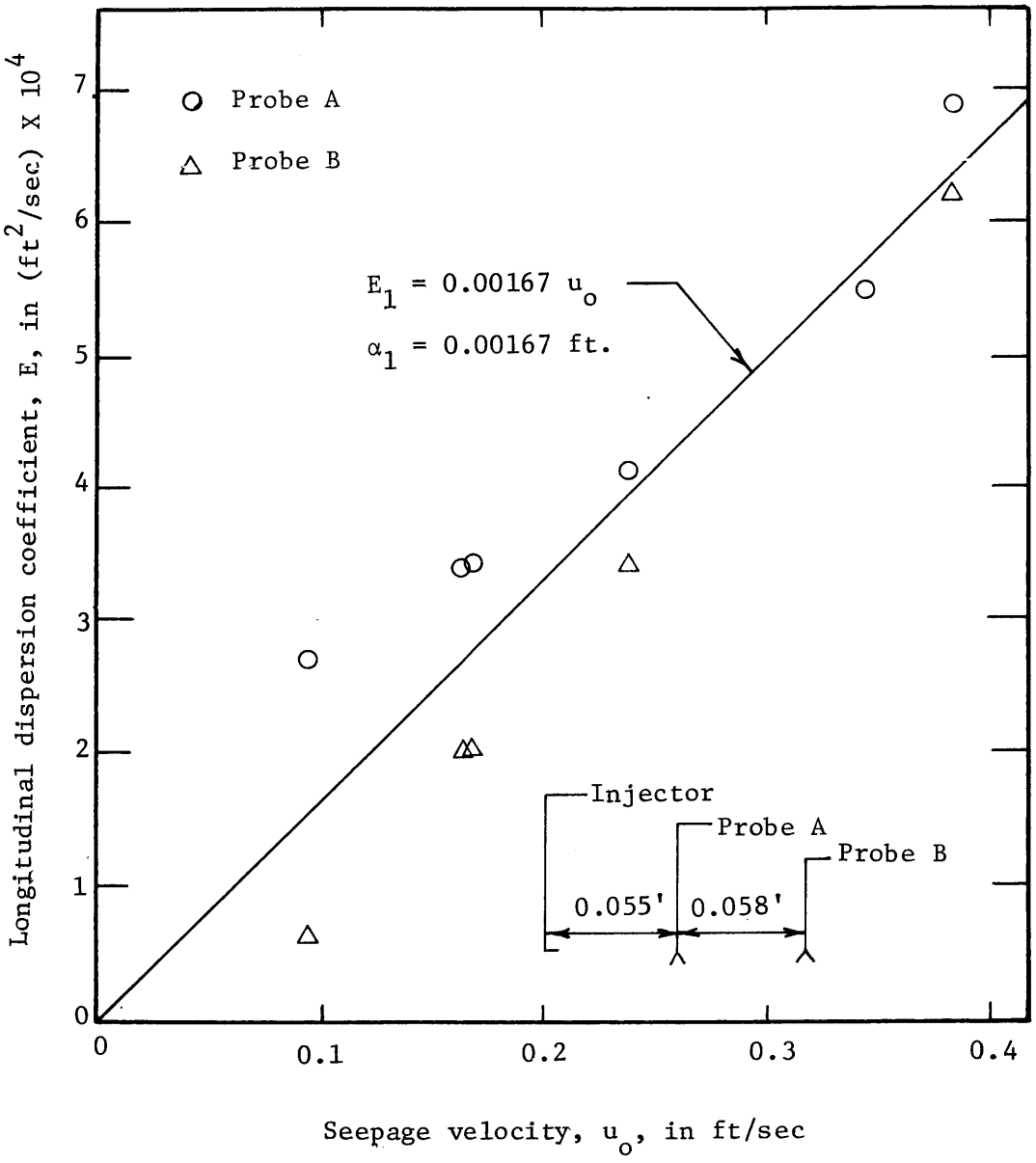

Fig. 2-34 Relationship between the longitudinal dispersion coefficient and the seepage velocity

Attempts at making measurements in the porous foam using the pitot tube were completely unsuccessful. This was primarily due to the difficulty encountered in traversing the pitot tube through the foam and the inadequate resolution of the system at low velocities.

The tracer techniques provided good results in the region where the flow was driven primarily by the pressure gradient as was shown in Figs. 2-25 and 2-29. Near the interface boundary where the turbulent intensities and the shearing effect predominate, the method met with only limited success. In this region it was difficult first of all to observe the helium patch passing both probes, and when it did pass both probes, to be able to distinguish the peaks. The probes were moved closer together in order to observe the patch passing both probes. The reduction in the probe spacing reduced the accuracy in the determination of travel times. Velocities determined in the shear zone were unreliable and erratic at best even with crosscorrelation of the signals.

Crosscorrelation of the signals provided a good method of determining travel times where the travel times were of sufficient duration not be lost in the peak of the crosscorrelation function. Seepage velocities of magnitudes much below what the hot wire anemometer can measure directly were determined using the tracer technique.

Velocities were measured in the shear zone using the shielded probes directly as anemometers. The arguments concerning flow patterns presented against the unshielded probe pertain to the shielded probe only to a limited extent. The shield eliminates effects from the core

flow impinging directly on the hot wire. The area over which the shielded probe samples the velocity is approximately the size of two pores, 0.03 in. by 0.06 in. Therefore, the flow pattern in the vicinity of the opening should approach that predicted by the potential flow solution which indicates a correlation between the velocity sensed by the probe and two times the actual seepage velocity. This correlation was evident in the calibration experiments in the 2 in. diameter plexiglass tubing. Velocities measured with the shielded probe are limited to those greater than about 1.5 ft/sec.

The results of this study showed that velocities over the entire depth of foam can be measured only by using a combination of the techniques. The tracer technique works well in the pressure gradient flow region. The shielded probe anemometer works best in the shearing zone and the velocities determined with it can be interpreted to give the seepage velocities, thus, completing the velocity profile. A composite picture of the velocity distributions at different pipe Reynolds numbers is given in Fig. 2-35. The distributions were determined from the anemometer velocities (Fig. 2-31) and the tracer velocities (Figs. 2-25 and 2-29). The lines representing the velocities were established in the following manner. In the shear zone, the seepage velocities were obtained from the dashed curves of Fig. 2-31. Points in the zone of pressure gradient flow were taken from the helium tracer data. A best fit line was determined by eye in each zone and the two were faired together at the intersection. The lines shown in Fig. 2-35 are the culmination of the experimental phase of the study. They

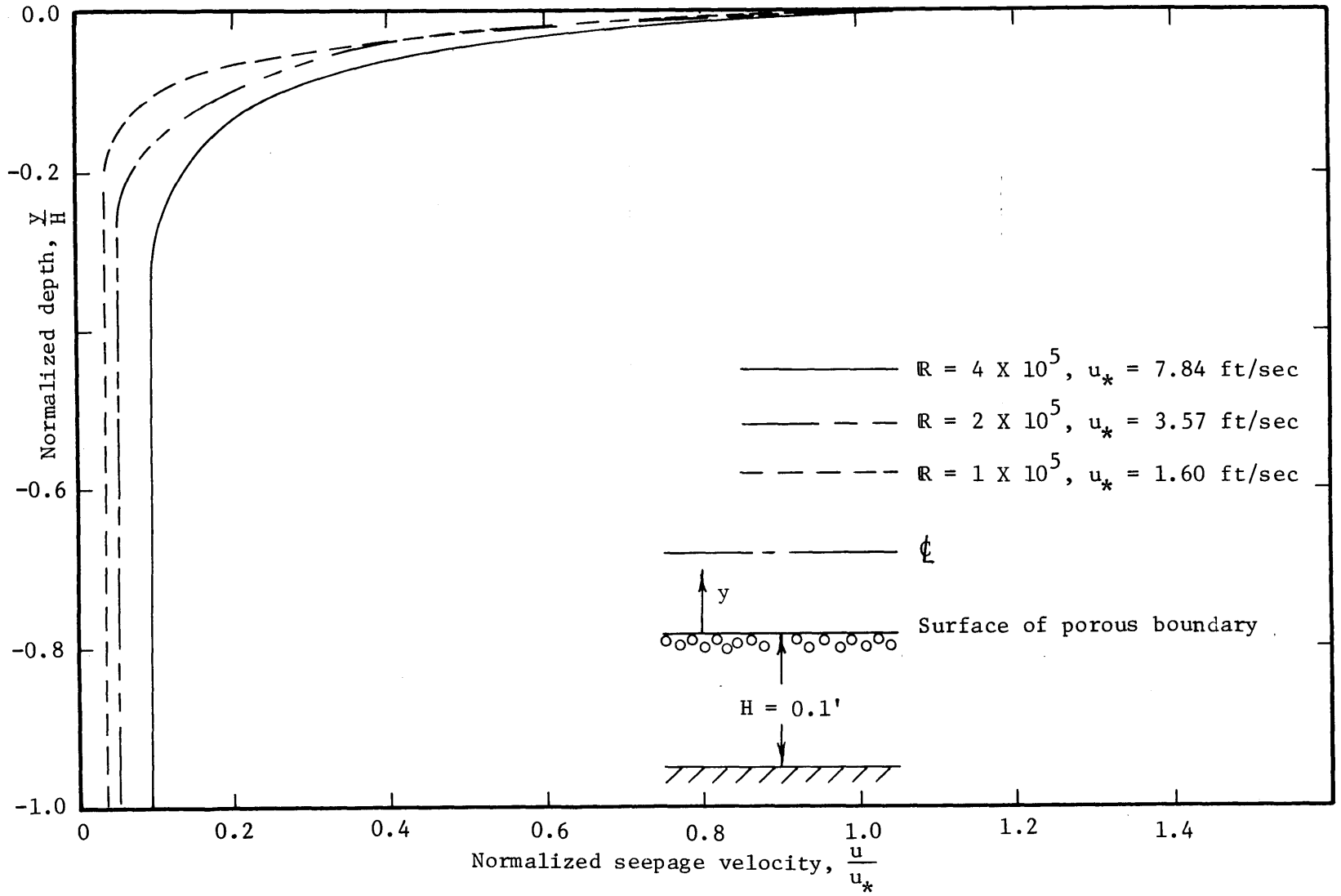

Fig. 2-35 Composite of velocity distributions in a porous boundary exposed to turbulent shear flow

represent what is the best known estimate of the velocity distributions within a porous boundary exposed to turbulent shear flow. The penetration depths indicated in Fig. 2-35 should be used only as a guide since the data in the region are not sufficient to specify the penetration depths exactly.

The longitudinal turbulence intensities were presented in Fig. 2-32. It is uncertain as to their exact meaning. This is partially because the mean velocity is correlated with twice the seepage velocity and what effect this correlation has on the fluctuating component of velocity is unknown. Also, the effect of the shield is unknown. It should be noted that in the core flow, the shielded probe indicates intensities comparable to those measured by Muñoz. They are presented because it is felt, they give at least a relative indication of the penetration depth of the turbulence and thus an indication of the shearing zone in the porous medium.

III. ANALYSIS OF FLOW IN A POROUS BOUNDARY

3.1 Introduction

There are numerous studies which have investigated flow characteristics in flow fields over porous boundaries. However, despite these, there is no information regarding the flow characteristics within the boundary. In some studies, such as those by Eckert, et. al., (1955) and Olsen and Eckert (1966), the boundary only provides a means of applying suction or injection to the system. In other studies, such as those conducted in sand bed channels and porous pipes, it is known that the boundary exerts a considerable effect on the mean flow characteristics in the overriding fluid. This effect usually is attributed to the boundary geometry since the effect due to the flow in the boundary is unknown.

It is possible that there is some interaction between the porous medium flow and the channel or core flow. Each flow tends to modify the other and in turn be modified. But, the mechanism of this interaction is not understood. It is felt that the interaction is related to the fluid turbulence.

The purpose of this chapter is to develop a description of the flow in a porous boundary exposed to an external superposed shear flow. The porous boundary in this study is a lining attached to an impervious pipe. The configuration is referred to as the porous pipe herein. Although, there are overtones to sand bed channels, it was not the intent to model them, but merely to give some insight into what can be qualitatively expected in flows over porous boundaries.

This chapter presents the general equation of motion for flow in a porous boundary and then through a phenomenological approach presents velocity distributions based on three different eddy viscosity assumptions. Comparison of the models on the basis of the surface velocity indicates the different penetration depths resulting from the assumptions. The core velocity distribution is related to the boundary velocity and the eddy viscosity in an attempt to develop a general model for the entire pipe. Since an explicit expression relating the friction factor to the Reynolds number cannot be achieved, an analysis was made which provided a means of extrapolating the curve of friction factor versus Reynolds number from a known point.

3.2 Flow in a Porous Medium Boundary

The problem posed in this study involves a porous medium exposed to a shear flow. This problem is unusual in that it combines a shear flow and a porous medium flow. Therefore, before attempting to develop the model, consideration will be given to the forces involved.

In the usual connotation of porous medium flow, shear forces do not explicitly enter the problem. A balance of forces is achieved between the pressure and drag forces. Darcy's law for flow in a porous medium is one example of this balance of forces, applying in this case to laminar flows. For flows in the turbulent range the square law drag force has been found to be appropriate. Ward (1964) determined the drag coefficients in terms of physical properties of the fluid and medium appropriate for all flow regimes in porous media. The balance of forces as Ward presented is given by

$$\frac{dp}{d\ell} = \frac{\mu v}{k} + \frac{\rho v^2}{c\sqrt{k}} \qquad (3\text{-}1)$$

where:

$\frac{dp}{d\ell}$ = pressure drop per unit length

μ = viscosity of fluid

ρ = density

k = permeability

c = a dimensionless constant

v = specific discharge

Although flow in crop canopies is not considered as porous medium flow, a striking similarity of flow conditions exists. The crop canopy can be thought of as an anisotropic porous medium. However, in canopy flow a pressure gradient does not enter into the balance of forces. Therefore, the canopy is thought of as a drag on the external flow and in the canopy the drag force is balanced by a shearing force. Cionco (1965) and Takeda (1966) have developed canopy models by balancing the shear force and a drag force proportional to the square of the velocity. Their force balance takes the form

$$\frac{\partial \tau}{\partial z} = \rho \, c_D \, U^2 \qquad (3\text{-}2)$$

where τ = shear or frictional stress

c_D = a drag coefficient dependent upon the vegetation density

U = velocity

z = vertical coordinate

It appears that the boundary flow of the porous pipe should exhibit characteristics of both porous medium flow and canopy flow. If the boundary were of sufficient thickness, shear forces would become negligible with depth, and the usual porous medium flow driven by the pressure gradient would exist. Near the interface boundary, i.e., the nominal porous boundary adjacent to the core flow, a shear flow exists in addition to the porous medium flow. The flow in this region would be similar to the canopy type of flow. If this condition exists, a shear force should be included in the balance of forces for the porous boundary.

Brinkman (1947) was probably the first to include both drag forces and shear forces in a porous medium model. His model attempted to correct for nonlinearity observed in a permeameter containing densely packed porous particles.

The general equation of motion for flow in a porous medium has been developed by Buyevich, et.al., (1969) and is given by

$$n\rho\left(\frac{\partial}{\partial t} + \frac{\partial}{\partial x_j}\right) u_i = -n\left(\frac{\partial p}{\partial x_i} - \rho g_i\right) + \frac{\partial \tau_{ij}}{\partial x_j} - f_{di} \qquad (3\text{-}3)$$

where $\tau_{ij} = \mu\left(\frac{\partial u_i}{\partial x_j} + \frac{\partial u_j}{\partial x_i}\right) - \frac{2}{3}\mu\frac{\partial u_k}{\partial x_k}\delta_{ij}$

τ_{ij} = shear stress components

$f_{di} = \underset{m}{G(n)}\,\underset{m}{|\vec{u}|^m}\,u_i$

f_{di} = drag force components

n = porosity

ρ = density

p = pressure

g_i = components of the body forces associated with the gravitational acceleration

u_i = seepage velocity components

t = time

x_i = coordinate directions

δ_{ij} = Kronecher delta: if $i = j$, $\delta_{ij} = 1$; if $i \neq j$, $\delta_{ij} = 0$

i, j and k = subscripts which can have the values 1,2, or 3

$G_m(n)$ = function of n assumed to be known

m = integer value of 0,1,2....

Assuming the fluid to be incompressible, the equation for the conservation of mass is

$$\frac{\partial u_i}{\partial x_i} = 0 \tag{3-4}$$

The equations of motion for flow in the boundary of a porous pipe can now be developed by starting with the general equations (3-3) and (3-4).

The flow in the porous boundary is regarded as turbulent and the instantaneous quantities can be represented by mean and fluctuating components

$$u_i = \overline{u}_i + u_i' \tag{3-5}$$

$$p = \overline{p} + p' \tag{3-6}$$

The drag forces are assumed to be functions only of the mean velocity, $\overline{u}_i$. Substituting Eqs. (3-5) and (3-6) into Eq. (3-3) and time averaging

gives a resulting equation which can be rearranged and written as

$$\rho \frac{\partial \bar{u}_i}{\partial t} + \rho \bar{u}_i \frac{\partial \bar{u}_i}{\partial x_j} = \frac{\partial \bar{p}}{\partial x_i} + \frac{\partial}{\partial x_j}\left(\mu \frac{\partial \bar{u}_i}{\partial x_j} - \rho \overline{u_i' u_j'} \right) - \frac{\bar{f}_{di}}{n} \qquad (3\text{-}7)$$

The gravitational body forces, g_i, are now included in the pressure, p. Note that Eq. (3-7) is the same as Reynolds equation except for the drag term and represents the general equation of turbulent flow in the porous boundary. In its present form Eq. (3-7) cannot be solved analytically, but by making some gross assumptions concerning the flow field, the equation may be reduced to a more tractable form.

The coordinate system used in the porous pipe is shown in Fig. 3-1. A steady, uniform flow is assumed to exist in the porous pipe. In general the shear stress $\bar{\tau}_{ij}$ is

$$\bar{\tau}_{ij} = \mu \frac{\partial \bar{u}_i}{\partial x_j} - \rho \overline{u_i' u_j'} \qquad (3\text{-}8)$$

For turbulent flows, the Reynolds stresses are considered to dominate, i.e., $\bar{\tau}_{ij} \simeq -\rho \overline{u_i u_j}$. For laminar flows, the viscous stresses dominate, i.e., $\bar{\tau}_{ij} \simeq \mu \frac{d\bar{u}_i}{dx_j}$

Using the above assumptions, Eq. (3-7) becomes

$$-\frac{\partial \bar{p}}{\partial x_i} + \frac{\partial \bar{\tau}_{ij}}{\partial x_j} - \frac{f_{di}}{n} = 0 \qquad (3\text{-}9)$$

This is the general equation of motion for flow in the boundary of the porous pipe. For the specific flow with

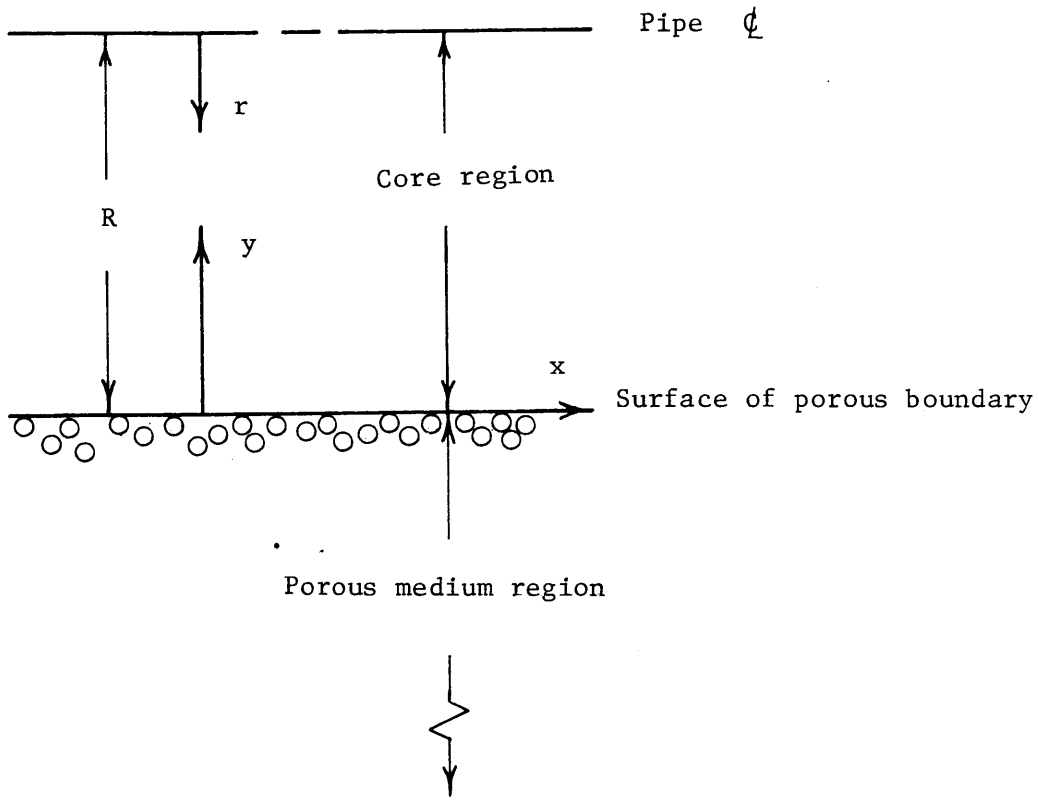

Fig. 3-1 Coordinate system used in models of porous boundary flow

$$\overline{u}_1 = u \tag{3-10}$$

let

$$x_1 = x \tag{3-11}$$

$$f_{d1} = f_d \tag{3-12}$$

$$x_2 = y \tag{3-13}$$

$$\overline{\tau}_{ij} = \tau \tag{3-14}$$

Eq. (2-10) reduces to

$$-\frac{\partial p}{\partial x} + \frac{\partial \tau}{\partial y} - \frac{f_d}{n} = 0 \tag{3-15}$$

where the over bars are dropped as a matter of convenience. Equation (3-15) only can be solved by making assumptions regarding the shear stress, τ, and the drag force, f_d.

The shear stress to be used in the development of the velocity profiles follows from phenomenological theories of turbulence and is assumed proportional to a kinematic eddy viscosity, ε, and the velocity gradient, $\frac{du}{dy}$, such that

$$\tau = \rho \, \varepsilon \, \frac{du}{dy} \tag{3-16}$$

Different functional forms of the eddy viscosity, ε, have been used to determine mean velocities in turbulent flows. Some simple forms the functions can take are

$$\left.\begin{aligned} \varepsilon &= u_* L \\ \varepsilon &= uL \end{aligned}\right\} \tag{3-17}$$

where L = some characteristic length

u_* = shear velocity

u = seepage velocity

Forms of eddy viscosity given in Eq. (3-17) are used to develop the mean velocity profiles for the porous boundary, later in this chapter.

The drag force considered to be the most general for porous media is that presented by Ward. The form of the drag force used in canopy flows is implied in Ward's equation. Therefore, no additional terms need be included to account for drag for the canopy type flows. The drag force used to develop the velocity profiles later in this chapter takes the form of Ward's equation and is

$$\frac{f_d}{n} = \frac{\rho\nu}{k} u + \frac{\rho}{c\sqrt{k}} u^2 \tag{3-16}$$

Replacing f_d in Eq. (3-15) with Eq. (3-16) gives

$$-\frac{\partial p}{\partial x} + \frac{\partial \tau}{\partial y} - \frac{\rho\nu}{k} u - \frac{\rho u^2}{c\sqrt{k}} = 0 \tag{3-17}$$

If the shear stress term is zero, Eq. (3-17) reduces to a form of Ward's equation for flow in a porous medium. If a pressure gradient does not exist and the linear drag term can be neglected, Eq. (2-17) approaches the form of the equations used in canopy flows. For the development of the velocity profiles in the following sections, Eq. (3-17) represents the governing equation of motion in the porous boundary.

3.3 Mathematical Models Assuming Eddy Viscosity Constant

The nature of the flow in the boundary of the porous pipe will be considered before developing the velocity distribution. The nature of the flow in the porous pipe can be characterized by visualizing two small packets of fluid such as those represented schematically in Fig. 3-2. The two packets at different levels try to move into different regions with higher or lower momentum. It can be seen readily that it may not be possible for these packets always to move from one level to another. They may be intercepted by a porous medium particle and give up their momentum to it. Thus, small scale turbulence in the porous boundary would be quickly damped out or be relatively insignificant.

If the large scale eddies from the core flow that impinge on the surface are considered, it appears that the porous medium would offer some resistance to its passage but would not significantly hinder its movement. Therefore, it is assumed that the large scale eddies are the generating mechanism of the turbulence in the porous boundary. Furthermore, since the eddy scale is relatively large compared with the pore scale of the boundary, the mixing process should be constant over a large area. Therefore, it seems appropriate that the eddy viscosity be assumed a constant as a first approximation. Two different forms of the eddy viscosity were used to develop velocity profiles in the porous boundary. The first assumption was that the eddy viscosity was a function of the velocity at the interface between core flow and the boundary, i.e., the surface velocity. It is given by

$$\varepsilon = BL\ (u_s - u_1) = BL\ \hat{u}_o \qquad (3\text{-}19)$$

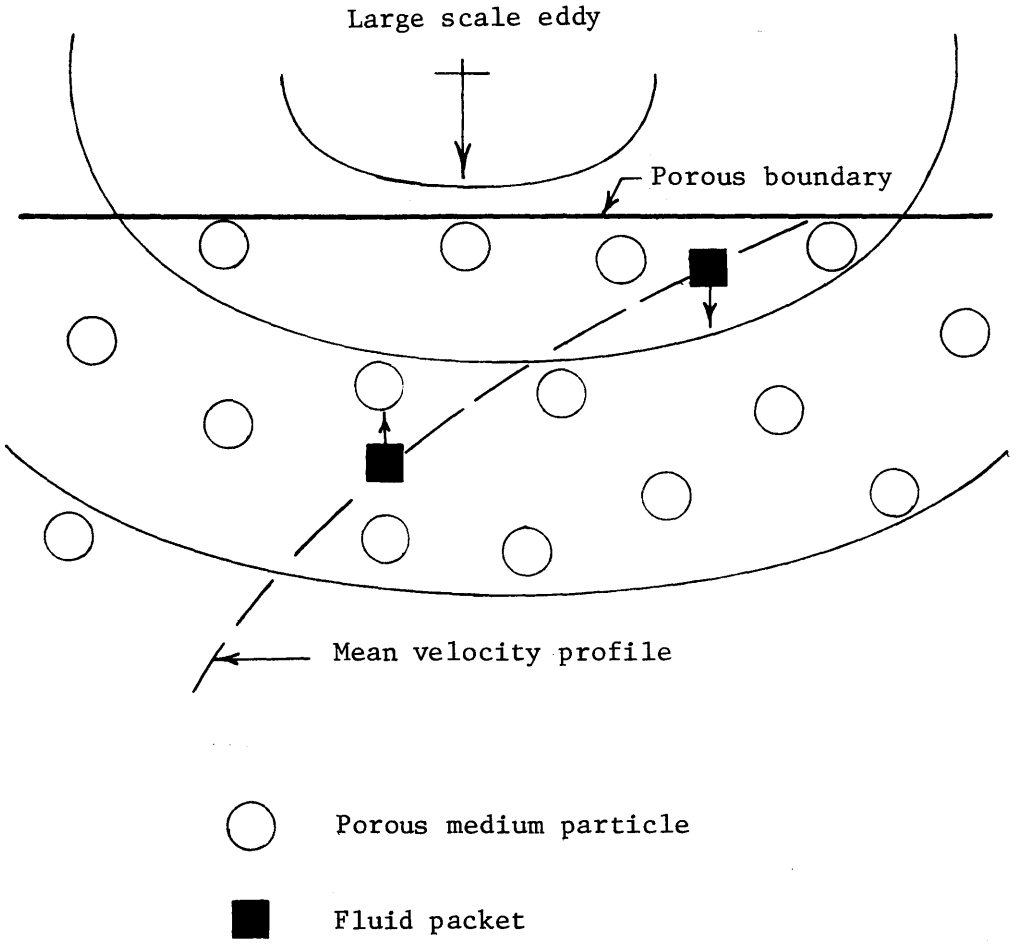

Fig. 3-2 Schematic representation of flow in the porous pipe boundary

where B = constant of proportionality

L = a length characteristic of the boundary

$$\hat{u}_o = u_s - u_1 \tag{3-19}$$

u_s = surface velocity

u_1 = porous medium pressure gradient flow which can be determined from

$$nu_1 = -\frac{\nu c}{2\sqrt{k}} + \frac{1}{2}\sqrt{\frac{\nu^2 c^2}{k} + \frac{8c\sqrt{k}}{R}u_*^2} \tag{3-20}$$

which is the solution of Eq. (3-1) when $dp/d\ell$ is replaced by

$$\frac{\rho u_*^2}{2R}$$

R = porous pipe radius

The second assumption was that the eddy viscosity was a function of this shear velocity, u_*. It is given by

$$\varepsilon = BL\, u_* \tag{3-24}$$

The velocity distribution using the first eddy viscosity, Eq. (3-18), will be completely developed and documented. Since the velocity profile development using the second eddy viscosity assumption parallels the first, only an outline of the differences in principal equations is noted before presenting the final solution.

The coordinate system used in the models was shown in Fig. 3-1. The boundary conditions appropriate for all models are

$$\tau = \tau_o = \rho\varepsilon \frac{du}{dy} \quad \text{at } y = 0 \tag{3-22}$$

$$\tau = \rho\varepsilon \frac{du}{dy} \qquad \text{at } y \to -\infty \tag{3-23}$$

where τ_o = shear stress at the surface of the boundary.

The first boundary condition, Eq. (3-22), implies the shear stress across the interface boundary is continuous. The second condition indicates that no stress exists to great depths in the boundary, and at that depth the flow is sustained by the pressure gradient, therefore, $u = u_1$.

Using the constant eddy viscosity assumption, Eq. (3-18), the equation of motion in the porous boundary, Eq. (3-17), can be rearranged and written as

$$\rho BL \hat{u}_o \frac{d^2u}{dy^2} = \rho \frac{\nu}{k}(u - u_1) + \frac{\rho}{c\sqrt{k}}(u^2 - u_1^2) \tag{3-24}$$

Total derivatives replace the partial derivatives since u is only a function of y. The equation of motion and the boundary conditions can be made nondimensional by normalizing with the shear velocity, u_*, and a characteristic length, L, such that

$$u = Uu_*,\ u_1 = U_1 u_*,\ \hat{u}_o = \hat{U}_o u_* \tag{3-25}$$

$$y = L\xi \tag{3-26}$$

Substituting Eqs. (3-25) and (3-26) into Eq. (3-24) and rearranging gives

$$B\hat{u}_o \frac{d^2u}{d\xi^2} = \frac{\nu L}{ku_*}(u - u_1) + \frac{L}{c\sqrt{k}}(u^2 - u_1^2) \tag{3-27}$$

Letting $\hat{U} = U - U_1$ (3-28)

and noting that $\frac{d\hat{U}}{d\xi} = \frac{dU}{d\xi}$ (3-29)

Eq. (3-27) can be written as

$$\frac{B\hat{U}_o}{\beta} \frac{d^2U}{d\xi^2} = \frac{A}{\beta} \hat{U} + \hat{U}^2 \tag{3-30}$$

where $\beta = \frac{L}{c\sqrt{k}}$ (3-31)

$$A = \frac{\nu L}{k u_*} + 2\beta U_1 \tag{3-32}$$

The boundary conditions, Eqs. (3-22) and (3-23), can be written in nondimensional form as

$$\frac{dU}{d\xi} = \frac{1}{B\hat{U}_o} \quad \text{at } \xi = 0 \tag{3-33}$$

$$\frac{dU}{d\xi} = 0 \quad \text{at} \quad \xi \to -\infty \tag{3-34}$$

which from Eq. (3-23) implies $\hat{U} = 0$ at $\xi \to -\infty$

To find the solution of Eq. (3-30) subject to Eqs. (3-33) and (3-34), let

$$S = \frac{d\hat{U}}{d\xi} \tag{3-35}$$

and $$\frac{d}{d\xi} = \frac{d}{d\hat{U}} \frac{d\hat{U}}{d\xi} = S \frac{d}{d\hat{U}} \tag{3-36}$$

Substituting Eq. (3-35) and (3-36) into Eq. (3-30) gives

$$\frac{\hat{BU}_o}{2\beta}\ \frac{dS^2}{d\hat{U}} = \frac{A}{\beta}\hat{U} + \hat{U}^2 \tag{3-37}$$

The result of integrating Eq. (3-37) and using the boundary condition Eq. (3-34) is

$$\frac{\hat{BU}_o}{2\beta}\ S^2 = \frac{A}{2\beta}\ \hat{U}^2 + \frac{\hat{U}^3}{3} \tag{3-38}$$

The surface velocity, $\hat{U}_o$, can be determined by substituting the value $S = (\hat{BU}_o)^{-1}$ from Eq. (3-33) into Eq. (3-38) giving

$$\frac{1}{\hat{BU}_o} = A\hat{U}_o^{\,2} + \frac{2\beta}{3}\hat{U}_o^{\,3} \tag{3-39}$$

The solution is not straight forward and is best found using an iteration procedure in a digital computer.

By taking the square root of Eq. (3-38), it can be written as

$$\sqrt{\frac{\hat{BU}_o}{2\ \beta}}\ \ \frac{d\hat{U}}{d\xi} = \hat{U}\left(\frac{A}{2\beta} + \frac{\hat{U}}{3}\right)^{1/2} \tag{3-40}$$

This equation can be separated and integrated to give

$$\sqrt{\frac{2\beta}{A}}\ \ln\left\{\frac{\left(\frac{\hat{U}}{3} + \frac{A}{2\beta}\right)^{1/2} - \frac{A}{2\beta}}{\left(\frac{\hat{U}}{3} + \frac{A}{2\beta}\right)^{1/2} + \frac{A}{2\beta}}\right\} + D = \sqrt{\frac{2\beta}{\hat{BU}_o}}\ \xi \tag{3-41}$$

The value of the constant of integration, D, can be determined from the fact that at $\xi = 0$, $\hat{U} = \hat{U}_o$ and the solution for the velocity distribution in the porous boundary then becomes

$$\ln\left\{\frac{\left(\frac{\hat{U}}{3}+\frac{A}{2\beta}\right)^{1/2}-\frac{A}{2\beta}}{\left(\frac{\hat{U}}{3}+\frac{A}{2\beta}\right)^{1/2}+\frac{A}{2\beta}}\right\}-\ln\left\{\frac{\left(\frac{\hat{U}_o}{3}+\frac{A}{2\beta}\right)^{1/2}-\frac{A}{2\beta}}{\left(\frac{\hat{U}_o}{3}+\frac{A}{2\beta}\right)^{1/2}+\frac{A}{2\beta}}\right\}=\sqrt{\frac{A}{B\hat{U}_o}}\,\xi \quad (3\text{-}42)$$

Since the value of A depends upon the Reynolds number through the shear velocity, u_*, the solution for Eq. (3-42) also depends on the Reynolds number. Furthermore, the proportionality constant, B, has not been specified. It is assumed to be a universal constant, but its value will depend on the characteristic length scale chosen, and at this point B must be determined empirically. However, the velocity distribution can be determined by assuming different values of B if the value of u_* is known. The values of u_* are known for several values of pipe Reynolds numbers from the experiments performed by Muñoz. The velocity profiles shown in Figs. 3-3, 3-4 and 3-5 were determined for different values of B at Reynolds numbers of 1×10^5, 2×10^5 and 4×10^5. The values of the eddy viscosity at the surface corresponding to the different values of B also are given in the figures. The velocity distributions shown in Fig. 3-6 are exactly the same as those in Fig. 3-5 except they are plotted using a linear scale instead of a semi-log scale. The linear scale eliminates the distortion and is presented here to aid in visualizing how rapidly the velocity decreases.

If the eddy viscosity assumption, Eq. (3-21), is used, the solution for the velocity distribution is the same as Eq. (3-42) except for the coefficient on the right hand side of Eq. (3-42). In that equation the surface velocity does not appear and the coefficient is

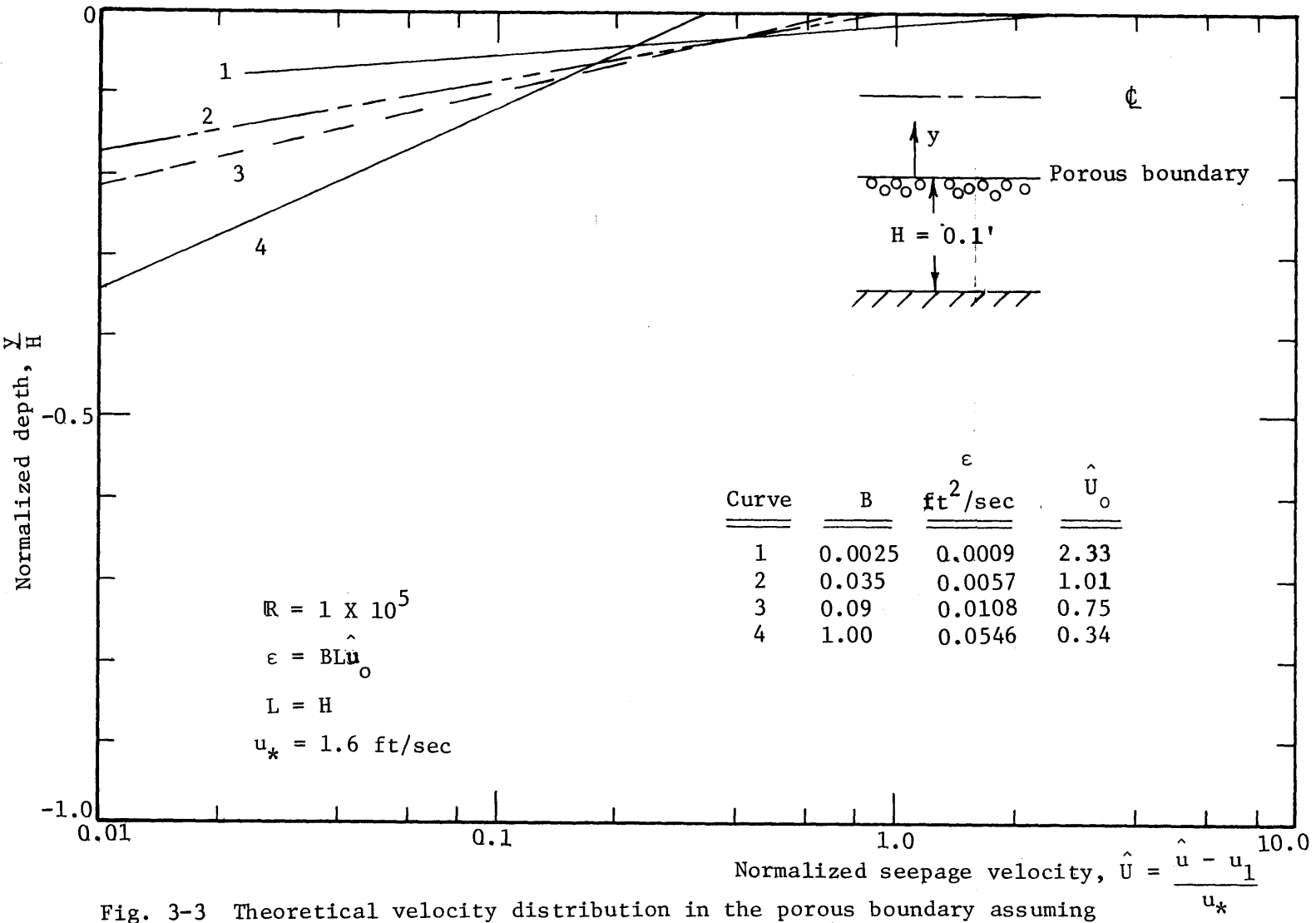

Fig. 3-3 Theoretical velocity distribution in the porous boundary assuming eddy viscosity proportional to the surface velocity, $\mathbb{R} = 1 \times 10^5$

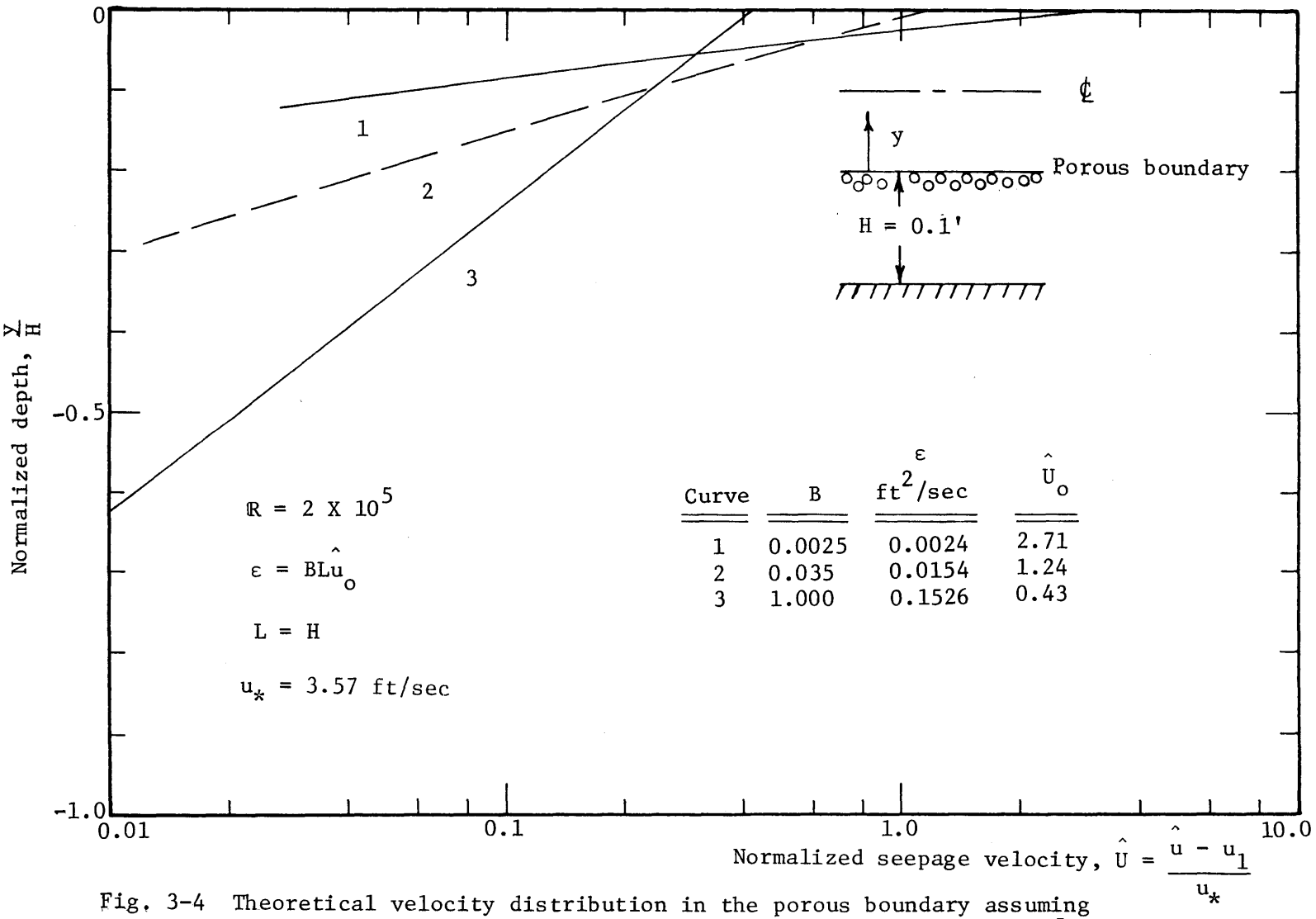

Fig. 3-4 Theoretical velocity distribution in the porous boundary assuming eddy viscosity proportional to the surface velocity, $\mathbb{R} = 2 \times 10^5$

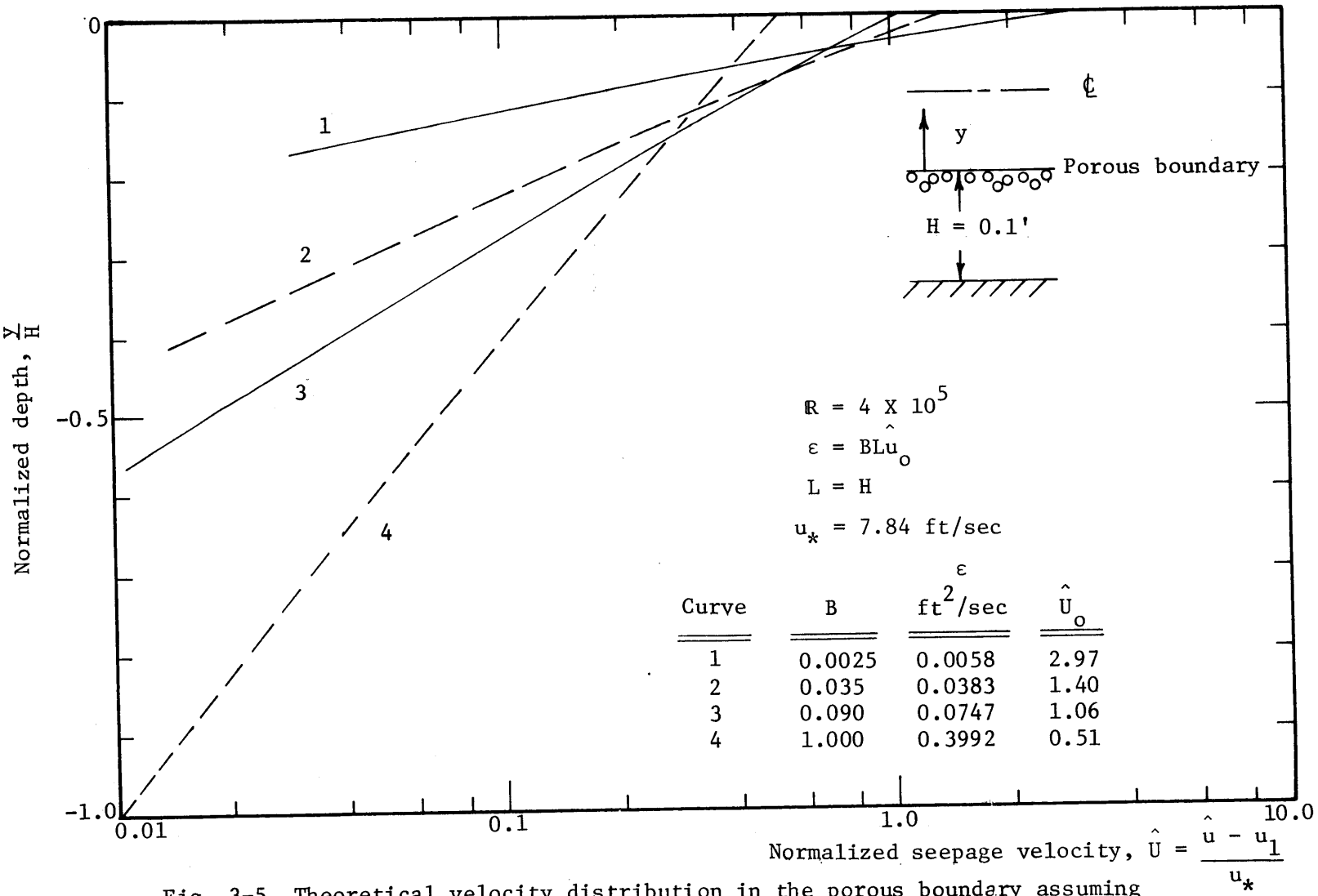

Fig. 3-5 Theoretical velocity distribution in the porous boundary assuming eddy viscosity proportional to the surface velocity, $\mathbb{R} = 4 \times 10^5$

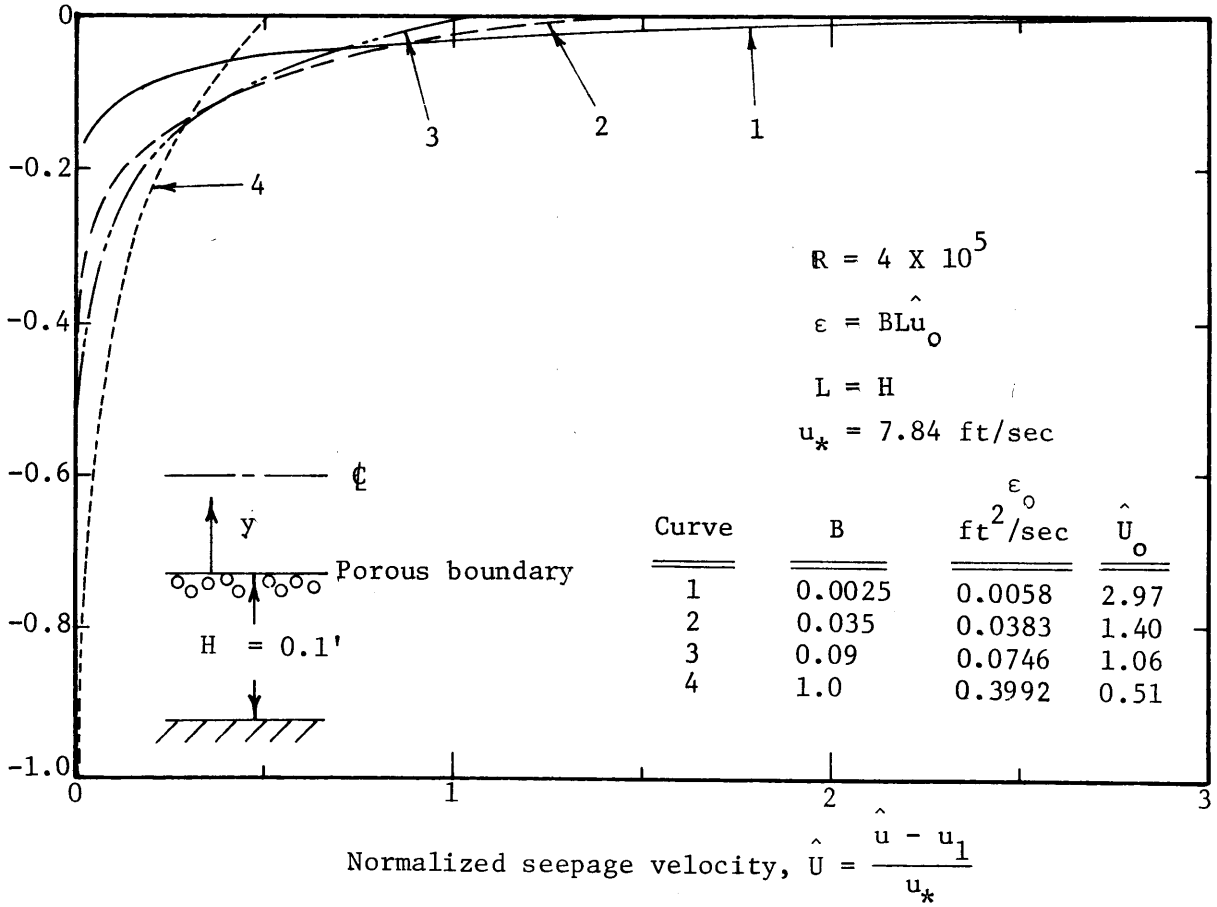

Fig. 3-6 Theoretical velocity distribution in the porous boundary assuming eddy viscosity proportional to the surface velocity, $\mathbb{R} = 4 \times 10^5$

$\sqrt{\frac{A}{B}}$. The boundary conditions become

$$\frac{d\hat{U}}{d\xi} = \frac{1}{B} \quad \text{at} \quad \xi = 0 \tag{3-43}$$

and

$$\frac{d\hat{U}}{d\xi} = 0 \quad \text{at} \quad \xi \to -\infty \tag{3-44}$$

The velocity distribution for the assumption, $\varepsilon = BLu_*$ can be written as

$$\ln\left[\frac{\left(\frac{\hat{U}}{3}+\frac{A}{2\beta}\right)^{1/2}-\frac{A}{2\beta}}{\left(\frac{\hat{U}}{3}+\frac{A}{2\beta}\right)^{1/2}+\frac{A}{2\beta}}\right] - \ln\left[\frac{\left(\frac{\hat{U}_o}{3}+\frac{A}{2\beta}\right)^{1/2}-\frac{A}{2\beta}}{\left(\frac{\hat{U}_o}{3}+\frac{A}{2\beta}\right)^{1/2}+\frac{A}{2\beta}}\right] = \sqrt{\frac{A}{B}}\,\xi \tag{3-45}$$

The surface velocity can be determined by using Eq. (3-43) for S in the following equation evaluated at $\xi = 0$

$$\frac{B}{2\beta} S^2 = \frac{A}{2\beta} \hat{U}^2 + \frac{\hat{U}^3}{3} \tag{3-46}$$

This completes the solution for the velocity distribution in the porous boundary using the assumption for eddy viscosity, $\varepsilon = BLu_*$. Velocity profiles at the different pipe Reynolds numbers and for different values of B are given in Figs. 3-7, 3-8 and 3-9.

Eqs. (3-42) and (3-45) give identical profiles when $\hat{U}_o = 1$. For values of $\hat{U}_o > 1$, the eddy viscosity, $\varepsilon = BL\hat{U}_o$, is larger for a given value of B. For values of $\hat{U}_o < 1$, the inverse is true.

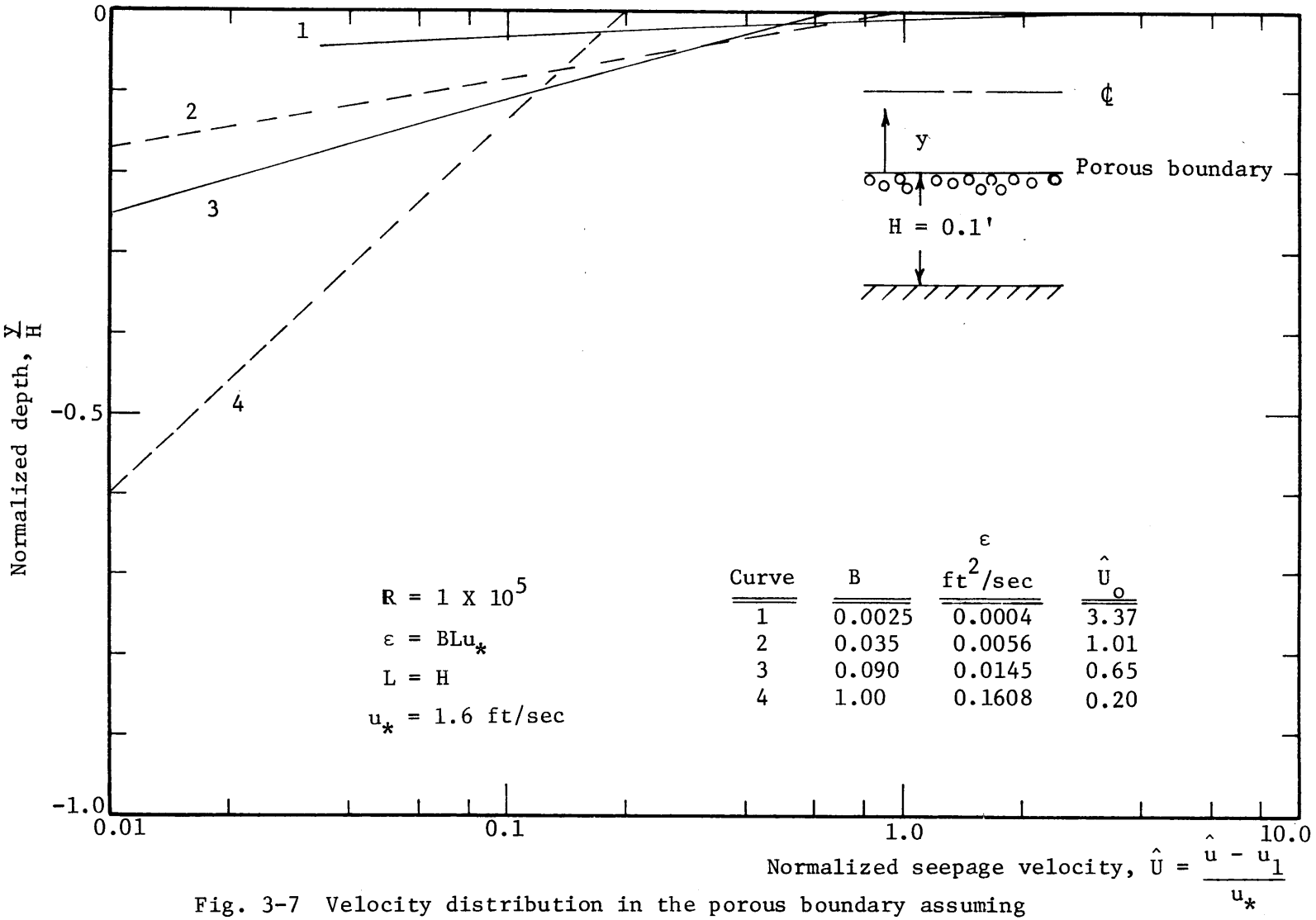

Fig. 3-7 Velocity distribution in the porous boundary assuming eddy viscosity proportional to shear velocity, R = 1 X 10^5

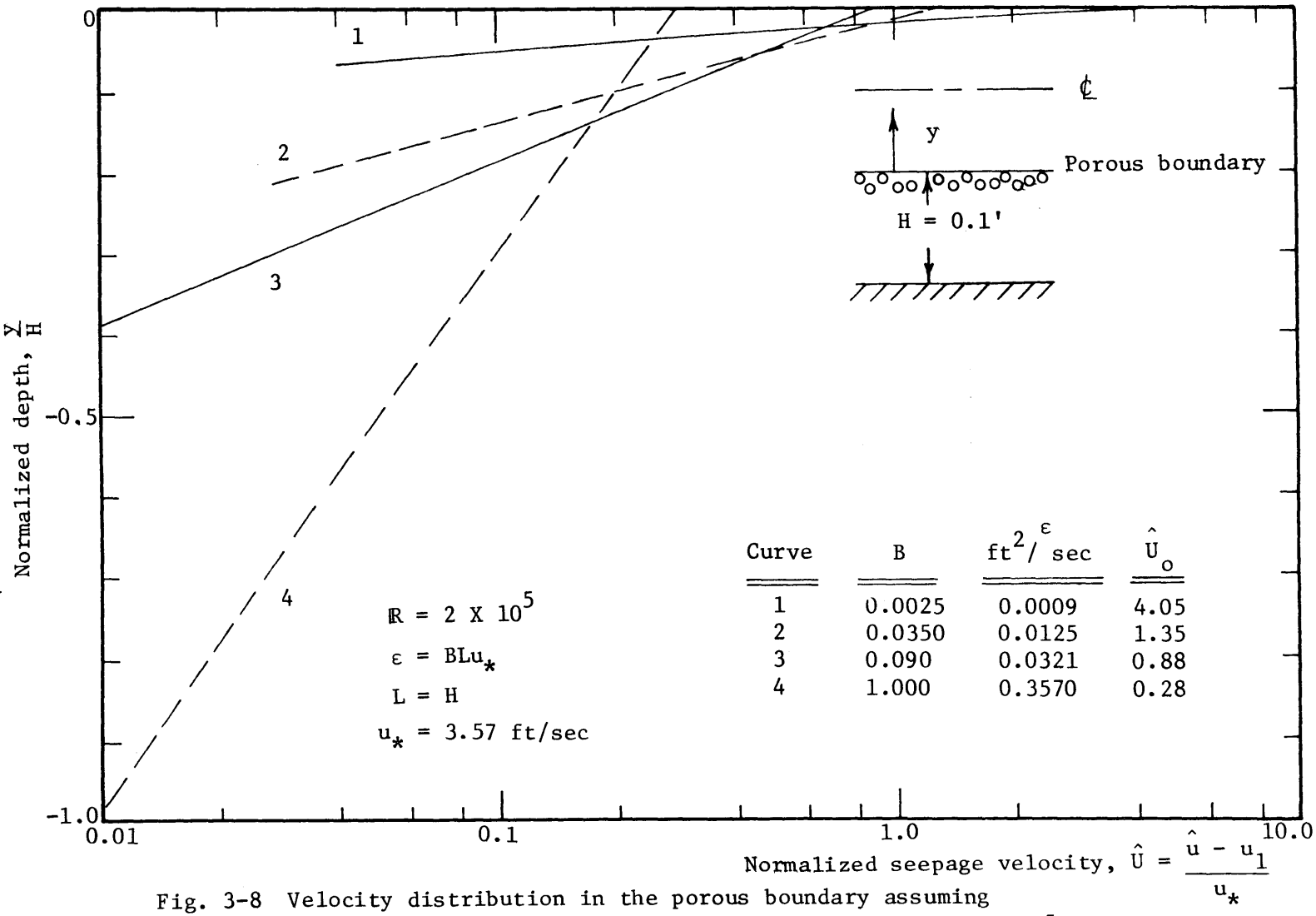

Fig. 3-8 Velocity distribution in the porous boundary assuming eddy viscosity proportional to shear velocity, $\mathbb{R} = 2 \times 10^5$

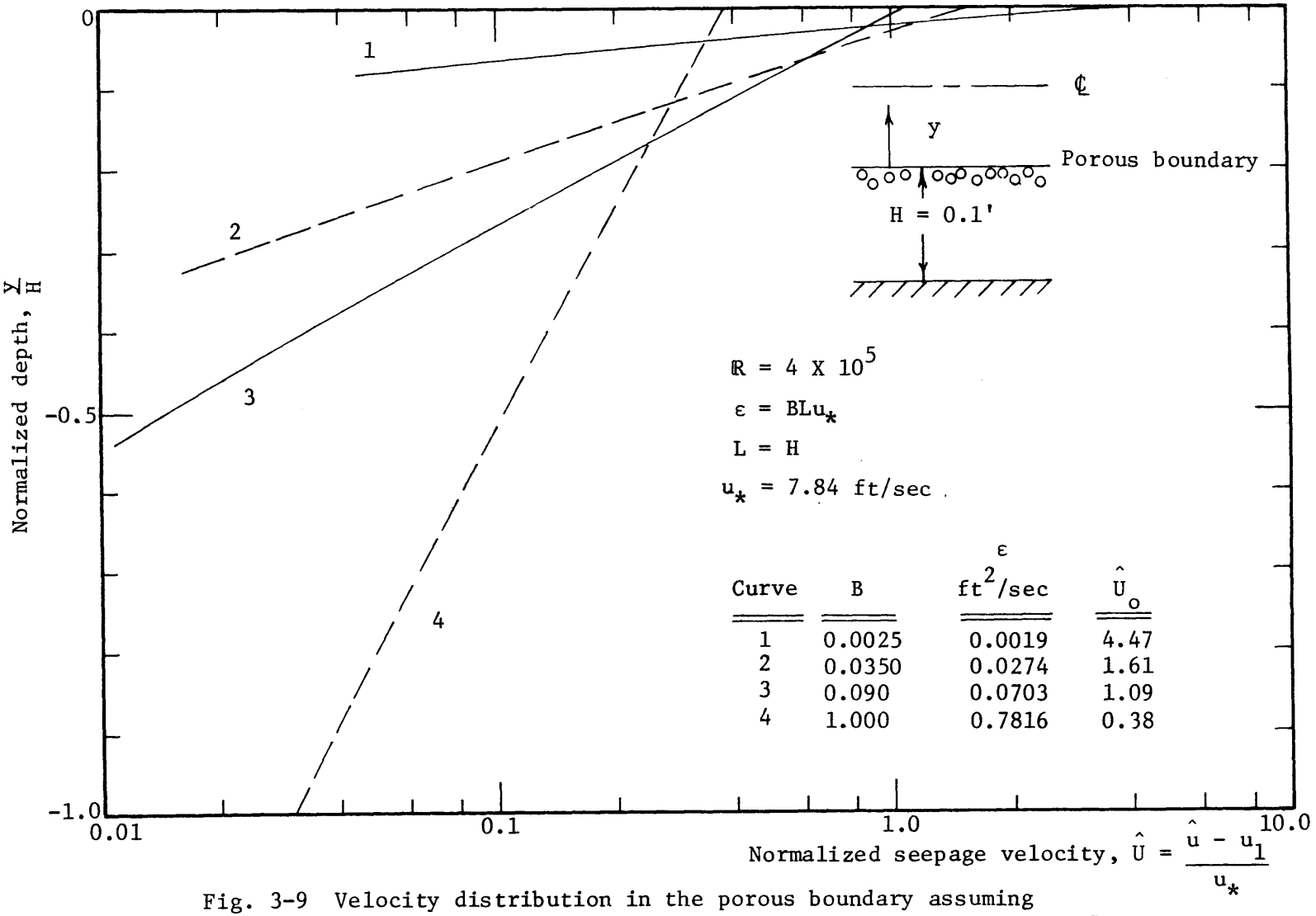

Fig. 3-9 Velocity distribution in the porous boundary assuming eddy viscosity proportional to shear velocity, $\mathbb{R} = 4 \times 10^5$

3.4 Mathematical Model Assuming Eddy Viscosity Proportional to Velocity

To investigate the effects of a variable eddy viscosity, the assumption was made that the eddy viscosity was proportional to the velocity in the boundary. This can be written as

$$\varepsilon = BL\hat{U} \tag{3-47}$$

where $\hat{U}$ is defined by Eq. (3-28). The physical significance of this assumption is that the lateral turbulent motion may decrease with increased depth into the porous boundary and thus the eddy viscosity should also decrease. Velocity profiles using this assumption were developed for later comparison with the constant eddy viscosity profiles.

The general equations of motion for this model, after substitution of Eq. (3-47) into Eq. (3-17), can be made nondimensional by using Eqs. (3-25) and (3-26) and becomes

$$\frac{B}{2\beta}\frac{d^2\hat{U}^2}{d\xi^2} = \frac{A}{\beta}\hat{U} + \hat{U}^2 \tag{3-48}$$

where β and A are defined by Eqs. (3-31) and 3-32), respectively. The boundary conditions appropriate for this problem are

$$\frac{d\hat{U}}{d\xi} = \frac{1}{B} \quad \text{at } \xi = 0$$

$$\frac{d\hat{U}}{d\xi} = 0 \quad \text{at } \xi \to -\infty \tag{3-49}$$

or $$\hat{U} = 0 \quad \text{at } \xi \to -\infty$$

To find the solution of Eq. (3-48) subject to Eq.(3-49), let

$$S_1 = \frac{1}{2} \frac{d\hat{U}^2}{d\xi} = \hat{U} \frac{d\hat{U}}{d\xi} \tag{3-50}$$

then

$$\frac{d}{d\xi} = \frac{d}{d\hat{U}} \frac{d\hat{U}}{d\xi} = \frac{S_1}{\hat{U}} \frac{d}{d\hat{U}} \tag{3-51}$$

Substituting Eqs. (3-50) and (3-51) into (3-48) gives

$$\frac{B}{\beta} \frac{S_1}{\hat{U}} \frac{dS}{d\hat{U}} = \frac{A}{\beta} \hat{U} + \hat{U}^2 \tag{3-52}$$

which can be separated and integrated to give

$$\frac{B}{\beta} \frac{S_1^2}{2} = \frac{A}{3\beta} \hat{U}^3 + \frac{\hat{U}^4}{4} + G \tag{3-53}$$

The boundary condition, Eq. (3-49), at $\xi \to -\infty$ is used to find

$$G = 0 \tag{3-54}$$

The surface velocity can be found using Eq. (3-53) and the boundary condition at $\xi = 0$. The equation from which $\hat{U}_o$ can be evaluated is

$$\frac{1}{B\beta} = \frac{2A}{3\beta} \hat{U}_o^3 + \frac{\hat{U}_o^4}{2} \tag{3-55}$$

After taking the square root of Eq. (3-53), it can be separated and integrated to yield

$$\sqrt{\frac{B}{2\beta}} \ln\left(\frac{\hat{U}}{2} + \frac{A}{3\beta} + \sqrt{\frac{\hat{U}^2}{4} + \frac{A}{3\beta} \hat{U}} \right) + D = \xi \tag{3-56}$$

The value of D can be found by using the fact that $\hat{U} = \hat{U}_o$ at $\xi = 0$.

Evaluating D and substituting it into Eq. (3-56) gives the velocity distribution in the porous boundary as

$$\sqrt{\frac{B}{2\beta}}\ \ln\left[\frac{\frac{\hat{U}}{2}+\frac{A}{3\beta}+\left(\frac{\hat{U}^2}{4}+\frac{A}{3\beta}\hat{U}\right)^{1/2}}{\frac{\hat{U}_o}{2}+\frac{A}{3\beta}+\left(\frac{\hat{U}_o}{4}+\frac{A}{3\beta}\hat{U}_o\right)^{1/2}}\right] = \xi \qquad (3\text{-}57)$$

The above solution also depends upon the Reynolds number and the value of B as did those found for the constant eddy viscosity assumptions. Therefore, the velocity distribution given in Figs. (3-10), (3-11) and (3-12) were determined for different values of B at values of u_* corresponding to the Reynolds numbers at which Muñoz performed his experiments.

3.5 Comparison of Mathematical Models

The three mathematical models differ in the initial assumption concerning the eddy viscosity. The different assumptions produce different solutions for the velocity distributions in the porous boundary. Since all of the profiles extend in theory to $-\infty$, the criterion used for comparison was the depth at which the velocity, $\hat{U}$, was one percent of the surface velocity, $\hat{U}_o$. This depth is herein referred to as the penetration depth. Where possible the profiles start at the same surface velocity.

The constant eddy viscosities in general produce flatter velocity profiles since they provide a source which allows a larger momentum transfer to exist at greater depths in the boundary. The assumption of eddy viscosity proportional to the velocity, on the other hand, decreases the amount of momentum transfer at a rate proportional to both

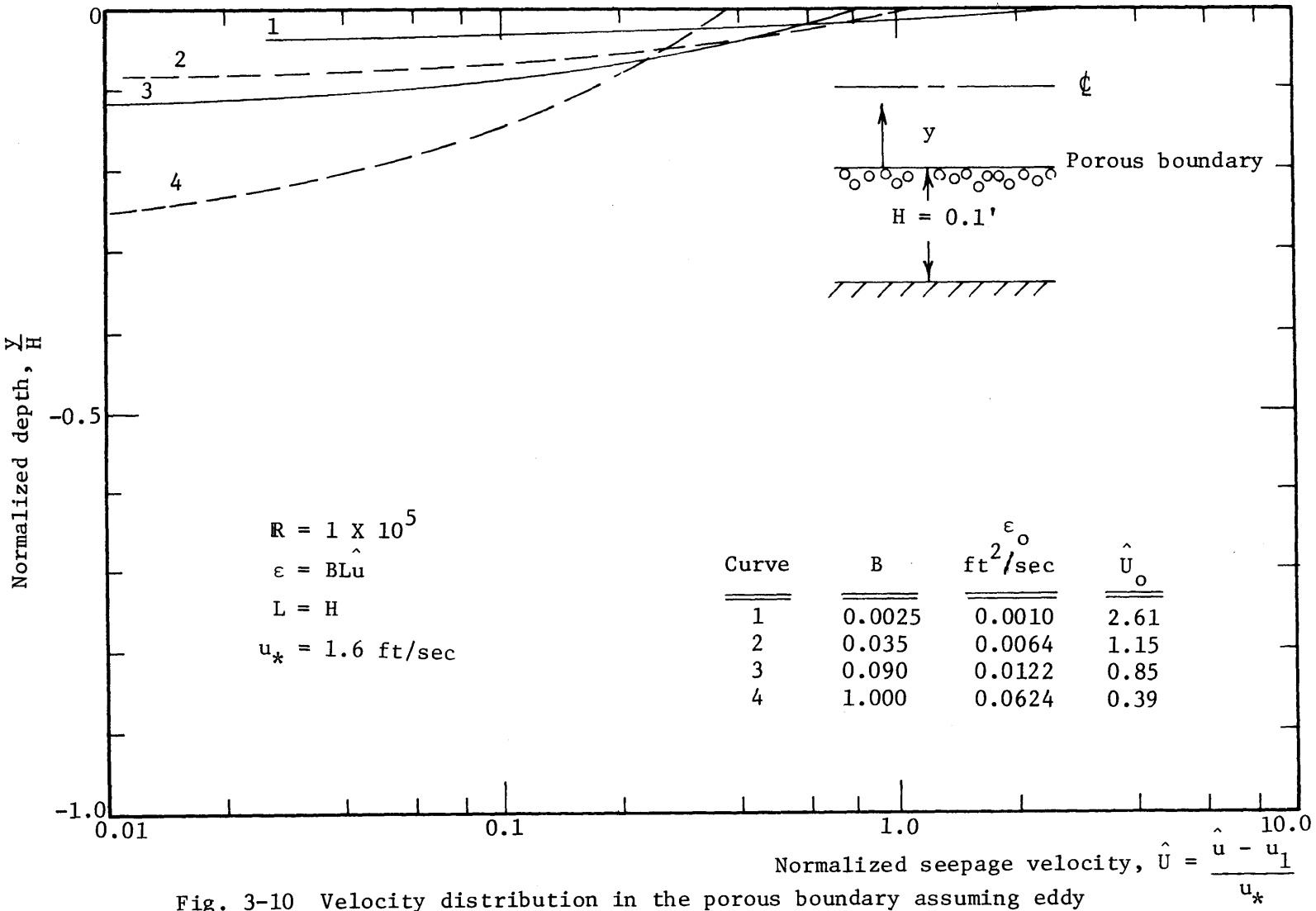

Curve	B	ε_o ft²/sec	$\hat{U}_o$
1	0.0025	0.0010	2.61
2	0.035	0.0064	1.15
3	0.090	0.0122	0.85
4	1.000	0.0624	0.39

Fig. 3-10 Velocity distribution in the porous boundary assuming eddy viscosity proportional to local mean velocity, $R = 1 \times 10^5$

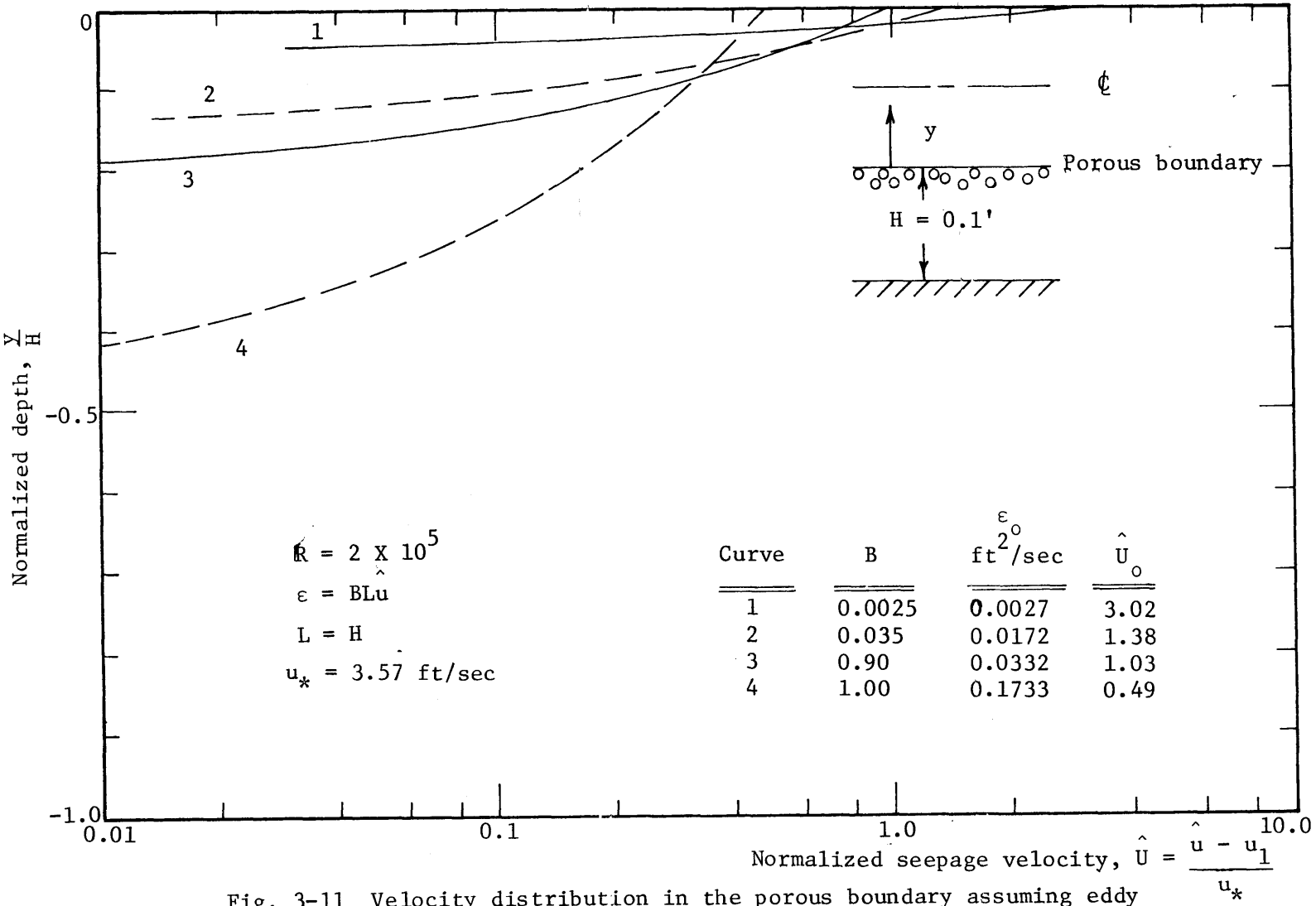

Fig. 3-11 Velocity distribution in the porous boundary assuming eddy viscosity proportional to local mean velocity, $\mathbb{R} = 2 \times 10^5$

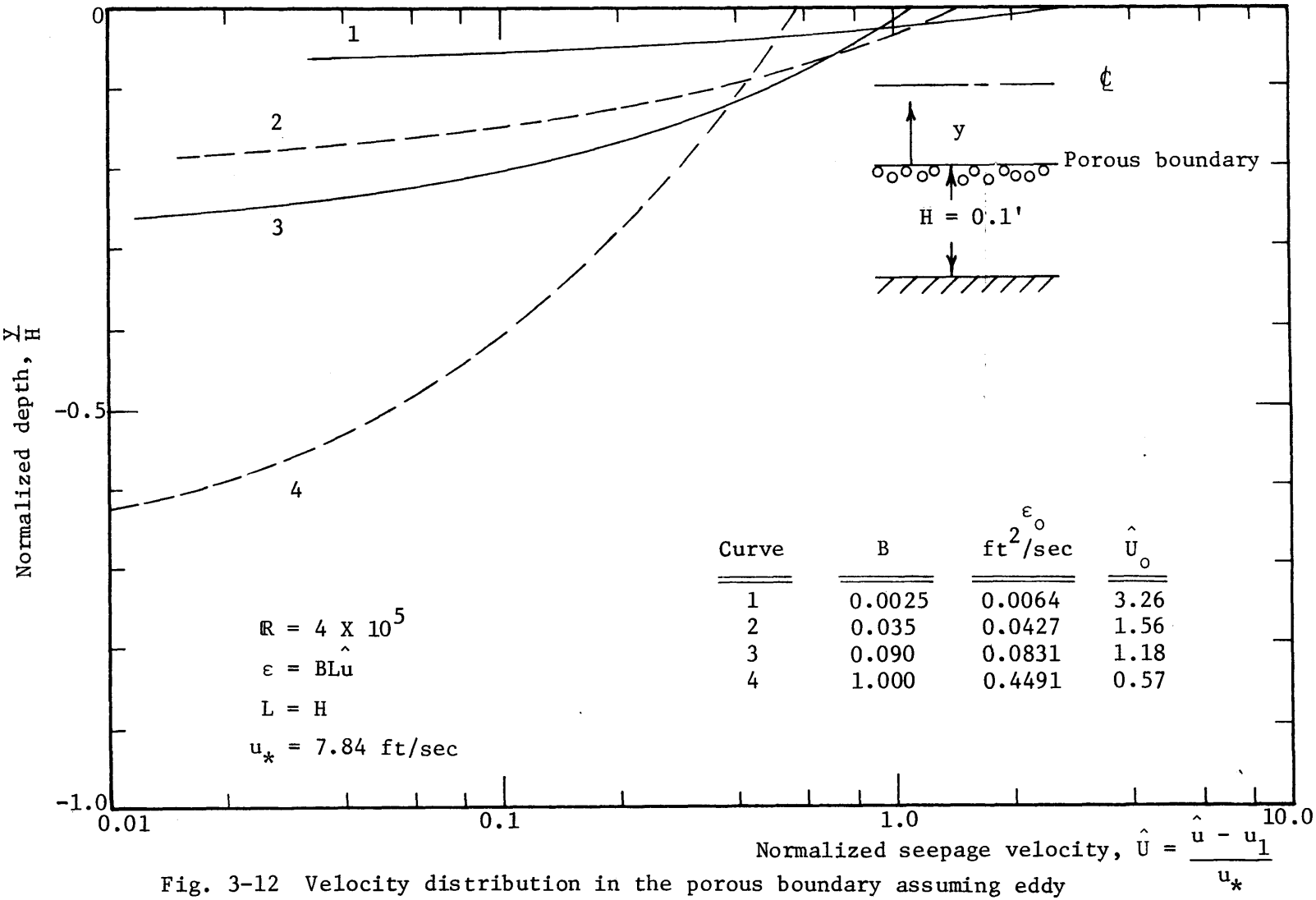

Fig. 3-12 Velocity distribution in the porous boundary assuming eddy viscosity proportional to local mean velocity, $R = 4 \times 10^5$

the velocity and the velocity gradient. Therefore, the velocity decreases more rapidly with depth in the porous boundary. The differences are evident in Fig. 3-13 which is typical of the profiles for all Reynolds numbers.

When the surface velocity, $\hat{U}_o$, is equal to one, the two constant viscosity assumptions are identical and produce the same profile. For values of $\hat{U}_o$ greater than one the assumption of $\varepsilon = BL\hat{U}_o$ allows greater momentum at greater depths; thus the velocity profile penetrates the boundary more as is seen in comparing curves 3, 4, and 5 of Fig. (3-14). At values of $\hat{U}_o$ less than one the reverse is true and the assumption of $\varepsilon = BLU_*$ indicates the velocity penetrates the boundary more than that of $\varepsilon = BL\hat{U}_o$ or $\varepsilon = BL\hat{U}$. In all cases, the penetration depth was a minimum for the assumption, $\varepsilon = BL\hat{U}$, for any given value of $\hat{U}_o$.

Curves representing the velocity distributions predicted from the models for a value of B = 0.025 are shown in Figs. 3-14, 3-15 and 3-16. Also indicated on the figures are the range of velocities measured at the different positions which were given in Figs. 2-25, 2-29 and 2-31 of Chapter 2. The velocity distributions tend to be within the range of measured velocities at the lower Reynolds number flows. At the highest Reynolds number, $\mathbb{R} = 4 \times 10^5$, none of the distributions matched the measured velocities in the region of the large velocity gradient of the curve. This may be due to the interpretation of the anemometer data in this region. The correlation of one half the anemometer velocity reading representing the seepage velocity was based upon measurements made under uniform flow conditions which were relative-

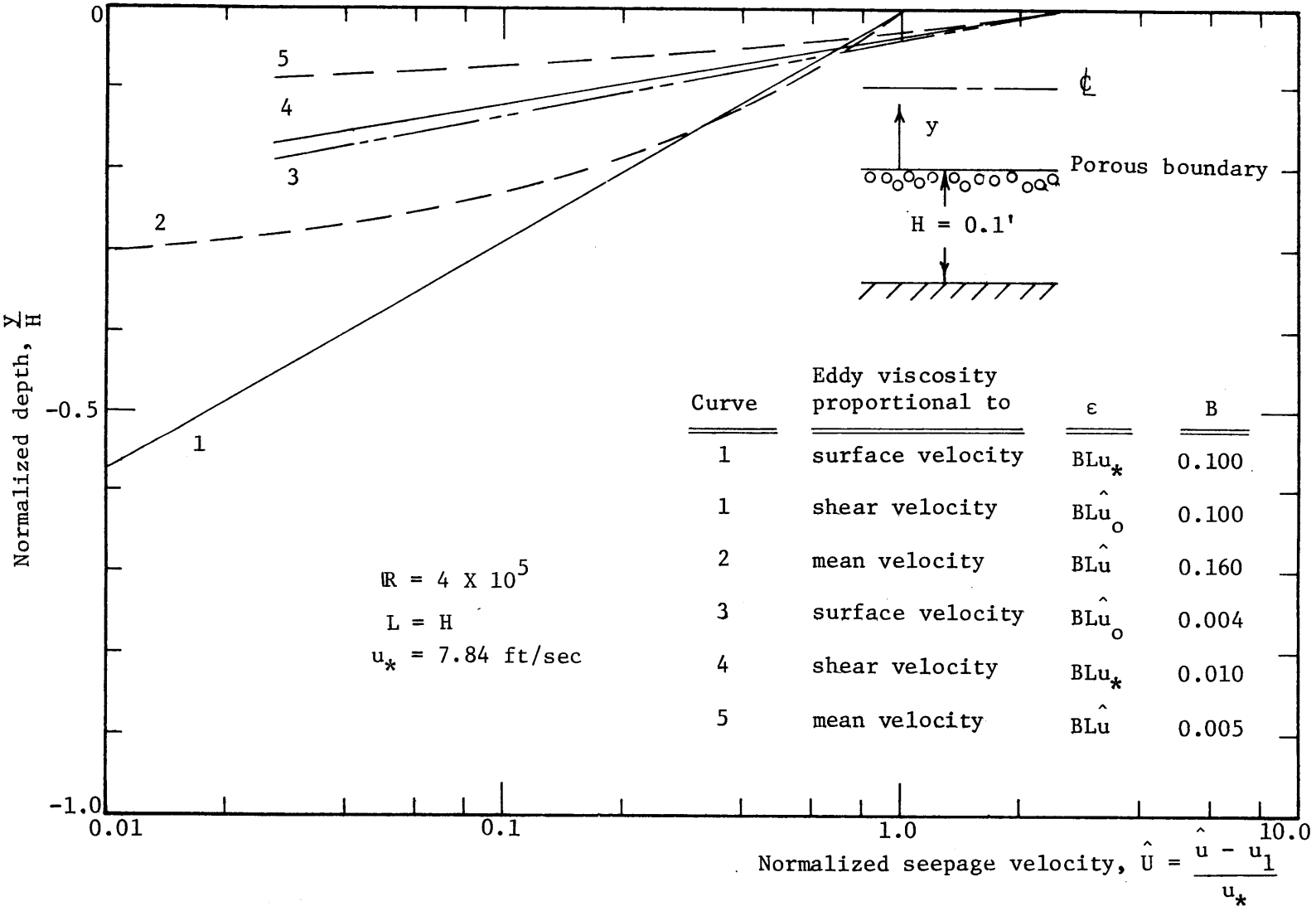

Fig. 3-13 Summary of velocity distributions from the three eddy viscosity models

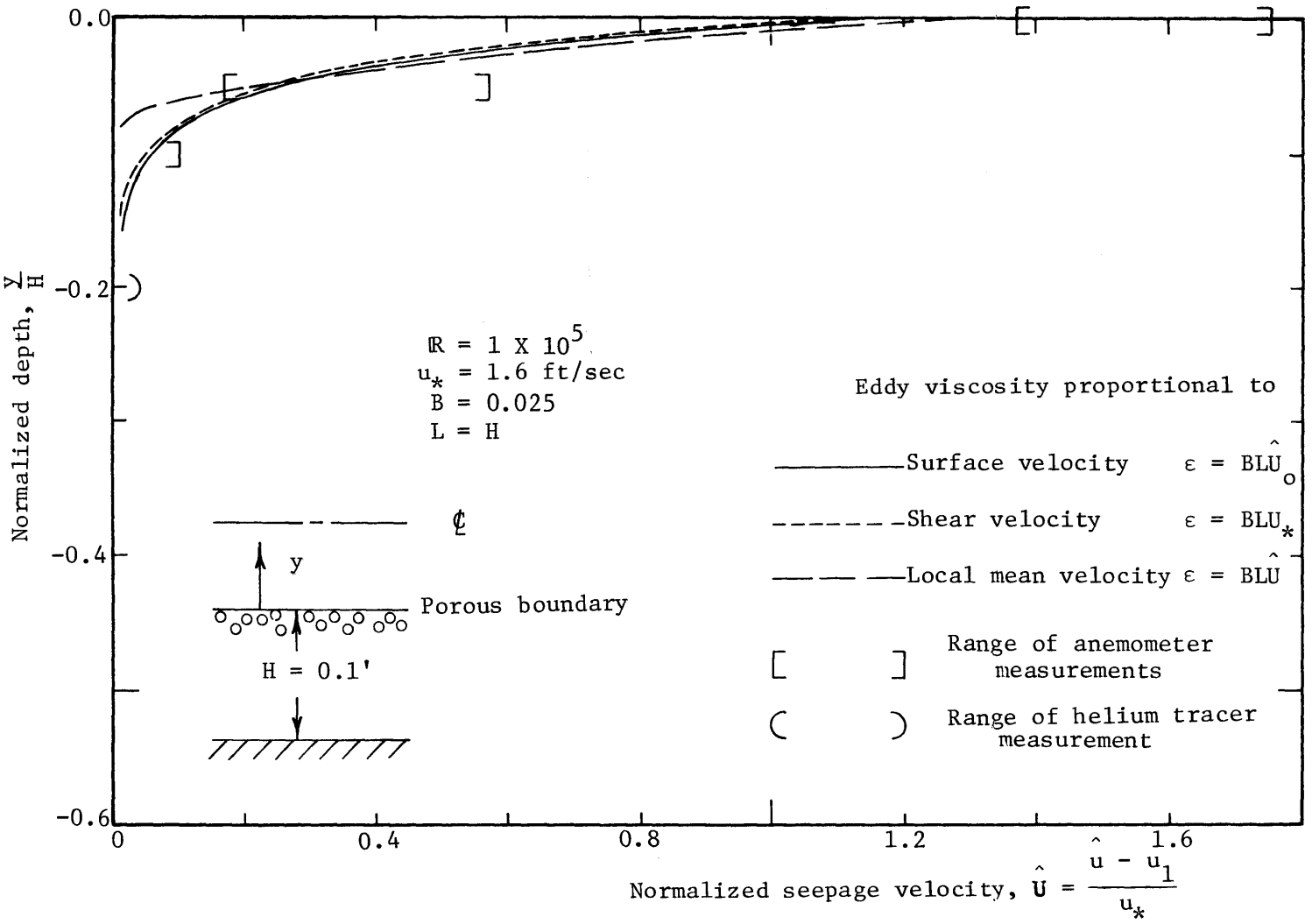

Fig. 3-14 Observed and predicted porous boundary velocity distributions, $\mathbb{R} = 1 \times 10^5$

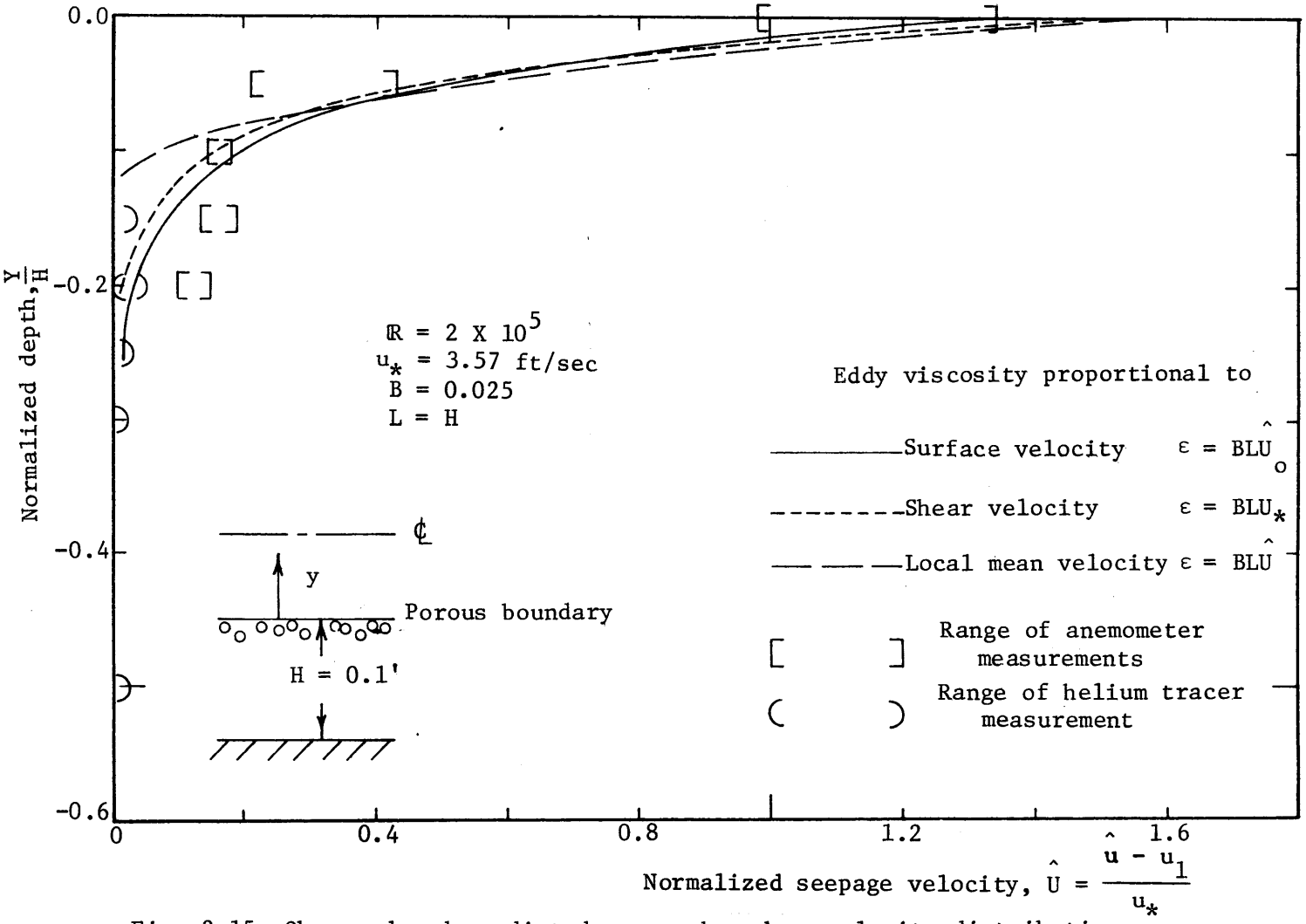

Fig. 3-15 Observed and predicted porous boundary velocity distributions, $\mathbb{R} = 2 \times 10^5$

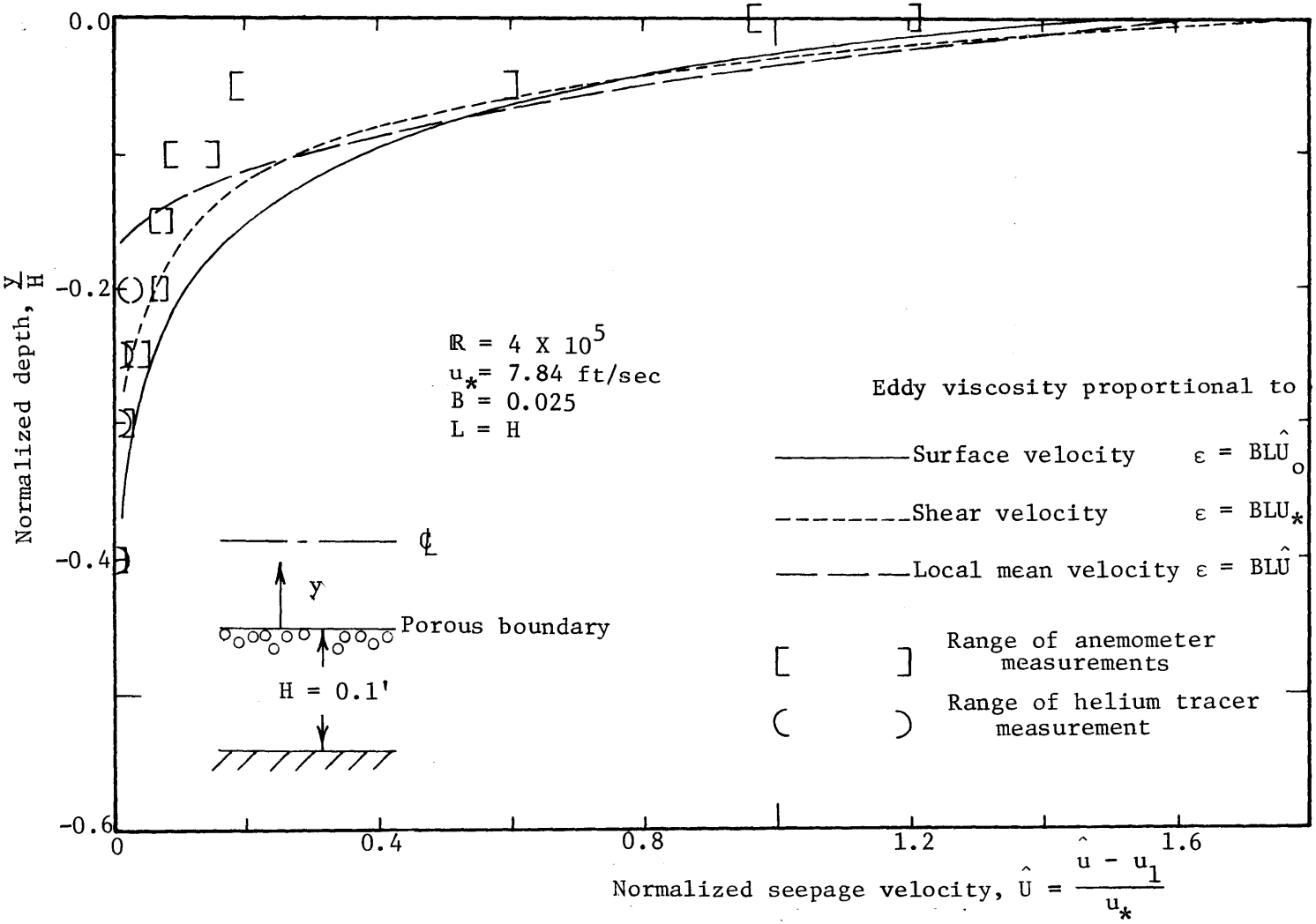

Fig. 3-16 Observed and predicted porous boundary velocity distributions, $\mathbb{R} = 4 \times 10^5$

ly free of turbulence. Thus, it is uncertain if this correlation exists when the anemometer is exposed to a flow exhibiting a velocity gradient and a high degree of turbulence which characterizes the flow near the surface at the high Reynolds number.

Until the velocity correlation can be resolved, possibly by perfecting the helium tracer technique, the velocity distribution predicted by the models can be considered to provide a reasonable representation of the actual seepage velocity in the porous foam boundary. The choice of the mathematical model to use is somewhat arbitrary. All three models give distributions which are reasonably close to those measured. The exact location of the penetration depth cannot be specified from the velocity measurements, but if the turbulent intensities shown in Fig. 2-32 of Chapter 2 are considered it appears that the penetration depth is somewhat between $-0.2 > Y/H > -0.3$. If this is true, then the constant eddy viscosity models would be preferred since they indicate comparable penetration depths.

3.6 Analysis of Core Flow

In this section the relationship between the core flow and the boundary flow is developed. The linking of the two flow fields is through the slip velocity and the eddy viscosity at the boundary. After establishing the velocity distribution in the core, it is possible to find an expression relating the friction factor, f, to the permeability Reynolds number, $\mathbb{R}_k$. Then, given a value of f at some $\mathbb{R}_k$, an approximation is used to provide a method of estimating the change in friction factor with Reynolds number. It was hoped that the

friction factor relationship would provide some insight into the interaction of the two flow fields.

In the porous pipe, it is assumed that fully-developed steady flow exists. The shear stress in the core, τ, varies linearly with the radical distance from the pipe centerline, r, and can be given by

$$\frac{\tau}{\tau_o} = \frac{r}{R} \tag{3-58}$$

where

R = radius to porous boundary

τ_o = shear stress at r = R

Using the eddy viscosity concept the shear stress is expressed as

$$\tau = \rho\varepsilon \frac{du}{dy} \tag{3-59}$$

Phenomenological theories give various functional relationships for the form of the eddy viscosity. Generally, these have assumed that the wall or boundary was impermeable and the eddy viscosity approached zero at the wall. Muñoz found that by assuming an origin below the surface of the porous boundary, he could arrive at an eddy viscosity that could be used over the entire pipe core. This is similar to the approach Rotta (1950) used in his analysis of effects of roughness on velocity distributions in turbulent flow.

Using Muñoz's findings that the velocity defect could be interpreted with the shifted coordinate system, the following form for the eddy viscosity was assumed to completely specify Eq. (3-59)

$$\varepsilon = \kappa u_* y' \left(1 - \frac{y}{R}\right) \tag{3-60}$$

where

κ = 0.4 (Karman's constant) and the coordinates y' and y are defined in the

sketch of Fig. 3-17 . Combining Eqs. (3-58), (3-59) and (3-60) gives

$$\rho\kappa u_* \, y' \frac{dU}{dy} = \tau_o \tag{3-61}$$

Noting that dy = dy' and using the definition

$$\tau_o = \rho u_*^2 \tag{3-62}$$

Eq. (3-61) can be written as

$$y' \frac{du}{dy'} = \frac{u_*}{\kappa} \tag{3-63}$$

Integrating Eq. (3-63) gives

$$u = \frac{u_*}{\kappa} \ln y' + c' \tag{3-64}$$

The constant, c', can be evaluated using a boundary condition based on the surface velocity.

Murray (1965) developed a boundary condition when analyzing waves over a permeable bed similar to that of the porous pipe. His boundary condition would imply that the core velocity is equal to the seepage velocity at the boundary. This condition is used in the analysis of the core flow. It is assumed here that the velocity distribution in the porous boundary is known and, thus, the value of the surface velocity can be determined. For the core the surface velocity is designated by u_o. The boundary condition necessary to evaluate c' can now be written as

$$u = u_o \quad \text{at} \quad y' = \delta \tag{3-65}$$

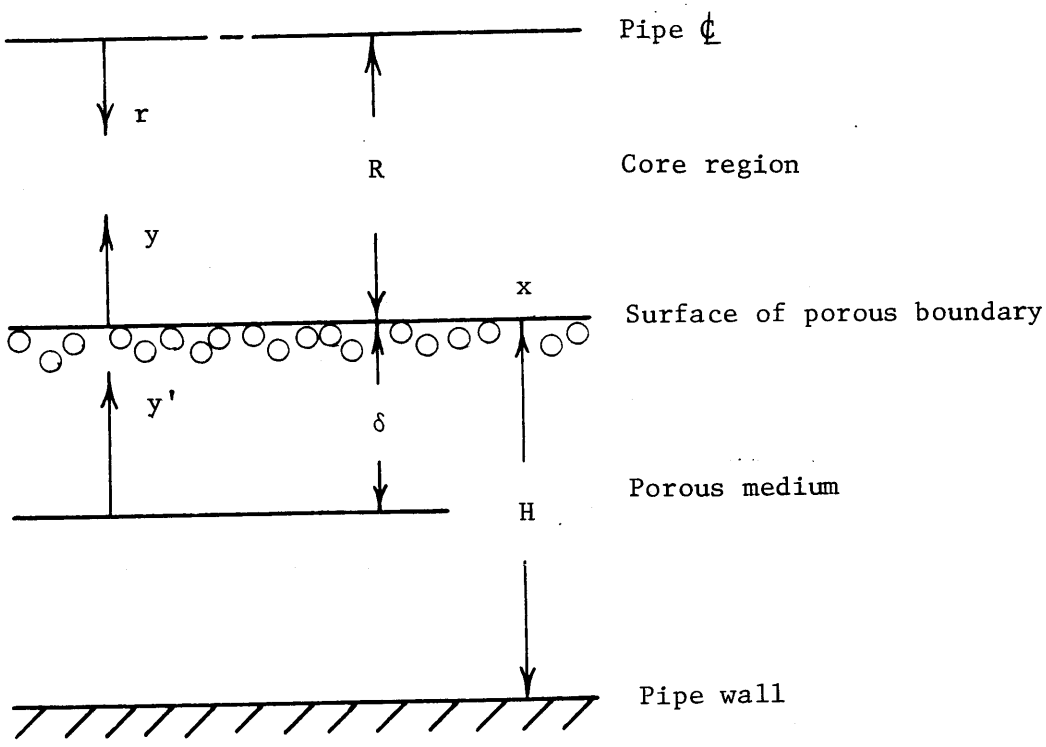

Fig. 3-17 Coordinate system used in core flow analysis

Evaluating c' and substituting for it in Eq. (3-64) results in the equation for the velocity distribution in the core, which is

$$U - U_o = \frac{1}{\kappa} \ln (y'/\delta) \tag{3-66}$$

where

$$U = u/u_* \tag{3-67}$$

$$U_o = u_o/u_* \tag{3-68}$$

The above equation can be evaluated if the δ can be determined. This is accomplished through the eddy viscosity as will be shown.

Corresponding to U_o in the core is the velocity determined by the porous medium models which is

$$\hat{U}_o = U_o - U_1 \tag{3-69}$$

Using the relationship for the velocities, Eq. (3-69), the value of δ can now be found by equating the eddy viscosities of the core and porous medium models, evaluated at the interface.

The eddy viscosity at the interface is not the same for the three porous medium models. For the two models, $\varepsilon = BL\hat{U}$ and $\varepsilon = BL\hat{U}_o$, the interface eddy viscosity can be designated as

$$\frac{\varepsilon}{u_*} = BL\hat{U}_o \tag{3-70}$$

Equating Eq. (3-70) to the value of the core eddy viscosity, Eq. (3-60), evaluated at $y' = \delta$ gives

$$\delta = \frac{BL}{\kappa} \hat{U}_o \tag{3-71}$$

If the model using $\varepsilon = BLU_*$ is considered, the equation corresponding to Eq. (3-70) would be

$$\frac{\varepsilon}{u_*} = BL \tag{3-72}$$

Then, the value of the shift in the coordinate, δ, would become

$$\delta = \frac{BL}{\kappa} \tag{3-73}$$

By equating the eddy viscosities an additional restriction is imposed on the problem. This condition is that the slope of the velocity profiles at the boundary must be continuous in order to keep the shear stress across the boundary continuous.

The average normalized velocity, $\overline{U}$, in the pipe can be determined if the discharge in the boundary can be neglected. Muñoz found the boundary flow to be insignificant compared with the core flow when he compared the measured total discharge with that found by integrating his experimentally determined core velocity profile. Therefore, the assumption seems warranted. Integrating the velocity over the pipe core and dividing by the area gives

$$\overline{U} - U_o = \frac{1}{\kappa}\left\{-\frac{3}{2} - \frac{\delta}{R} + \left(\frac{R+\delta}{R}\right)^2 \ln\left(\frac{R+\delta}{\delta}\right)\right\} \tag{3-74}$$

The definition of friction factor for a pipe can be written as

$$\overline{U} = \frac{\overline{u}}{u_*} = \sqrt{\frac{8}{f}} \tag{3-75}$$

Substituting Eq. (3-75) and this expression for U_o given by Eq. (3-69)

into Eq. (3-74), the friction factor for the porous pipe can be related to characteristics of the boundary velocity distribution by

$$\sqrt{\frac{8}{f}} = \hat{U}_o + U_1 + \frac{1}{\kappa}\left\{ - \frac{3}{2} - \frac{\delta}{R} + \left(\frac{R+\delta}{R}\right)^2 \ln\left(\frac{R+\delta}{\delta}\right) \right\} \qquad (3\text{-}76)$$

The relationship between the friction factor, f, and Reynolds number cannot be seen easily from Eq. (3-76). That is because the surface velocity, U_o, depends upon the Reynolds number and the value of B as was pointed out in Sections 3.3 and 3.4. The surface velocity also depends upon the model used to evaluate it. The value of δ is dependent upon the surface velocity for two of the porous medium models as indicated by Eq. (3-71). For the other case, δ is a constant given by Eq. (3-73). The pressure gradient flow, U_1, was given by Eq. (3-20). The appearance of u_* in Eq. (3-20) makes U_1 also dependent upon the Reynolds number. Because of the complex interaction of these terms it is difficult to anticipate if the friction factor will increase or decrease with increasing Reynolds number.

The friction factor was observed by Muñoz to increase with increasing Reynolds number in his porous pipe experiments. The range of Reynolds numbers covered in his experiments was the same as covered in this study. Lovera and Kennedy (1969) have shown that the friction factor increases with Reynolds number for flow in sand bed channels. This indicates that some similarity may exist between the flow in the porous pipe and sand bed channels.

Beavers and Joseph (1967) reported a decrease in the friction factor with increasing Reynolds number for the laminar case of a Poiseuille flow over a naturally permeable block. Their experiments covered a range of Reynolds numbers, based on the channel height, from about 20 to 2000. Review of their results indicated that the friction factor reached a minimum value at a Reynolds number of about 1500. It is difficult to determine if the friction factor would have increased or become constant with increasing Reynolds numbers greater than 2000.

It is obvious from the above examples that knowledge of the friction factor - Reynolds number relationship is pertinent. Through it greater insight into the mechanism relating the core and boundary flows may be achieved.

Before proceeding, the order of magnitude of δ is estimated in order to reduce Eq. (3-76) to a more tractable form. From the experimental results of Chapter 2 the value of the normalized surface velocity can be estimated to be of order one for all the models. Likewise, the value of BL = 0.0025 ft. gave a reasonable fit for the velocity profile. Using these values,

$$\delta \simeq 0.00625 \text{ ft.}$$

and

$$\frac{\delta}{R} = 0.0159 << 1$$

Therefore, neglecting δ in comparison with R, Eq. (3-76) can be reduced to

$$\sqrt{\frac{8}{f}} = \hat{U}_o + U_1 + \frac{1}{\kappa}\left(-\frac{3}{2} + \ln\frac{R}{\delta}\right) \tag{3-77}$$

In Eq. (3-77), both $\hat{U}_o$ and U_1 are normalized with respect to the shear velocity u_*. Since the friction factor is a function of the average velocity, $\bar{u}$, it would seem appropriate that the characteristic velocity be $\bar{u}$ instead of u_*. Only the model assuming $\varepsilon = BL\hat{U}_o$ is developed here. This discussion applies to the other models also, but the equations for $\hat{U}_o$ and δ would be different.

Letting

$$\hat{V}_o = \frac{\hat{u}_o}{\bar{u}} \tag{3-78}$$

$$V_1 = \frac{u_1}{\bar{u}} \tag{3-79}$$

$$\mathbb{R}_k = \frac{u\sqrt{k}}{\nu} \tag{3-80}$$

where the permeability Reynolds number, $\mathbb{R}_k$, implies the characteristic length, $L = \sqrt{k}$, Eq. (3-77) can be written as

$$\sqrt{\frac{8}{f}}\left(1 - \hat{V}_o - V_1\right) = \frac{1}{\kappa}\left(-\frac{3}{2} + \ln\frac{R\kappa}{\sqrt{k}} - \ln\hat{V}_o - \ln\sqrt{\frac{8}{f}} - \ln B\right) \tag{3-81}$$

The surface velocity given by Eq. (3-38) can be rewritten using Eqs. (3-78), (3-79) and (3-80) as

$$\frac{1}{B}\left(\sqrt{\frac{8}{f}}\right)^{-4} = \left(\mathbb{R}_k^{-1} + \frac{2V_1}{c}\right)\hat{V}_o^{\,3} + \frac{2\hat{V}_o^{\,4}}{3c} \tag{3-82}$$

The pressure gradient flow, Eq. (3-20), can be transformed in a similar manner and written as

$$V_1 = -\frac{c}{2\mathbb{R}_k} + \frac{1}{2}\left\{\frac{c^2}{\mathbb{R}_k^2} + \frac{8c\sqrt{k}}{R}\left(\sqrt{\frac{8}{f}}\right)^{-2}\right\}^{1/2} \tag{3-83}$$

The last three equations can, in principle, be solved to find the friction factor versus Reynolds number relationship for a porous pipe if the quantities c, $\sqrt{k}$ and R are given and B is viewed as a fitting parameter. Likewise, if values of f and $\mathbb{R}_k$ are known along with c, $\sqrt{k}$ and R a value of B is implied.

Another method of estimating the change in friction factor with Reynolds number involves assuming the functional form of the relationship. The method also assumes that one point on the curve relating f and $\mathbb{R}_k$, designated the reference value, is known. A description of the method is presented in the following paragraphs. Mathematical details of the method are presented in Appendix C for the constant eddy viscosity model, $\varepsilon = B\hat{L}U_o$.

Knowing that the velocity is given by a logarithmic function, it can be expected that the Reynolds number also enters as a logarithmic function. Thus, an estimation of the change in friction factor can be made by taking some reference value, say $\left(\sqrt{\frac{8}{f}}\right)_o$, and adding to it the change, interpreted as the slope of the curve of $\sqrt{\frac{8}{f}}$ versus $\ln \mathbb{R}_k$ multiplied by the incremental change in the $\ln \mathbb{R}_k$. Mathematically, this can be written as

$$\sqrt{\frac{8}{f}} - \left(\sqrt{\frac{8}{f}}\right)_o = \frac{d(F)}{d \ln \mathbb{R}_k} \cdot \left[\ln \mathbb{R}_k - \ln\left(\mathbb{R}_k\right)_o\right] \tag{3-84}$$

where

$$F = \sqrt{\frac{8}{f}} \tag{3-85}$$

and the subscript o indicates the known reference values. The derivative, $\frac{dF}{d \ln \mathbb{R}_k}$, represents the slope of the curve of $\sqrt{\frac{8}{f}}$ versus $\ln \mathbb{R}_k$. For convenience, a dot over the variable is used to indicate the derivative with respect to $(\ln \mathbb{R}_k)$, i.e., $\dot{F} = \frac{dF}{d \ln \mathbb{R}_k}$. If the change in $(\ln \mathbb{R}_k)$ is considered to be positive, the slope must be negative in order for the friction factor to increase with increasing Reynolds number.

Evaluation of the derivative requires differentiating Eqs. (3-81), (3-82) and (3-83) with respect to $(\ln \mathbb{R}_k)$. The resulting three equations are sufficient to evaluate $\dot{F}$ in terms of the reference values, $\left(\sqrt{\frac{8}{f}}\right)_o$ and $(\ln \mathbb{R}_k)_o$, and the quantities $\hat{V}_o$, V_1, and B. The friction factor at another $\mathbb{R}_k$ now can be estimated by using Eq. (3-84).

The slope, $\dot{F}$, was evaluated for the three eddy viscosity models by taking a value from the curve of f versus $\mathbb{R}$ presented by Muñoz. An intermediate value of f = 0.06 at $\mathbb{R}_k$ = 160 was chosen. Table 3-1 gives the values F, B and the value of $\hat{U}_o$ corresponding to B determined at $\mathbb{R}_k$ = 160. The value of $\dot{F}$ was then used to determine values of f at $\mathbb{R}_k$ = 80 and $\mathbb{R}_k$ = 320. The resulting values of f for the three models are compared with observed values of f in Fig. 3-18.

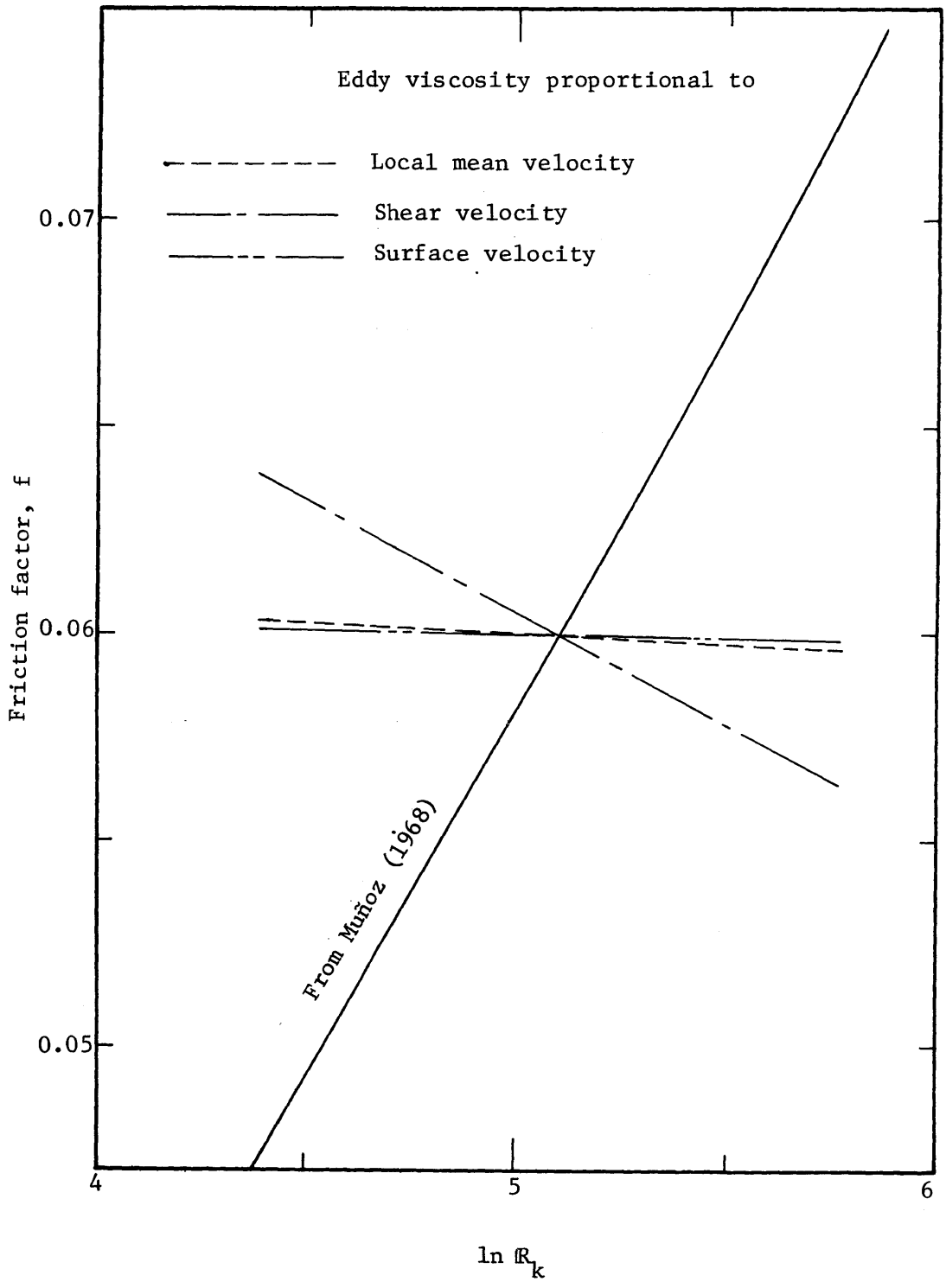

Fig. 3-18 Observed and predicted values of friction factor

Table 3-1

Values of the slope, $\dot{F}$, $\hat{U}_o$, and B determined at $\mathbb{R}_k = 160$

Eddy Viscosity Model	$\varepsilon = BL\hat{U}_o$	$\varepsilon = BLU_*$	$\varepsilon = BL\hat{U}$
B[†]	0.00387	0.00169	0.00380
$\dot{F}$	0.0201	0.5168	0.0489
$\hat{U}_o$	2.42	4.59	2.68

[†] A value of L = H = 0.1 ft. corresponds to this value of B.

In all cases, the value of $\dot{F}$ was found to be positive. Corresponding to this, the three models predicted a friction factor that decreased with increasing values of Reynolds number. All of the values of B given in Table 3-1 are lower than the value of B = 0.025 found to give the best-fitting velocity profile in Chapter 2. Corresponding to B, the value of $\hat{U}_o$ given in Table 3-1 is higher than observed.

The two factors involved in determining the friction factor are $\hat{U}_o$ and δ according to Eq. (3-77). For the model, $\varepsilon = BLU_*$, δ is a constant and does not change with Reynolds number. For the other two models, δ depends on $\hat{U}_o$. The slip velocity, $\hat{U}_o$, and δ have opposite effects on the friction factor. The direct effect of $\hat{U}_o$ is to decrease the friction factor with increasing Reynolds number. The effect of δ

is to increase the friction factor with increasing Reynolds number. In the range of values of $\hat{U}_o$ considered in this analysis, the effect of δ is small compared with the effect of $\hat{U}_o$ because the friction factor increase due to δ is logarithmic whereas the decrease due directly to $\hat{U}_o$ is linear. It can be seen from Fig. 3-18 that model, $\varepsilon = BL\hat{U}_o$, has the least decrease in the friction factor with Reynolds number. This is the model which also predicts the greatest penetration depth. All of the models predict an increase in $\hat{U}_o$ with increasing Reynolds number for a given value of B, but the $\varepsilon = BL\hat{U}_o$ model has the smallest increase.

Apparently, in the core flow model, the shear effects reflected in δ are relatively insignificant compared with the slip velocity effect. It is also possible that the shear effects modeled here are not the primary factor determining the interaction between the core and boundary flows.

Obviously, the core flow model does not provide an adequate prediction of the friction factor. However, the boundary flow models do provide a reasonable representation of the experimental velocity profiles using one empirically determined parameter, B.

IV. DISPERSION IN A SHEAR FLOW

4.1 Introduction

This analysis of dispersion in a shear flow was developed in an effort to assessthe limitations of the helium tracer technique of velocity measurements in a shear flow. A perturbation technique is used to solve the dispersion equation describing the distribution of helium in the porous medium shear flow. Solutions are developed for constant and velocity dependent dispersion coefficients.

The solution with the variable coefficients is thought to reflect more correctly the conditions within the porous medium, but the range of application is difficult to define specifically. However, the solution for the constant coefficients case can be compared with a known exact solution for diffusion in a shear flow. Thus, comparison of these two solutions gives an indirect method of defining the limitations of the variable coefficient solution.

The mathematical model describing the dispersion process is presented first. Then, the perturbation solution for constant coefficients of dispersion will be derived, followed by the solution for variable coefficients. The perturbation solution and the exact solution are compared. The comparison is extended to the variable coefficient solution and its apparent limitations are defined. Characteristics of the solutions are discussed along with application of the results to others environments.

4.2 Mathematical Model

In a binary system, application of the conservation of mass principle results in the classical convective-diffusion equation. The

analysis of dispersion in a shear flow is based on the convective-diffusion equation. Crank (1956) and Daily and Harleman (1966) give a detailed development of the equation. Since the process of transporting the tracer is one due to variations of the velocity, the term dispersion will replace diffusion throughout the rest of this discussion as suggested by Hoopes (1969) and Harleman (1970).

The general equation for turbulent convective dispersion for a mass flux in the x-direction is given by Daily and Harleman as

$$\frac{\partial \bar{c}_A}{\partial t} + \bar{u}\frac{\partial \bar{c}_A}{\partial x} + \bar{v}\frac{\partial \bar{c}_A}{\partial y} + \bar{w}\frac{\partial \bar{c}_A}{\partial z} = \frac{\partial}{\partial z}\left(E_x \frac{\partial \bar{c}_A}{\partial x}\right) + \frac{\partial}{\partial y}\left(E_y \frac{\partial \bar{c}_A}{\partial y}\right) + \frac{\partial}{\partial z}\left(E_z \frac{\partial \bar{c}_A}{\partial z}\right) + D_{AB}\left(\frac{\partial^2 \bar{c}_A}{\partial x^2} + \frac{\partial^2 \bar{c}_A}{\partial y^2} + \frac{\partial^2 \bar{c}_A}{\partial z^2}\right) \qquad (4\text{-}1)$$

where:

$\bar{c}_A$ = concentration of component A in a mixture of species A and B and is defined as $\frac{\text{mass of A}}{\text{mass of mixture of A and B}}$

t = time

$\bar{u}$, $\bar{v}$ and $\bar{w}$ = mean velocities in the coordinate directions x, y, and z, respectively.

D_{AB} = molecular-diffusion coefficient

E_x, E_y, E_z = turbulent-dispersion coefficients defined as

$$\rho\overline{(c'u')} = -\rho E_x \frac{\partial c_A}{\partial x}, \quad \rho\overline{(c'v')} = -\rho E_y \frac{\partial c_A}{\partial y}, \text{ and}$$

$$\rho\overline{(c'w')} = -\rho E_z \frac{\partial c_A}{\partial y} \qquad (4\text{-}2)$$

where the prime denotes the fluctuating component of the quantity and the bar reflects the time average of the fluctuating components.

The proposed mathematical model considers dispersion in a shear flow. A sketch of the model is given in Fig. 4-1. The characteristics of the system are described as follows

a) The porous medium is homogeneous and extends to infinity in all directions.

b) The mean velocity is steady and uniform and is taken in the x-direction. Effects of curvature of the pipe are neglected.

c) The dispersion coefficients are assumed to be directly proportional to the velocity. Molecular diffusion is neglected.

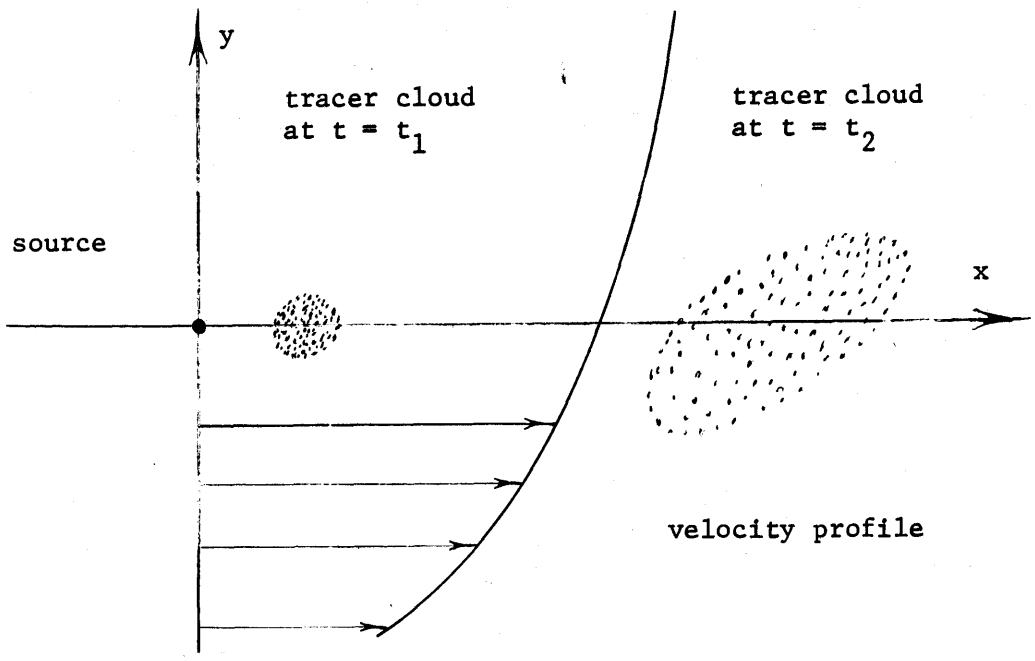

Fig. 4.1 Sketch of Dispersion in a Shear Flow

Harleman, Mehlhorn, and Rumer (1962) have shown that for laminar flow, the longitudinal dispersion coefficient was approximately proportional to the velocity. Hoopes and Harleman (1965) showed that the lateral dispersion, E_2, was proportional to the permeability Reynolds number, R_k, raised to a power, n, $E_2 \propto R_k^n$ for $R_k < 0.4$. For $R_k > 0.4$, E_2 tends to become directly proportional to R_k. Although their experimental results covered only a range of velocities for $R_k < 10$, the trend in the data seems to indicate a linear dependence of the dispersion coefficients on the velocity for values of $R_k > 10$. Furthermore, for mathematical convenience they introduced dispersion coefficients into their mathematical model which were directly proportional to the velocity.

Permeability Reynolds numbers are expected to be very much greater than 10 in the porous pipe. Therefore, following the trend shown, the dispersion coefficients were assumed to be directly related to the velocity. The lateral dispersion coefficients were assumed to be equal. These assumptions can be written as

$$E_x = E_1 = \alpha_1 u \tag{4-3}$$

$$E_y = E_z = E_2 = E_3 = \alpha_2 u \tag{4-4}$$

where α_1 and α_2 are dispersivity coefficients with dimensions of length.

Substituting Eqs. (4-3) and (4-4) into Eq. (4-1) gives the following equation. (The subscript A and the bar denoting the time average

concentration are dropped as a matter of convenience).

$$\frac{\partial c}{\partial t} + u \frac{\partial c}{\partial x} = \frac{\partial}{\partial x}\left(\alpha_1 u \frac{\partial c}{\partial x}\right) + \frac{\partial}{\partial y}\left(\alpha_2 u \frac{\partial c}{\partial y}\right) + \frac{\partial}{\partial z}\left(\alpha_2 u \frac{\partial c}{\partial z}\right) \quad (4\text{-}5)$$

Equation (4-5) is the basic equation for the mathematical model in which the dispersion coefficients are proportional to the velocity.

Later in this chapter the solution of this equation is compared with the exact solution for a diffusion process when the coefficients are assumed to be constants. Therefore, as an intermediate step in the comparison, the perturbation solution for the case where the dispersion coefficients are assumed constant was found. Following equations (4-3) and (4-4), the form of the dispersion coefficients was taken as

$$E_{10} = \alpha_1 u_o \quad (4\text{-}6)$$

$$E_{20} = \alpha_2 u_o \quad (4\text{-}7)$$

where u_o = a characteristic velocity.

The terms α_1 and α_2 are the same as previously defined. The equation resulting from the substitution of Eqs. (4-6) and (4-7) into Eq. (4-1) is

$$\frac{\partial c}{\partial t} + u \frac{\partial c}{\partial x} = \alpha_1 u_o \frac{\partial^2 c}{\partial x^2} + \alpha_2 u_o \frac{\partial^2 c}{\partial y^2} + \alpha_3 u_o \frac{\partial^2 c}{\partial z^2} \quad (4\text{-}8)$$

Equation (4-8) is the basic equation describing the dispersion process where the dispersion coefficients are assumed to be constants.

Equation (4-5) and (4-8) can be made non-dimensional by introducing a characteristic length, L, and a characteristic velocity, u_o,

such that

$$x = Lx', \; y = Ly', \; z = Lz' \tag{4-9}$$

$$u = u_o \, u' \tag{4-10}$$

$$t = \frac{L}{u_o} \, t' \tag{4-11}$$

where the prime in this case denotes the dimensionless quantity. Upon substitution of the above equations into (4-5), (dropping the primes as a matter of convenience and noting that the quantities are dimensionless), the result is

$$\frac{\partial c}{\partial t} + u \frac{\partial c}{\partial x} = \frac{1}{P_1} \frac{\partial}{\partial x}\left(u \frac{\partial c}{\partial x}\right) + \frac{1}{P_2} \frac{\partial}{\partial y} \left(u \frac{\partial c}{\partial y}\right) + \frac{1}{P_2} \frac{\partial}{\partial z}\left(u \frac{\partial c}{\partial y}\right) \tag{4-12}$$

$$\text{where } P_1 = \frac{L}{\alpha_1}, \; P_2 = \frac{L}{\alpha_2} \tag{4-13}$$

This is the non-dimensional equation for the mathematical model with the assumption of dispersion coefficients proportional to velocity.

Substituting Eqs. (4-9), (4-10), and (4-11) into Eq. (4-8) gives the nondimensional equation for the mathematical model with constant coefficients of dispersion. Upon substitution, it becomes

$$\frac{\partial c}{\partial t} + u \frac{\partial c}{\partial x} = \frac{1}{P_1} \frac{\partial^2 c}{\partial x^2} + \frac{1}{P_2} \frac{\partial^2 c}{\partial y^2} + \frac{1}{P_2} \frac{\partial^2 c}{\partial z^2} \tag{4-14}$$

The solutions of Eqs. (4-12) and (4-14) depend upon the initial and boundary conditions imposed on the system. In this model, the initial condition imposed was that of an instantaneous point source introduced into the system at time, t = 0. It was located at the originof the coordinate system. Mathematically, this can be represented

by:

$$c = c(x,y,z,0) = (M/\rho)\delta(x)\ \delta(y)\ \delta(z) \tag{4-15}$$

where $M = \int_{-\infty}^{\infty}\int\int c\rho\ dydxdz$ is the mass of tracer introduced at $x = 0$, $y = 0$, $z = 0$ and $t = 0$.

ρ = the density of the tracer

$\delta(\gamma)$ = the Dirac delta function of the variable γ.

The boundary condition appropriate for an instantaneous point source is

$$c \to o \quad \text{as } x^2 + y^2 + z^2 \to \infty, \text{ for all } t \tag{4-16}$$

Using the initial and boundary conditions above, solutions to Eqs. (4-12) and (4-14) can be found using a perturbation technique. The technique and solutions are given in the following sections.

4.3 Perturbation Solution of the Dispersion Equation with Constant Coefficients

In order to find the solution to Eq. (4-14) subject to the initial and boundary conditions, Eqs. (4-15) and (4-16), the following transformation is introduced:

$$\xi = x - ut \tag{4-17}$$

With this change of variable, Eq. (4-14) becomes

$$\frac{\partial c}{\partial t} = \frac{1}{P_1}\frac{\partial^2 c}{\partial \xi 2} + \frac{1}{P_2}\left(\frac{\partial}{\partial y} - t\frac{\partial u}{\partial y}\frac{\partial}{\partial \xi}\right)\left(\frac{\partial c}{\partial y} - t\frac{\partial u}{\partial y}\frac{\partial c}{\partial \xi}\right) + \frac{1}{P_2}\frac{\partial^2 c}{\partial z^2} \tag{4-18}$$

If the concentration and velocity are assumed to be continuous functions, Eq. (4-18) can be written as

$$\frac{\partial c}{\partial t} = \frac{1}{P_1}\frac{\partial^2 c}{\partial \xi^2} + \frac{1}{P_2}\frac{\partial^2 c}{\partial y^2} + \frac{1}{P_2}\frac{\partial^2 c}{\partial z^2} - \frac{t}{P_2}\frac{\partial c}{\partial \xi}\frac{\partial^2 u}{\partial y^2} - 2\frac{t}{P_2}\frac{\partial u}{\partial y}\frac{\partial^2 c}{\partial \xi \partial y}$$

$$+ \frac{t^2}{P_2}\left(\frac{\partial u}{\partial y}\right)^2 \frac{\partial^2 c}{\partial \xi^2} \qquad (4\text{-}19)$$

Another transformation is introduced which scales the coordinates relative to their respective dispersion coefficients. The coordinate transformations are:

$$X = \xi\sqrt{P_1} \qquad (4\text{-}20)$$

$$Y = y\sqrt{P_2} \qquad (4\text{-}21)$$

$$Z = z\sqrt{P_2} \qquad (4\text{-}22)$$

Substituting these into Eq. (4-19)

$$\frac{\partial c}{\partial t} = \frac{\partial^2 c}{\partial X^2} + \frac{\partial^2 c}{\partial Y^2} + \frac{\partial^2 c}{\partial Z^2} - t\sqrt{P_1}\frac{\partial c}{\partial X}\frac{\partial^2 u}{\partial Y^2} - 2t\sqrt{P_1}\frac{\partial u}{\partial Y}\frac{\partial^2 c}{\partial X \partial Y}$$

$$+ t^2 P_1\left(\frac{\partial u}{\partial y}\right)^2 \frac{\partial^2 c}{\partial X^2} \qquad (4\text{-}23)$$

A solution for Eq. (4-23) based on a perturbation procedure can be found by expanding the solution and the defining equation in terms of a small parameter, ε. To do this, the velocity, u, and the concentration, c, are expanded as follows:

$$u = 1 + \varepsilon f_1 + \varepsilon^2 f_2 + \ldots. \qquad (4\text{-}24)$$

where f_1, f_2,... are functions of y, and

$$c = c_o + \varepsilon c_1 + \varepsilon^2 c_2 + \ldots . \tag{4-25}$$

The resulting equation upon substitution of Eqs. (4-24) and (4-25) into Eq. (4-23) and rearranging is

$$\frac{\partial c_o}{\partial t} - \nabla^2 c_o + \varepsilon \frac{\partial c_1}{\partial t} - \nabla^2 c_1 + t\sqrt{P_1} \frac{\partial c_o}{\partial X} \frac{\partial^2 f_1}{\partial Y^2} + 2t\sqrt{P_1} \frac{\partial f_1}{\partial Y} \frac{\partial^2 c_o}{\partial X \partial Y}$$
$$+ \varepsilon^2 \frac{\partial^2 c_2}{\partial t} - \nabla^2 c_2 + t\sqrt{P_1} \frac{\partial c_o}{\partial X} \frac{\partial^2 f}{\partial Y^2} + \frac{\partial c_1}{\partial X} \frac{\partial^2 f_1}{\partial Y^2}$$
$$+ 2t\sqrt{P_1} \frac{\partial f_2}{\partial Y} \frac{\partial^2 c_o}{\partial X \partial Y} + \frac{\partial f_1}{\partial Y} \frac{\partial^2 c_1}{\partial X \partial Y} - t^2 P_1 \frac{\partial f_1}{\partial Y}^2 \frac{\partial^2 c_o}{\partial X^2} + O(\varepsilon^3) = 0 \tag{4-26}$$

where $\nabla^2 = \frac{\partial^2}{\partial X^2} + \frac{\partial^2}{\partial Y^2} + \frac{\partial^2}{\partial Z^2}$ (4-27)

and $O(\varepsilon^3)$ means order of ε^3.

Some assumptions concerning the velocity and the initial condition are introduced here before expanding Eq. (4-26) and grouping the coefficients of the powers of ε. Any velocity profile can be represented by a linear profile for a limited distance within the neighborhood of the point of interest. This distance will depend upon the curvature of the velocity profile. In this model the velocity in the region of interest is assumed to have a linear profile which can be represented by

$$u = 1 + sy = 1 + s \frac{Y}{\sqrt{P_1}} \tag{4-28}$$

where s = the slope of the nondimensional velocity profile and $f_1 = y$.

If the series expansion of the concentration is introduced in the initial condition of equation (4-15), the mass of tracer, M, must be expanded as

$$M = M_o + \varepsilon M_1 + \varepsilon^2 M_2 + \ldots . \tag{4-29}$$

To solve the zero order equations, the initial condition is taken as

$$M = M_o \tag{4-30}$$

This condition implies that in order to conserve the mass, no additional mass can be injected. Therefore, the initial conditions for the higher order equations become

$$M_1 = M_2 = M_3 = \ldots = 0 \text{ at } t = 0 \tag{4-31}$$

Grouping the coefficient equations for the orders of ε from Eqs. (4-15), (4-16) and (4-26) with the substitution of Eq. (4-28) gives for the zero, first and second orders:

ε^o coefficients

$$\left.\begin{aligned} &\frac{\partial c_o}{\partial t} - \nabla^2 c_o = 0 \\ &c_o = \frac{(M_o/\rho)}{\sqrt{P_1 P_2 L^3}} \quad \delta(X)\ \delta(Y)\ \delta(Z) \quad \text{at } t = 0 \end{aligned}\right\} \tag{4-32}$$

where

$$M_o = \int_{-\infty}^{\infty}\int\int \frac{c_o \rho L^3}{\sqrt{P_1}\, P_2}\, dX\, dY\, dZ$$

$$c_o \to 0 \quad \text{as } X^2 + Y^2 + Z^2 \to \infty \text{ for all } t \qquad \Big\} \tag{4-32}$$

ε^1 coefficients:

$$\left.\begin{aligned} &\frac{\partial c_1}{\partial t} - \nabla^2 c_1 = -2t \, \frac{P_1}{P_2} \, \frac{\partial^2 c_o}{\partial X \partial Y} \\ &M_1 = \int_{-\infty}^{\infty}\int_{-\infty}^{\infty}\int_{-\infty}^{\infty} \frac{c_1 \rho L^3}{\sqrt{P_1}\, P_2} \, dX \, dY \, dZ = 0 \text{ at } t = 0 \\ &c_1 \to 0 \quad \text{as } X^2 + Y^2 + Z^2 \to \infty \text{ for all } t \end{aligned}\right\} \tag{4-33}$$

ε^2 coefficients:

$$\left.\begin{aligned} &\frac{\partial c_2}{\partial t} - \nabla^2 c_2 = -2t \, \frac{P_1}{P_2} \, \frac{\partial^2 c_1}{\partial X \partial Y} + t^2 \, \frac{P_1}{P_2} \, \frac{\partial^2 c_o}{\partial X^2} \\ &M_2 = \int_{-\infty}^{\infty}\int_{-\infty}^{\infty}\int_{-\infty}^{\infty} \frac{c_2 \rho L^3}{\sqrt{P_1}\, P_2} \, dX \, dY \, dZ = 0 \text{ at } t = 0 \\ &c_2 \to 0 \text{ at } X^2 + Y^2 + Z^2 \to \infty \text{ for all } t \end{aligned}\right\} \tag{4-34}$$

The solution of an equation of the form of Eq. (4-32) has been given by Carslaw and Jaeger (1959) and in terms of the variables used here it is

$$c_o = \frac{A}{t^{3/2}} \exp\left\{ -\frac{1}{4t}\left(X^2 + Y^2 + Z^2 \right) \right\} \tag{4-35}$$

where

$$A = \frac{(M_o/\rho)\ \sqrt{P_1}\ P_2}{8\ \pi^{3/2}\ L^3} \tag{4-36}$$

Substituting Eq. (4-35) into the first order equation gives the result

$$\frac{\partial c_1}{\partial t} - \nabla^2 c_1 = -\sqrt{\frac{P_1}{P_2}}\ \frac{AXY}{2t^{5/2}}\ \exp\left\{-\frac{1}{4t}\ (X^2 + Y^2 + Z^2)\right\} \tag{4-37}$$

In theory, the solution of Eq. (4-37) can be found by taking the Fourier transform of the equation, or since the unit impulse response solution, Eq. (4-35), is known, by using the convolution integral. These methods sometimes involve integral solutions that are difficult to determine. When this happens other less formal methods may be used such as in this case.

The solution of Eq. (4-37) was found by following a procedure outlined by Wylie (1951) for linear ordinary differential equations known as the method of undetermined coefficients. The method involves assuming trial functions and substituting them into the differential equation. Proper values of one or more unknown coefficients which are included in the trial functions are finally determined so that the trial function or functions are actually a solution to the equation. The solution to the first order, Eq. (4-33) determined in this manner is

$$c_1 = -\frac{XY}{4}\sqrt{\frac{P_1}{P_2}}\ \ c_o \tag{4-38}$$

This solution provides a correction to the zero order equation and the

concentration now becomes

$$c = c_o + \varepsilon c_1 = c_o \left(1 - s \frac{XY}{4} \sqrt{\frac{P_1}{P_2}} \right) \tag{4-39}$$

Substituting Eqs. (4-35) and (4-38) into Eq. (4-34) gives the second order differential equation

$$\frac{\partial c_2}{\partial t} - \nabla^2 c_2 = \frac{P_1}{P_2} c_o \left(\frac{X^2 Y^2}{8t} - \frac{Y^2}{4} \right) \tag{4-40}$$

The solution of Eq. (4-40) is

$$c_2 = c_o \frac{P_1}{P_2} \left(- \frac{X^2 Y^2}{48} - \frac{X^2 t}{84} - \frac{Y^2 t}{12} - \frac{2t}{21} \right) \tag{4-41}$$

This solution gives a second order correction term for the mass which is

$$M_2 = - M_o \frac{P_1}{P_2} \left(\frac{t^2}{24} + \frac{2t}{12} + \frac{t}{84} + \frac{2t}{21} \right) \tag{4-42}$$

Although the initial condition $M_2 = 0$ at $t = 0$ is satisfied, a reduction in the amount of mass injected is indicated by Eq. (4-46) since t is always a positive quantity. However, this condition may be necessary in order for the perturbation solution to converge to the exact solution. That this is indeed the case will be evident in the comparison of the perturbation solution and the exact solution presented later in this chapter.

The total concentration is given by

$$c = c_o \left\{ 1 - \frac{sXY}{4} \sqrt{\frac{P_1}{P_2}} - s^2 \frac{P_1}{P_2} \left(\frac{X^2 Y^2}{48} + \frac{X^2 t}{84} + \frac{Y^2 t}{12} + \frac{2t}{21} \right) \right\} \tag{4-43}$$

This equation is correct to the second order in ε. Higher order terms would require considerably more algebraic endeavor but could be found by the same technique.

4.4 Perturbation Solution of the Dispersion with Variable Coefficients

The same transformationsas those made in solving the dispersion equation with constant coefficients are used in developing this solution. Therefore, the development will start with the substitution of Eq. (4-17) into Eq. (4-12) resulting in

$$\frac{\partial c}{\partial t} = \frac{1}{P_1} \frac{\partial}{\partial \xi}\left(u \frac{\partial c}{\partial \xi}\right) + \frac{1}{P_2}\left(\frac{\partial}{\partial y} - t \frac{\partial u}{\partial y} \frac{\partial}{\partial \xi}\right)\left(u \frac{\partial c}{\partial y} - tu \frac{\partial u}{\partial y} \frac{\partial c}{\partial \xi}\right) + \frac{1}{P_2} \frac{\partial}{\partial z}\left(u \frac{\partial u}{\partial z}\right) \tag{4-44}$$

Introducing the stretched coordinates, Eqs. (4-20), (4-21) and (4-22), into Eq. (4-44) gives

$$\frac{\partial c}{\partial t} = \frac{\partial}{\partial X}\left(u \frac{\partial c}{\partial X}\right) + \frac{\partial}{\partial Y}\left(u \frac{\partial c}{\partial Y}\right) + \frac{\partial}{\partial Z}\left(u \frac{\partial c}{\partial Z}\right) - \sqrt{P_1}\, t \frac{\partial}{\partial Y}\left(u \frac{\partial u}{\partial Y} \frac{\partial c}{\partial X}\right)$$
$$- \sqrt{P_1}\, t \frac{\partial u}{\partial Y} \frac{\partial}{\partial X}\left(u \frac{\partial c}{\partial Y}\right) + P_1\, t \frac{\partial u}{\partial Y} \frac{\partial}{\partial X}\left(ut \frac{\partial u}{\partial Y} \frac{\partial c}{\partial X}\right) \tag{4-45}$$

The expansions of the velocity, Eq. (4-24), and the concentration, Eq. (4-25), are substituted into Eq. (4-44) and upon rearranging gives

$$\frac{\partial c_o}{\partial t} - \nabla^2 c_o + \varepsilon\left\{\frac{c_1}{t} - \nabla^2 c_1 - f_1 \frac{\partial c_o}{\partial t} - f_1' \frac{\partial c_o}{\partial Y} + 2t\sqrt{\frac{P_1}{P_2}}\, f_1' \frac{\partial^2 c_o}{\partial X \partial Y}\right\}$$
$$+ \varepsilon^2\left\{\frac{\partial c_2}{\partial t} - \nabla^2 c_2 - f_1 \frac{\partial c_1}{\partial t} - f_1' \frac{\partial c_1}{\partial Y} - f_2 \frac{\partial c_o}{\partial t} - f_2' \frac{\partial c_o}{\partial Y}\right.$$
$$\left. + \sqrt{\frac{P_1}{P_2}}\, t\,(f_1 f_1' + f_2) \cdot \left(\frac{\partial^2 c_o}{\partial X \partial Y} + \frac{\partial c_o}{\partial X}\right) - \sqrt{\frac{P_1}{P_2}}\, t\, f_1' \left(\frac{\partial^2 c_1}{\partial X \partial Y} + \frac{\partial c_1}{\partial X}\right)\right.$$

$$- \frac{P_1}{P_2} t^2 (f_1')^2 \frac{\partial^2 c_o}{\partial X^2} \Bigg\} + O(\varepsilon^3) = 0 \qquad (4\text{-}46)$$

where the prime denotes differentiation with respect to y, i.e., $\frac{\partial}{\partial y}$.

The same initial and boundary conditions as those used for the solution involving constant coefficients are considered in developing this solution. Therefore, grouping the coefficient equations for the orders of ε from Eqs. (4-15), (4-16), and (4-44) with the substitution of Eq. (4-28) gives for the zero, first, and second orders:

ε^o coefficients

$$\left.\begin{aligned} &\frac{\partial c_o}{\partial t} - \nabla^2 c_o = 0 \\ &c_o = \frac{M_o/\rho}{\sqrt{P_1}\, P_2\, L^3} \quad \delta(X)\ \ \delta(Y)\ \ \delta(Z) \text{ at } t = 0 \end{aligned}\right\} \qquad (4\text{-}47)$$

where

$$M_o = \int_{-\infty}^{\infty}\int\int \frac{c_o \rho\, L^3}{\sqrt{P_1}\, P_2}\, dX\, dY\, dZ$$

$$c_o \to 0 \quad \text{as } X^2 + Y^2 + Z^2 \to \infty \text{ for all } t$$

ε^1 coefficients

$$\left.\begin{aligned} &\frac{\partial c_1}{\partial t} - \nabla^2 c_1 - \frac{Y}{\sqrt{P_2}} \frac{\partial c_o}{\partial t} - \frac{\partial c_o}{\partial Y} + 2t\sqrt{\frac{P_1}{P_2}}\, \frac{\partial^2 c_o}{\partial X \partial Y} = 0 \\ &M_1 = \int_{-\infty}^{\infty}\int\int \frac{c_1 \rho L^3}{\sqrt{P_1}\, P_2}\, dX\, dY\, dZ = 0 \text{ at } t = 0 \\ &c_1 \to 0 \quad \text{as } X^2 + Y^2 + Z^2 \to \infty \text{ for all } t = 0 \end{aligned}\right\} \qquad (4\text{-}48)$$

ε^2 coefficients

$$\left.\begin{aligned}
&\frac{\partial c_2}{\partial t} - \nabla^2 c_2 - \frac{Y}{\sqrt{P_2}}\frac{\partial c_1}{\partial t} - \frac{\partial c_1}{\partial Y} - \sqrt{\frac{P_1}{P_2}}\, t\, \frac{Y}{\sqrt{P_2}}\left(\frac{\partial^2 c_o}{\partial X \partial Y} + \frac{\partial c_o}{\partial X}\right) \\
&\quad - \sqrt{\frac{P_1}{P_2}}\, t\left(\frac{\partial^2 c_1}{\partial X \partial Y} + \frac{\partial c_1}{\partial X}\right) - \frac{P_1}{P_2}\, t^2\, \frac{\partial^2 c_o}{\partial X^2} = 0 \\
&M_2 = \int_{-\infty}^{\infty}\int\int \frac{c_2 \rho L^3}{\sqrt{P_1}\, P_2}\, dX\, dY\, dZ = 0 \text{ at } t = 0 \\
&c_2 \to 0 \text{ as } X^2 + Y^2 + Z^2 \to \infty \text{ for all } t
\end{aligned}\right\} \qquad (4\text{-}49)$$

The zero order coefficients in Eq. (4-45) are the same as those found for the constant dispersion coefficients, Eq. (4-32). Therefore, the solution is the same and is given by Eqs. (4-35) and (4-36) which are

$$c_o = \frac{A}{t^{3/2}} \exp\left\{ - \frac{1}{4t}(X^2 + Y^2 + Z^2) \right\} \qquad (4\text{-}35)$$

$$\text{where } A = \frac{(M_o/\rho)\sqrt{P_1}\, P_2}{8\pi^{3/2} L^3} \qquad (4\text{-}36)$$

Therefore, Eqs. (4-35) and (4-36) also represent the zero order approximation to the solution for variable dispersion coefficients. Thus, to zero order the solutions for constant and variable coefficients are identical.

Substituting Eq. (4-35) into Eq. (4-47) and rearranging gives

$$\frac{\partial c_1}{\partial t} - \nabla^2 c_1 = c_o\left\{ \frac{Y}{\sqrt{P_2}}\left(\frac{X^2 + Y^2 + Z^2}{4t^2}\right) - \frac{2Y}{t\sqrt{P_2}} - \sqrt{\frac{P_1}{P_2}}\, \frac{XY}{2t} \right\} \qquad (4\text{-}50)$$

The solution was found by the method of undetermined coefficients and is

$$c_1 = c_o\left\{ \frac{-3Y}{4\sqrt{P_2}} - \frac{XY}{4}\sqrt{\frac{P_1}{P_2}} + \frac{Y}{2\sqrt{P_2}}\left(\frac{X^2 + Y^2 + Z^2}{4t}\right)\right\} \qquad (4\text{-}51)$$

This is the correction to the zero order term. The concentration correct to first order is given by

$$c = c_o + \varepsilon c_1 = c_o\left\{1 - \frac{sXY}{4}\sqrt{\frac{P_1}{P_2}} - \frac{3sY}{4\sqrt{P_2}} + \frac{sY}{2\sqrt{P_2}}\left(\frac{X^2 + Y^2 + Z^2}{4t}\right)\right\} \qquad (4\text{-}52)$$

The first order concentration distribution for constant dispersion coefficients is given by the first two terms in the above equation. The other two terms reflect the correction to the constant coefficient due to the variation of the disperison coefficient.

The governing differential equation for the second order correction would be found by substituting Eqs. (4-51) and (4-35) into Eq. (4-49). In theory, a solution to the resulting equation could be found, but the process would require considerable algebraic endeavor. The solution was terminated at the first order because the comparison between the exact solution and the constant dispersivity coefficient solution indicated good agreement to first order for slopes and distances found in the porous pipe.

4.5 Limitations of the Perturbation Solutions

Perturbation techniques are used generally to provide solutions to problems which cannot be solved exactly. The solution is given in terms of a series expansion which is assumed to converge to the exact

solution. Since only the first two or three terms of the series are solved, the solution is an approximation and, therefore, is limited in its application. Some criterion must be given to indicate where the solution can be expected to be valid. Generally, the criterion is based on the parameter ε associated with the problem.

The limitations of the solution for variable dispersivity coefficients, Eq. (4-52), were sought by the usual method of a specification on the parameter ε. A criterion based on ε is really a specification on the slope, s. The slope is the ratio of the travel time to the shear time as can be seen by looking at the definition of s

$$s = \frac{du}{dy}\,\frac{L}{u_o} = \frac{du}{dy}\,t \tag{4-53}$$

By this definition, s is not a constant but depends upon the point of observation and the travel time. Therefore, the specification based upon it is difficult to interpret and determination of the specification was unsuccessful from a purely mathematical standpoint. Therefore, an alternate method of specifying the limitations of the solution was pursued. This involved the comparison of a perturbation solution using constant dispersion coefficients with an exact solution for the same conditions. The constant dispersion perturbation solution is a special case of the variable dispersion case and when it no longer could be considered valid, neither could the variable solution.

Carter and Okubo (1965) obtained the solution to the dispersion equation with constant coefficients for an instantaneous source in a shear flow. Their solution was for both horizontal and vertical shears.

By equating the horizontal shear to zero, their solution is the exact solution to the dispersion equation, Eq. (4-8), and in terms of the nondimensional variables previously defined is

$$c = \frac{A}{t^{3/2}(1 + \phi^2 t^2)^{1/2}} \exp -\left\{ \frac{\left(X + \frac{1}{2}\left[\frac{P_1}{P_2}\right] sYt\right)^2}{4t\,(1 + \phi^2 t^2)} + \frac{Y^2}{4t} + \frac{Z^2}{4t} \right\} \qquad (4\text{-}54)$$

where

$$\phi^2 = \frac{P_1}{P_2}\,\frac{s^2}{12} \qquad (4\text{-}55)$$

It is difficult to see the similarity between Eq. (4-54) in its present form and Eq. (4-43). But, by using the expansion

$$\frac{1}{1 + \phi^2 t^2} = 1 - \phi^2 t^2 + (\phi^2 t^2)^2 \ldots \qquad (4\text{-}56)$$

with $\phi^2 t^2 < 1$ completing the square of the first exponent term, and using the series expressions for the exponential terms extrinsic to these in Eq. (4-43), Eq. (4-54) can be approximately represented by

$$c = c_o \left\{ 1 - \sqrt{\frac{P_1}{P_2}}\,\frac{sXY}{4} - s^2\,\frac{P_1}{P_2}\left(-\frac{X^2Y^2}{32} + \frac{Y^2 t}{16} - \frac{X^2 t}{48} + \frac{t^2}{12} \right) + \ldots \right\} \qquad (4\text{-}57)$$

By comparing Eqs. (4-39) and (4-43), the first and second order perturbation solutions, with Eq. (4-57), it appears that the basic structure of the equations is similar. However, a criterion based on ε still cannot be established. Therefore, a numerical comparison was made upon which to establish the limitations of the perturbation solution.

The numerical comparison was based upon relative concentration contours. The concentrations were normalized by dividing them by $At^{-3/2}$. This normalization makes the concentrations relative to the concentration of a point moving in a uniform velocity field equal to the mean velocity along the X-axis. The contours at the 50% level of the normalized concentration were used as the basis of comparison.

The 50% contours for s = 1.0 and s = 1.5 are shown in Figs. 4-2 and 4-3. For s = 1.0, a slight deviation of the perturbation solutions from the exact solution is noticeable. The first and second order perturbation solutions bracket the exact solution with the first falling outside and the second inside of the exact solution.

For s = 1.5, greater deviations are noticeable. The first order solution approximately matches the exact solution over a portion of the contours but deviates more in the vertical (Y) direction than for s = 1.0. The second order solution falls noticeably inside the exact solution.

After examining the concentration contours for numerous values of s, the following criterion was established. The perturbation solutions for both first and second order for the constant dispersion coefficients were considered to be valid for values of $s \leq 1.0$. Since the constant coefficient solution is a special case of the variable dispersion solution, the criterion is assumed to apply for Eq. (4-52) also.

A comparison between the exact solution, Eq. (4-54), and the perturbation solution for variable dispersion coefficients Eq. (4-52), is given in Figs. 4-4 and 4-5. The contours at the 50% level are given in

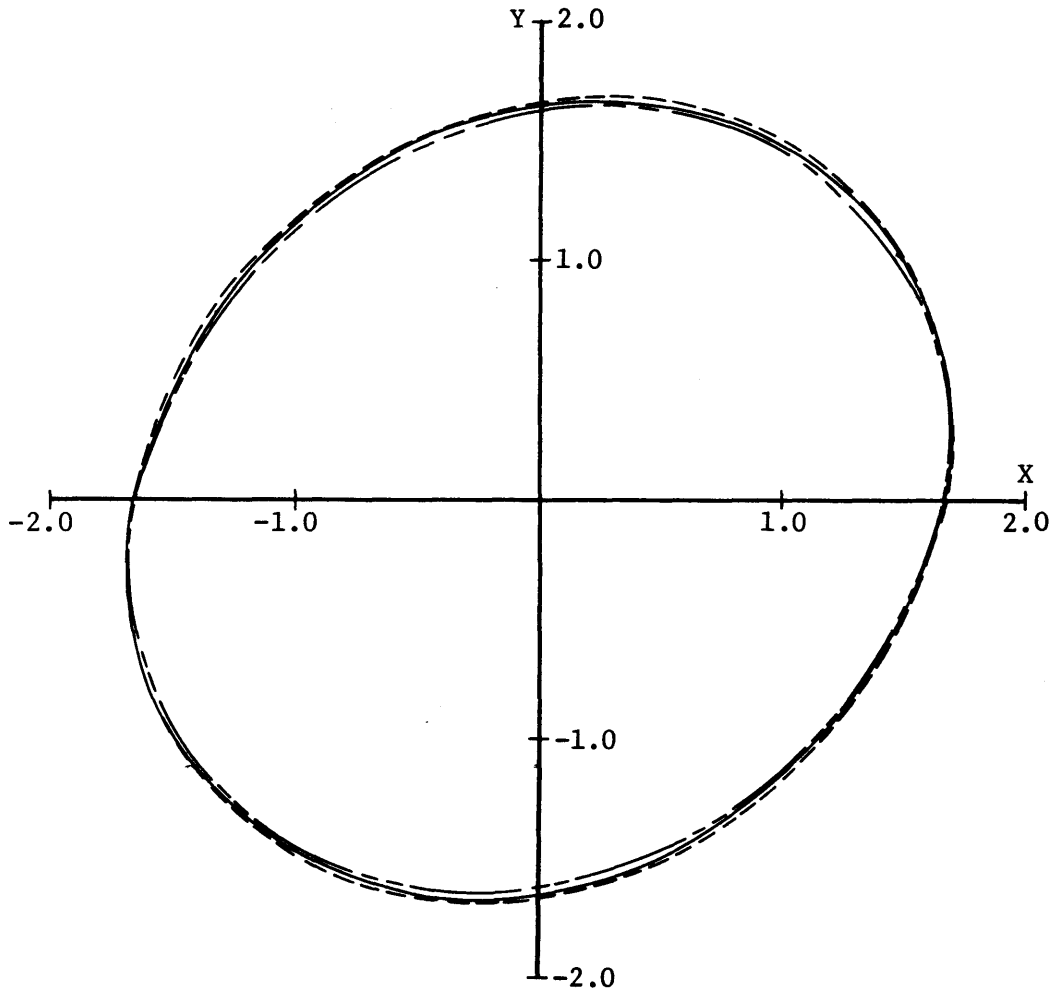

——————— Exact solution Eq. (4-58)

- - - - - - - - - First order perturbation solution Eq. (4-43)

——— - - ——— Second order perturbation solution Eq. (4-47)

Fig. 4-2 Relative concentration contours at 50% level for exact and perturbation solutions, s = 1.0

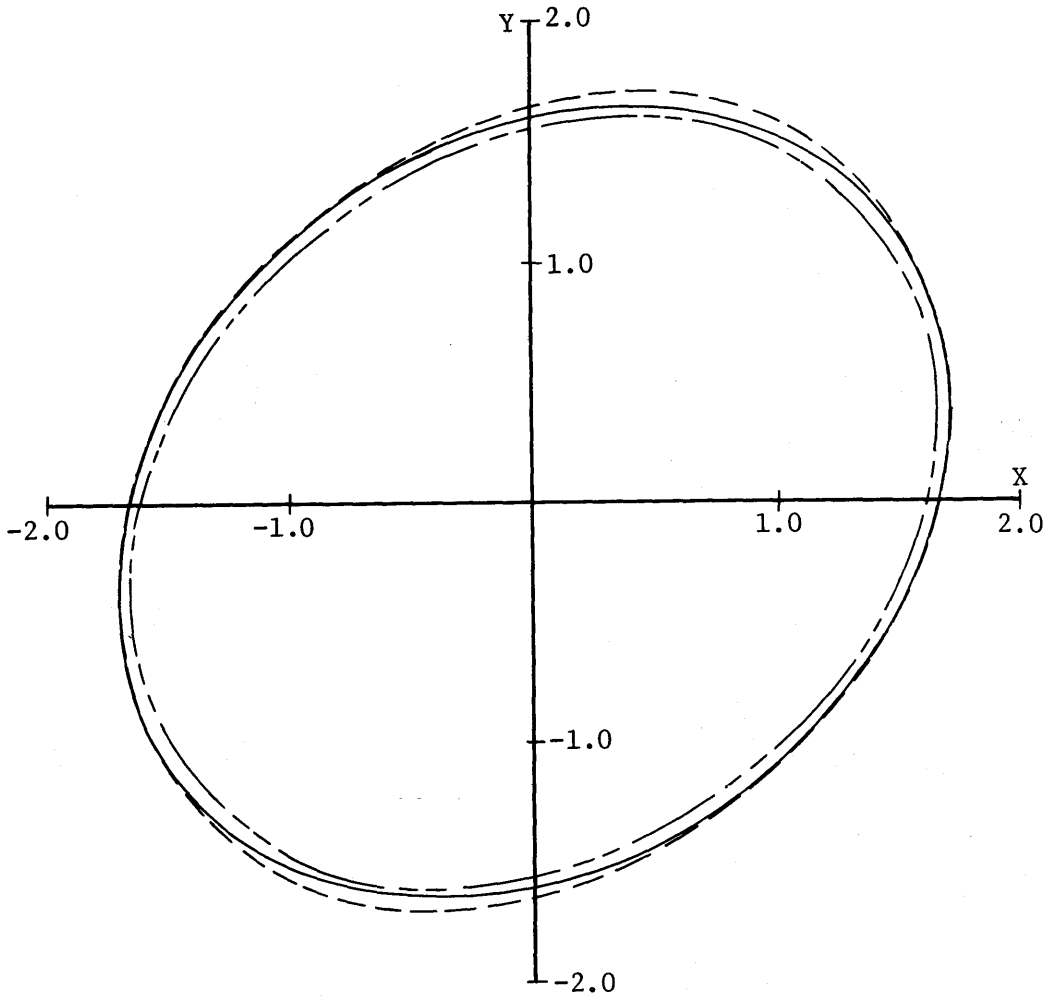

_____Exact solution Eq. (4-58)

_ _ _ _ _ _ _ _First order perturbation solution Eq. (4-43)

____ _ _ _ _ _Second order perturbation solution Eq. (4-47)

Fig. 4-3 Relative concentration contours at 50% level for exact and perturbation solutions, s = 1.5

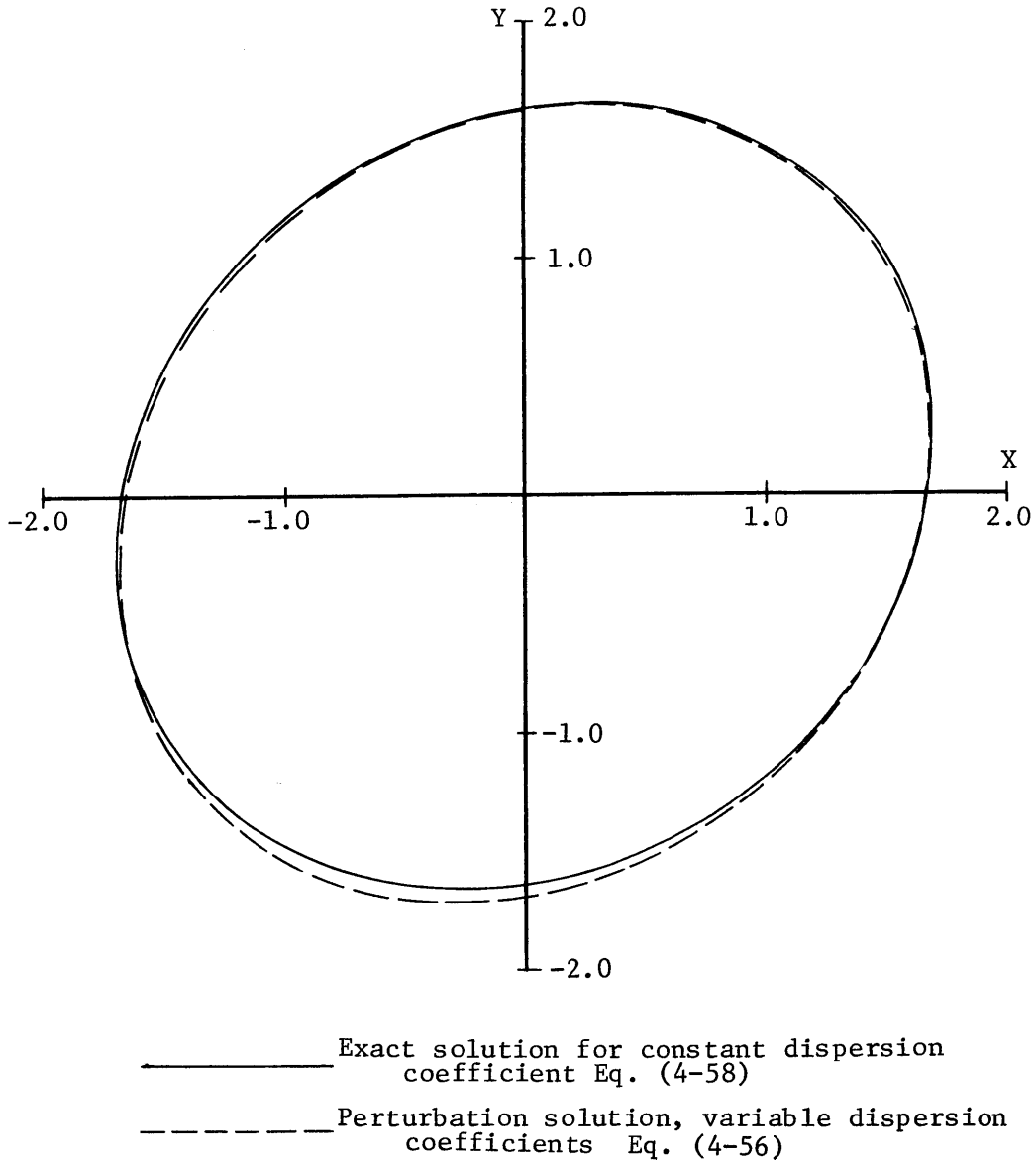

Fig. 4-4 Relative concentration contours at 50% level for the exact solution and variable dispersion perturbation solution, s = 1.0

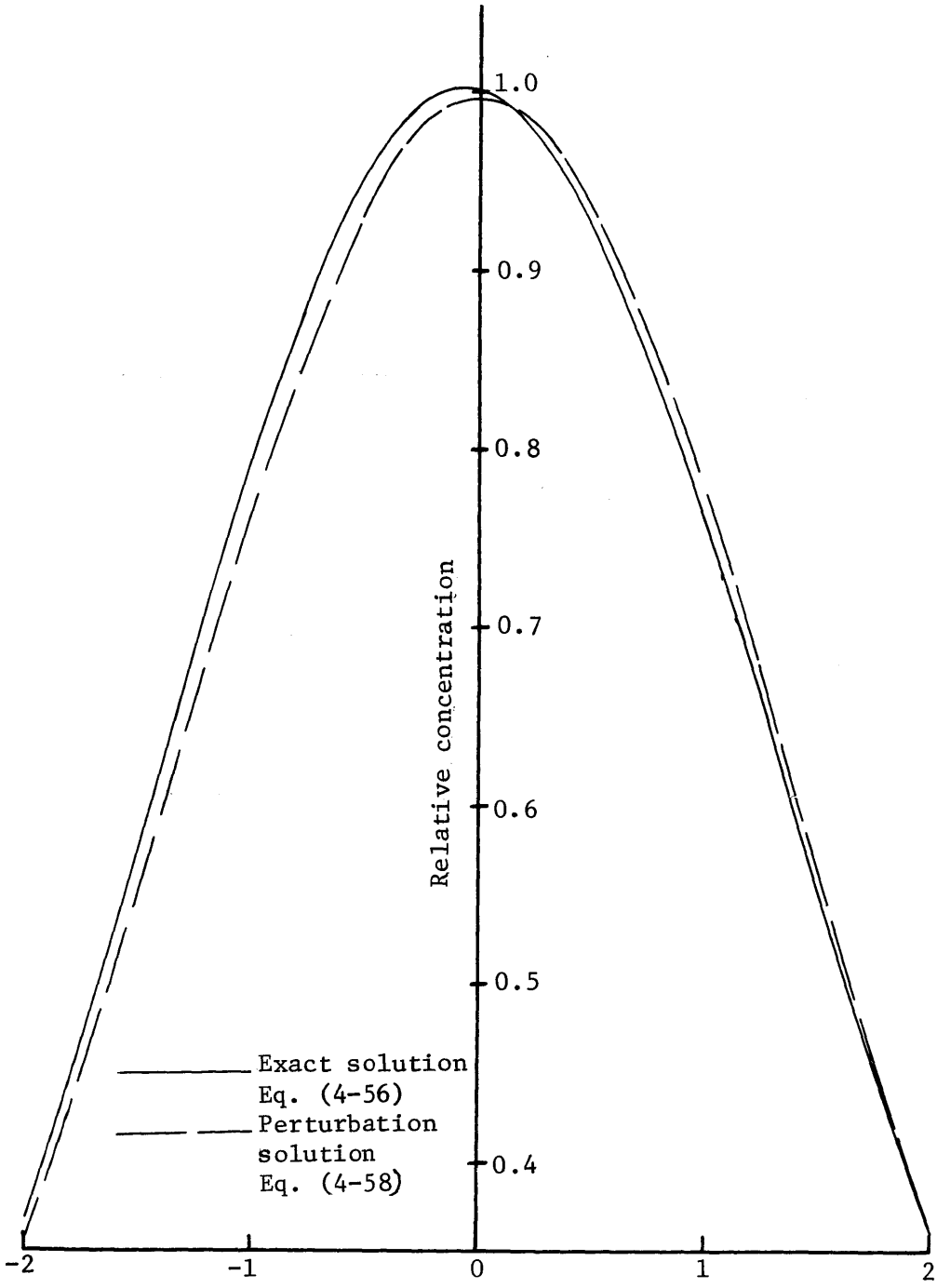

Fig. 4-5 Relative concentrations along the vertical axis

Fig. 4-4 and cross sections along the Y axis of the concentration distributions are given in Fig. 4-5. It is apparent from Fig. 4-4 that the shearing effect is more pronounced for the variable coefficient solution than for the exact constant coefficient solution. The distribution is drawn into the zone of lower velocity and Fig. 4-5 indicates that the maximum concentration no longer is located on the X axis but has shifted slightly below the axis. This shift, when related to the porous pipe problem, is negligible.

Application of Eq. (4-52) to the porous pipe case is considered by using the velocity profiles given in Chapter 2. The criterion based on the slope, $s \leq 1.0$, is more likely to be exceeded at the lower Reynolds numbers. For the lower Reynolds number case, a value of $U = 0.25$ and a gradient of $\frac{du}{dy} = 2$ could be expected in the shearing zone. Using these values the maximum distance to the point of observation according to Eq. (4-53) is 0.125 ft for $s = 1.0$. The maximum distance from the injector to the probes varied from 0.115 ft. to about 0.25 ft. during the experiments. However, observations in the shearing zone were achieved only at the minimum distance, 0.115 ft., and these could be considered only as partially successful. In the region of pressure gradient flow and in the transition to the shearing zone, the tracer method worked successfully and Eq. (4-52) is applicable.

Since Eq. (4-52) is the result of a perturbation about a uniform velocity, its application is limited to velocity fields approaching a uniform distribution. The flow conditions approaching those required for application of Eq. (4-52) are found in the ocean, large rivers and

channels, and the atmosphere. The distinguishing feature of the solution is the relationship of the dispersion coefficients to the shear velocity. The perturbation method can be used for velocity profiles other than linear by including more terms in the expansion. Obviously, for cases involving a linear shear and constant coefficients of dispersion, Carter and Okubo's solution, Eq. (4-57), is the one to use.

4.6 Velocity of Peak Concentration

It is obvious from Fig. 4-3 that distortion of the concentration distribution occurs in a shear flow. Both dispersion and convection tend to spread and distort the tracer cloud. In the higher velocity regions the cloud moves ahead at a greater rate than would be evident in a uniform field due to a higher convection velocity and due to the result of a greater dispersion rate. In the lower velocity region the reverse is true since both the convective velocity and the dispersion rate are less than for a uniform velocity. Since the shear was the most significant contributor to the patch distortion, it was expected that it would also have an effect on the longitudinal velocity of the peak concentration. This effect was evaluated by considering the concentration distribution given by Eq. (4-52).

By locating the shielded probes and injector always on a line parallel to the pipe center line and by using this fact, the concentration, Eq. (4-52), can be reduced to a simple expression by setting $Y = 0$ and $Z = 0$. The reduced equation after transformation back to dimensional form becomes

$$c = \frac{M/\rho}{8\pi^{3/2}\sqrt{E_1}\,E_2 t^{3/2}} \exp\left\{-\frac{(x-ut)^2}{4E_1 t}\right\} \tag{4-58}$$

The location of the maximum concentration can be found by setting $\frac{dc}{dt} = 0$ which reduces to

$$u^2t^2 + 6\,E_1 t - x^2 = 0 \tag{4-59}$$

Solving Eq. (4-59) for t gives the time required for the maximum concentration to arrive at the point, x, which is

$$t = -\frac{3E_1}{u^2} + \frac{\sqrt{9E_1^2 + u^2x^2}}{x^2} \tag{4-60}$$

The velocity of the peak concentration, U_p, can be found by considering the time required to move between two points on the axis, x_1 and x_2, such that

$$U_p = \frac{x_2 - x_1}{t_2 - t_1} \tag{4-61}$$

Using the subscripts 1 and 2 to distinguish the two points and times and substituting Eq. (4-60) into (4-61) gives

$$U_p = \frac{u(x_2 - x_1)}{\left(x_2^2 - \frac{9E_1^2}{u^2}\right)^{1/2} - \left(x_1^2 - \frac{9E_1^2}{u^2}\right)^{1/2}} \tag{4-62}$$

It is apparent from Eq. (4-62) that the peak concentration travels at a velocity different than the mean stream velocity, u. The difference

is independent of the shearing effect, therefore, indicating that along the longitudinal axis the shear does not affect the velocity of the peak concentration. The difference is due to the effect of the dispersion as indicated by the term

$$\frac{9E_1^2}{u^2x^2}.$$

However, as in most studies, if $\frac{9E_1^2}{u^2x_1^2} \ll 1$, and $\frac{9E_1^2}{u^2x_2^2} \ll 1$, then $U_p \simeq u$.

The value of the dispersion coefficient found in the porous foam was $E_{10} = 0.00167\ u_o$. During the experiments, the minimum distance from the injector to the first probe was 0.055 ft. and for this distance, Eq. (4-62) indicates a peak velocity which deviates less than one percent from the mean velocity. Thus, within the experimental accuracy, it was assumed that there was no distortion on the longitudinal axis due to either the shearing effect or the dispersion effect.

V. SUMMARY AND CONCLUSIONS

5.1 Flow in a Porous Foam Boundary

Velocity distributions in the porous boundary of a pipe were investigated in this study. Measurements were performed in the 1.2 in. thick polyurethane foam lining of a 12 in. ID pipe which was part of an open circuit air flow system. Several methods of making velocity measurements were attempted which involved hot wire anemometers and a helium tracer technique. An unshielded hot wire anemometer was unsatisfactory due to the disturbance caused by the hole required in the boundary. A helium tracer technique was devised and miniature hot wire anemometer probes were developed for use as sensors. Travel time of the peak concentration between two shielded probes provided the data for determining the seepage velocities. The data was reduced manually and by crosscorrelation of the anemometer output signals. In the shearing zone, seepage velocities were determined directly from the shielded hot wire anemometer data. Measurements performed by both the tracer technique and with the shielded probes are required to provide the velocity distribution over the entire porous foam boundary. Measurements of the longitudinal turbulent intensities were also made and they provide some indication of the penetration depth of the shear effects but are difficult to interpret in an absolute sense.

Mathematical models based on an eddy viscosity concept were developed to provide a theoretical velocity profile which could be

compared with the measured results. Three models were developed, two assuming constant eddy viscosity and the third using an eddy viscosity proportional to the velocity. The resulting profiles were all of exponential form with the penetration depth providing the major indication of their differences. Within the scatter of the experimental results, any of the theories could be considered to give a satisfactory representation of the velocity distribution.

An attempt was made to relate the core flow in the pipe with the boundary flow through the surface velocity and the eddy viscosities at the surface of the porous boundary. It was hoped that this relationship would provide a basis for predicting friction factors for the pipe which increased with increasing Reynolds number as was observed. However, this model predicted friction factors which decreased with increasing Reynolds numbers.

Development of the tracer technique for velocity measurements required additional knowledge of the concentration distribution of a tracer in a shear flow. Perturbation methods were used to develop analytical solutions for dispersion from an instantaneous point source in a shear flow with both constant and variable dispersion coefficients. The constant coefficient solution was compared with a known exact solution to determine the limitations of the method. The solutions were applicable provided that the product of shear rate and travel time to the point of interest is less than 1. The shear effect caused no distortion in the peak concentration velocity along the longitudinal axis. Distortion

due to dispersion effects was less than one percent and was considered to be insignificant in comparison with the experimental accuracy presently possible.

5.2 Conclusions

The velocity profiles measured in the porous foam boundary of a pipe indicate that shear effects penetrate to a relatively small distance (about 0.25 to 0.30 in.) into the boundary. A finite velocity exists at the surface of the porous boundary and its magnitude when normalized with the shear velocity is about 1 to 3. The velocity decreases approximately exponentially over the penetration depth and a pressure gradient flow exists over the remainder of the porous boundary.

New experimental techniques and instruments were developed to provide satisfactory velocity measurements in a porous foam boundary. By combining the results of two measurement techniques, it is possible to determine the velocity distribution throughout the entire porous boundary. In the shearing zone of the boundary, the shielded hot wire anemometer gave satisfactory results. In the pressure gradient zone, the tracer technique provides a direct method of measuring the seepage velocities.

An analysis which was based on the eddy viscosity concept gave reasonable agreement between the observed and predicted velocity profiles in the porous boundary. However, predictions of pipe friction factor based on the surface slip velocity and eddy viscosity from this analysis do not agree with observations. This

eddy viscosity model of shear flow in a porous boundary does not explain the interaction between the boundary and core flows.

A perturbation analysis of the concentration disbribution in a shear flow due to an instantaneous point source was developed. Along the longitudinal axis, shear effects cause no distortion in the velocity of the peak concentration. The solution is applicable to diffusion and dispersion from an instantaneous point source provided that the product of shear rate and travel time to the point is less than 1.

5.3 Recommendations

The present study should provide the background for additional research into porous boundary effects in turbulent shear flow. It presents the first experimental data for flow in the boundary. Further refinement of the tracer technique should be attempted. With the design of a more sophisticated injector, it may be possible to achieve direct measurements of the seepage velocity in the shear zone.

From the theoretical point of view, different models should be devised in an attempt to describe the interacting mechanism between the core and boundary flow. If this coupling could be found, gross flow features such as the friction factor could be predicted. Perhaps, such a model would provide a greater understanding of resistance to flow in alluvial channels since they have been shown by Lovera and Kennedy (1969) to exhibit an increase in resistance with increasing Reynolds number. The determination of the proper model may not be easily accomplished, but additional knowledge may

be gained through additional experiments since a method is now available for making measurements in the boundary.

BIBLIOGRAPHY

1. Beavers, G. S. and Joseph, D. D., "Boundary Conditions at a Naturally Permeable Wall", Journal of Fluid Mechanics, Vol. 30, Part I, 1967, pp. 197-207.

2. Bird, R. B., Stewart, W. E. and Lightfoot, E. N., Transport Phenomena, John Wiley and Sons Inc., New York, New York, 1960.

3. Brinkman, H. C., "On the Permeability of Media Consisting of Closely Packed Porous Particles", Applied Science Research, A1, 1947, pp. 81-86.

4. Buyevich, Yu A., Leonov, A. I. and Safrai, V. M., "Variations in Filtration Velocity due to Random Large-Scale Fluctuations of Porosity", Journal of Fluid Mechanics, Vol. 37, Part 2, 23 June 1969, pp. 371-381.

5. Carter, H. H. and Okubo, A., "A Study of the Physical Processes of Movement and Dispersion in the Cape Kennedy Area", U.S. Atomic Energy Commission, 20, 20359(NYO-2973-1), 1965.

6. Cionco, R. M., "A Mathematical Model for Air Flow in a Vegatative Canopy", Journal of Applied Meteorology, Vol. 4, August 1965, pp. 517-522.

7. Collis, D. C. and Williams, M. J., "Two-Dimensional Convection From Heated Wires at Low Reynolds Number", Journal of Fluid Mechanics, 6, Part 3, October 1959, pp. 357-384.

8. Crank, J., The Mathematics of Diffusion, Oxford University Press, London, 1956, 347 pp.

9. Eckert, E. R. G., Diaguila, A. J., and Donoughe, P. L., "Experiments on Turbulent Flow Through Channels Having Porous Rough Surface With and Without Air Injection", N.A.C.A. TN 3339, 1955.

10. Einstein, H. A., "Deposition of Suspended Particles in a Gravel Bed", Journal of the Hydraulics Division, A.S.C.E., Vol. 94, No. HY 5, September, 1968, pp. 1197-1205.

11. Flow Corporation, "Constant Temperature Hot-Wire Anemometer Instructions", Bulletin 900A, March 1967.

12. Flow Corporation, "Hot Wire Measurements of Air Velocity, Direction and Temperature", Bulletin 94B, January 1964.

13. Forstall, W. Jr. and Shapiro, A. H., "Momentum and Mass Transport in Coaxial Gas Jet", Transactions A.S.M.E., Journal of Applied Mechanics, Vol. 17, 399 pp., 1950.

14. Harleman, D. R. F., "Transport Processes in Water Quality Control", A series of notes to accompany lectures in 1.77- Water Quality Control, Department of Civil Engineering, M.I.T., 1970, 43 pp.

15. Harleman, D. R. F., Mehlhorn, P. F., and Rumer, R. R., Jr., "Longitudinal Dispersion in Uniform Porous Media", Report No. 57, Hydrodynamics Laboratory, M.I.T., August 1962, 30 pp.

16. Hinze, J. O., Turbulence , McGraw-Hill Book Co., Inc., New York, 1959.

17. Hoopes, E. R., "Unified View of Diffusion and Dispersion", Journal of the Hydraulics Division, ASCE, Vol. 95, No. HY 2, March 1969, pp. 621-631.

18. Hoopes, J. A. and Harleman, D. R. F., "Waste Water Recharge and Dispersion in Porous Media", Report No. 75, Hydrodynamics Laboratory M.I.T., June 1965, 166 pp.

19. Inoue, E., "On the Turbulent Structure of Airflow Within Crop Canopies", Journal of Meteorological Society of Japan, Vol. 41, 1963, pp. 317-326.

20. Lee, Y. W., Statistical Theory of Communication , John Wiley and Sons, Inc., New York, 1960.

21. Lovera, F. and Kennedy, J. F., "Friction Factors for Flat Bed Flows In Sand Channels", Journal of the Hydraulics Division, ASCE, Vol. 95, No. HY 4, July 1969, pp. 1227-1234.

22. Munoz Goma, R. J. and Gelhar, L. W., "Turbulent Pipe Flow with Rough and Porous Walls", Report No. 109, Hydrodynamics Laboratory, Department of Civil Engineering, M.I.T., April 1968, p. 162.

23. Murray, J. D. "Viscous Damping of Gravity Waves Over a Permeable Bed", Journal of Geophysics Research, Vol. 70, No. 10, May 15, 1965, pp. 2325-2332.

24. Olsen, R. M. and Eckert, E. R. G., "Experimental Studies of Turbulent Flow in a Porous Circular Tube with Uniform Fluid Injection Through the Tube Wall", Transactions A.S.M.E., Journal of Applied Mechanics, Vol. 33, Series E, No. 1, March 1966, pp. 7-17.

25. Plate, E. J. and Quraiski, A. A., "Modeling of Velocity Distribution Inside and Above Tall Crops", Journal of Applied Meterology, Vol. 4, June 1965, pp. 400-408.

26. Princeton Applied Research Corporation, "Instruction Manual Correlation Function Computers Model 100 and 101", 1967.

27. Rotta, J. "Das in Wandähe Gültige Geschwindigkeitsgesetz Turbulenten Strömungen", Ingenieur-Archiv, 18, No. 4, 1950, pp. 277-280.

28. Rush, D. and Forstall, W., Jr., "Apparatus for the Determination of the Concentration of Helium in Air by the Thermal Conductivity Method", M.I.T. Gas Turbine Laboratory, Meteorology Internal Report No. 4, January 1947., 16 pp.

29. Takeda, K., "On Roughness Length and Zero-Plane Displacement in the Wind Profile of the Lowest Air Layer", Journal of Meteorological Society of Japan, Vol. 44,No. 2, April 1966, pp. 101-107.

30. Ward, J. C., "Turbulent Flow in Porous Media", Proceedings of A.S.C.E., Journal of Hydraulics Division, Vol. 90, No. HY 5, September, 1964, pp. 1-12.

31. Weast, R. C. (ed.), Handbook of Chemistry and Physics, 49th Edition, The Chemical Rubber Co., Cleveland, Ohio, 1968.

32. Wylie, C. R., Jr., Advanced Engineering Mathematics, McGraw-Hill Book Co., Inc., New York, 1951.

33. Yuan, S. W. and Brogren, E. W., "Turbulent Flow in a Circular Pipe with Porous Wall", The Physics of Fluids, Vol. 4, No. 3, March 1961, pp. 368, 372.

APPENDIX A

LIST OF SYMBOLS

Only the commonly used symbols are defined here. Some repetition of symbols is unavoidable; in such cases it is obvious from the context in which they appear which definition applies. Dimensions of symbols, if any, are enclosed in parentheses.

English

a	Fourier coefficient
A	Constant depending on wire characteristics
A	Instantaneous point source strength
b	Fourier coefficient
B	Constant of proportionality in eddy viscosity
c	Mass concentration, mass of tracer per mass of solution
c	Constant characteristic of porous medium
C	Constant characteristic of hot wire
d	wire diameter (ft)
D_{AB}	Molecular diffusion coefficient (sq ft/sec)
E	Turbulent dispersion coefficient (sq ft/sec)
E_{10}	Dispersion coefficient on longitudinal axis (sq ft/sec)
f	Friction factor
f_d	Drag force per unit volume (lb/cu ft)
g	Gravitational acceleration (ft/sec^2)
I	Electric current in the hot wire (amperes)
k	Intrinsic permeability (sq ft/sec)

K	Thermal conductivity (Btu/sec-ft-°R)
ℓ	Wire length (ft)
L	Characteristic length (ft)
M	Mass of tracer (slugs)
n	Constant exponent depending on hot wire characteristics
n	porosity
p	pressure (lb/sq ft)
P	Constant, ratio of characteristic length and dispersivity coefficient
q	Specific discharge (ft/sec)
R	Wire resistance (ohms)
R	Radius to porous boundary (ft)
$\mathbb{R}$	Pipe Reynolds number
$\mathbb{R}_k$	Permeability Reynolds number
s	Slope of nondimensional velocity profile
t	Time (sec)
T	Absolute temperature (°K)
T	Fundamental period of periodic signal (sec)
u	Mean velocity in x direction (ft/sec)
u	Normalized seepage velocity in longitudinal direction
u_o	Characteristic velocity (ft/sec)
u_*	Shear velocity (ft/sec)
U	Seepage velocity normalized with shear velocity
U_1	Seepage velocity due to pressure gradient normalized with shear velocity
$\hat{U}_o$	Surface velocity normalized with shear velocity

$\hat{U}$	Seepage velocity less pressure gradient flow normalized with shear velocity
v	Mean velocity in y direction (ft/sec)
V	Fluid velocity normal to hot wire (ft/sec)
V_o	Seepage velocity normalized with average velocity
V_1	Pressure gradient seepage velocity normalized by average velocity
w	Mean velocity in z direction (ft/sec)
x	Longitudinal coordinate
X	Transformed coordinate
y	Vertical coordinate
Y	Transformed coordinate
z	Transverse horizontal coordinate
Z	Transformed coordinate

Greek

α	Dispersivity coefficient (ft)
β	Constant dependent on porous medium
$\delta(\gamma)$	Dirac delta function of the variable γ
ε	Eddy viscosity (sq ft/sec)
ε	Parameter in perturbation solutions
κ	Karman's constant (0.4)
μ	Dynamic viscosity of fluid (lb-sec/ft^2)
ν	Kinematic viscosity (sq ft/sec)
ξ	Transformed coordinate moving relative to the mean velocity
ρ	Density (slugs/cu ft)

τ	Shear stress (lb/sq ft)
τ_o	Shear stress at surface of porous boundary (lb/sq ft)
ϕ^2	Constant

Subscripts

More than one subscript can be used with one symbol.

i,j,k	Can take any value of 1,2,3 which represent the three coordinate directions
o	Value at surface of porous boundary or at a known reference value
R	Any reference value
1	Pressure gradient direction

APPENDIX B

LIST OF FIGURES

APPENDIX C

APPROXIMATE ANALYSIS OF THE FRICTION FACTOR-REYNOLDS NUMBER RELATIONSHIP

Analysis of the change in friction factor, f, with the permeability Reynolds number, $\mathbb{R}_k$, is presented for the eddy viscosity model, $\varepsilon = BL\hat{U}_o$. Analysis of the other model proceeds in the same manner with the differences arising from equations for $\hat{U}_o$ and δ. The method is described in Section 3.7 and, therefore, only the mathematical details are included here.

The goal of the analysis is to determine the sign and magnitude of the slope, $\dot{F}$, where

$$\dot{F} = \frac{d\sqrt{\frac{8}{f}}}{d \ln \mathbb{R}_k} = \mathbb{R}_k \frac{d\sqrt{\frac{8}{f}}}{d \mathbb{R}_k} \tag{C-1}$$

It is assumed that the quantities c, $\sqrt{k}$, and R, and the reference values, $\left(\sqrt{\frac{8}{f}}\right)_o$ and $(\ln \mathbb{R}_k)_o$ are known.

The solution is developed by first determining the pressure gradient flow, V_1, from Eq. (3-83). Note that all velocities are normalized with the average pipe velocity, $\bar{u}$, in this Appendix. The value of B and the surface velocity, $\hat{V}_o$ are determined simultaneously from Eqs. (3-81) and (3-82). Denoting the differentiation with respect to the $(\ln \mathbb{R}_k)$ by a dot over the variable, the Eqs. (3-83), (3-81) and (3-82) are differentiated respectively to give the following three equations.

$$a_1\dot{F} + b_1\dot{V}_1 + d_1 = 0 \tag{C-2}$$

where

$$a_1 = \frac{4c\sqrt{k}}{R}\left(\sqrt{\frac{8}{f}}\right)^{-3}$$

$$b_1 = \left\{\frac{c^2}{\mathbb{R}_k^{\,2}} + \frac{8c\sqrt{k}}{R}\left(\sqrt{\frac{8}{f}}\right)^{-2}\right\}^{1/2}$$

$$d_1 = \frac{c^2}{2\,\mathbb{R}_k^{\,2}} - \frac{c}{2\,\mathbb{R}_k}\,b_1$$

$$\dot{F} + b_2\,\dot{V}_1 + c_2\,\dot{\hat{V}}_o + d_2 = 0 \qquad \text{(C-3)}$$

where

$$b_2 = \frac{B\hat{V}_o^{\,3}}{2c}\left(\sqrt{\frac{8}{f}}\right)^5$$

$$c_2 = B\left(\sqrt{\frac{8}{f}}\right)^5\left\{\frac{3\hat{V}_o^{\,2}}{4}\left(\mathbb{R}_k^{\,-1} + \frac{2V_1}{c}\right) + \frac{2\hat{V}_o^{\,3}}{3c}\right\}$$

$$d_2 = \frac{-B\hat{V}_o^{\,3}}{4\,\mathbb{R}_k}\left(\sqrt{\frac{8}{f}}\right)^5$$

$$a_3\dot{F} + b_3\,\dot{V}_1 + c_3\,\dot{\hat{V}}_o = 0 \qquad \text{(C-4)}$$

where

$$a_3 = 1 - V_o - V_1 + \left(\kappa\sqrt{\frac{8}{f}}\right)^{-1}$$

$$b_3 = -\sqrt{\frac{8}{f}}$$

$$c_3 = \frac{1}{\kappa\hat{V}_o} - \sqrt{\frac{8}{f}}$$

The value of $\dot{F}$ can be found by solving Eqs. (C-2), (C-3) and (C-4)

simultaneously. The resulting equation becomes

$$\dot{F}\left(1 - a_3 \frac{c_2}{c_3} - a_1 \frac{b_2}{b_1} + a_1 \frac{b_3}{b_1} \frac{c_2}{c_3}\right) + d_2 - d_1\left(\frac{b_2}{b_1} - \frac{b_3}{b_1} \frac{c_2}{c_3}\right) = 0 \quad \text{(C-5)}$$

Thus, it is possible to determine $\dot{F}$ at the point of interest on the curve by evaluating the coefficients of Eqs. (C-2), (C-3) and (C-4). The coefficients are functions only of B, V_1, and $\hat{V}_o$. The friction factor at another $\mathbb{R}_k$ now can be estimated by using Eq. (3-84).